Fakultät 4 – Mathematik und Naturwissenschaften
Bergische Universität Wuppertal

Ultra-high-energy cosmic rays: their source and target properties

Inaugural-Dissertation

zur Erlangung des Doktorgrades
(Dr. rer. nat.)

der Fachgruppe Physik vorgelegt von

David Wittkowski
aus Ratingen

Wuppertal, Januar 2025

Aus der Arbeitsgruppe Astroteilchenphysik
der Bergischen Universität Wuppertal

Der Fachgruppe Physik der Bergischen Universität Wuppertal als Dissertation vorgelegt.

Referent: Prof. Dr. rer. nat. Karl-Heinz Kampert
Korreferent: Prof. Dr. rer. nat. Günter Sigl

Tag der mündlichen Prüfung: 25.03.2025

Vorwort

Die vorliegende Arbeit entstand in der Arbeitsgruppe Astroteilchenphysik der Bergischen Universität Wuppertal. Sie stellt die wichtigsten Ergebnisse vor, die der Verfasser in den letzten Jahren für seine Promotion erarbeitet hat. Teile der in dieser Arbeit vorgestellten Ergebnisse wurden zuvor durch den Verfasser dieser Arbeit in den Artikeln [1–4] veröffentlicht. Dies sind im Einzelnen die folgenden Artikel:

[1] David Wittkowski, Tobias Winchen, and Karl-Heinz Kampert:
Influence of the extragalactic background light and magnetic field on the energy spectrum and chemical composition of ultra-high-energy cosmic rays.
Auger internal publication, GAP2017-001 (2017)

Author contributions:
D. Wittkowski performed the research (computer simulations, derivations, data analyses, etc.), discussed the results, prepared the figures, and wrote the manuscript. T. Winchen discussed the results and assisted in data analyses. K.-H. Kampert supervised the work, provided computing resources for the simulations, discussed the results, proofread the manuscript, and commented on the manuscript.

[2] David Wittkowski for the Pierre Auger Collaboration:
Reconstructed properties of the sources of UHECR and their dependence on the extragalactic magnetic field.
Proceedings of the 35th International Cosmic Ray Conference (ICRC 2017), Proceedings of Science (SISSA, Trieste), 563 (2018)

Author contributions:
D. Wittkowski performed the research (computer simulations, derivations, data analyses, etc.), discussed the results, prepared the figures, and wrote the manuscript. K.-H. Kampert supervised the work, provided computing resources for the simulations, discussed the results, proofread the manuscript, and commented on the manuscript. The Pierre Auger Collaboration discussed the results and commented on the manuscript as part of its usual internal collaboration review process.

[3] David Wittkowski and Karl-Heinz Kampert:
On the anisotropy in the arrival directions of ultra-high-energy cosmic rays.
Astrophysical Journal Letters **854**, L3 (2018)

Author contributions:
D. Wittkowski performed the research (computer simulations, derivations, data analyses, etc.), discussed the results, prepared the figures, and wrote the manuscript. K.-H. Kampert supervised the work, provided computing resources for the simulations, discussed the results, proofread the manuscript, and commented on the manuscript. The Pierre Auger Collaboration discussed the results and commented on the manuscript as part of its usual internal collaboration review process.

[4] David Wittkowski and Karl-Heinz Kampert:
On the flux of high-energy cosmogenic neutrinos and the influence of the extragalactic magnetic field.
Monthly Notices of the Royal Astronomical Society Letters **488**, L119-L122 (2019)

Author contributions:
D. Wittkowski performed the research (computer simulations, derivations, data analyses, etc.), discussed the results, prepared the figures, and wrote the manuscript. K.-H. Kampert supervised the work, provided computing resources for the simulations, discussed the results, proofread the manuscript, and commented on the manuscript. The Pierre Auger Collaboration discussed the results and commented on

the manuscript as part of its usual internal collaboration review process.

Aufgrund dieser Vorabveröffentlichung von Ergebnissen des Verfassers dieser Arbeit, die während seiner Promotionszeit entstanden sind, stimmen Teile dieser Arbeit mit den Inhalten (Texte wörtlich oder sinngemäß, Gleichungen, Abbildungen, Tabellen,...) aus den Artikeln [1–4] überein:

Kurzfassung: Veröffentlichungen [1–4]

Abstract: Veröffentlichungen [1–4]

Kapitel 1: Veröffentlichungen [1–4]

Kapitel 4: Veröffentlichungen [1–4]

Kapitel 5: Veröffentlichungen [1, 2]

Kapitel 6: Veröffentlichungen [1–4]

Kapitel 7: Veröffentlichungen [1–4]

Alle Inhalte aus den Veröffentlichungen [1–4], die auch in der vorliegenden Arbeit zu finden sind, stammen ausschließlich vom Verfasser dieser Arbeit und enthalten keine Beiträge von Koautoren dieser Veröffentlichungen. Zugunsten der Lesbarkeit dieser Arbeit wurde darauf verzichtet, die Übereinstimmung von Inhalten dieser Arbeit und der Artikel [1–4] zusätzlich in den jeweiligen Kapiteln zu kennzeichnen.

Die erzielten Forschungsergebnisse wurden durch den Verfasser dieser Arbeit auch auf zahlreichen nationalen und internationalen Konferenzen präsentiert und diskutiert.

Danksagung

An erster Stelle danke ich meinem Betreuer Herrn Prof. Dr. Karl-Heinz Kampert für die Möglichkeit, in seiner Arbeitsgruppe an sehr interessanten Themen aus dem Bereich der experimentellen Astroteilchenphysik zu arbeiten, und für die hervorragende Betreuung. Ich danke auch Herrn Prof. Dr. Günter Sigl für den häufigen und immer sehr hilfreichen Austausch. Darüber hinaus danke ich den Mitarbeitern der Arbeitsgruppe "Astroteilchenphysik" der Bergischen Universität Wuppertal für produktive Diskussionen. Abschließend danke ich der Pierre-Auger-Kollaboration für die gute Zusammenarbeit und der Telescope-Array-Kollaboration für weitreichende Einblicke in das Telescope-Array-Projekt bei meinem Aufenthalt in Utah (USA).

Kurzfassung

Trotz fünf Jahrzehnten intensiver Forschung ist ultrahochenergetische kosmische Strahlung (UHECRs) nach wie vor ein wichtiges Thema der aktuellen Forschung, da einige entscheidende Fragen zu UHECRs unbeantwortet geblieben sind. Beispielsweise sind bisher weder die Quellen von UHECRs noch die Eigenschaften ihrer Quellen bekannt. Außerdem ist der Fluss hochenergetischer kosmogener Neutrinos, die durch Wechselwirkungen von UHECRs mit kosmischen Hintergrundphotonen entstehen, noch nicht gemessen worden.

Die vorliegende Arbeit befasst sich mit diesen Problemen mit Hilfe von aufwendigen Computersimulationen der Propagation von UHECRs von ihren Quellen zur Erde und eines Vergleichs mit experimentellen Daten. Die Simulationen berücksichtigen alle drei Raumdimensionen, die kosmologische Entwicklung des Universums, Wechselwirkungen von UHECRs mit kosmischen Hintergrundphotonen und realistische Annahmen über das extragalaktische Magnetfeld. Auf dieser Grundlage wird untersucht, welches Energiespektrum und welche chemische Zusammensetzung der UHECRs an ihren Quellen angenommen werden müssen, um in den Simulationen ein Energiespektrum und eine chemische Zusammensetzung der die Erde erreichenden UHECRs zu erhalten, die am besten mit den entsprechenden vom Pierre-Auger-Observatorium gemessenen Daten übereinstimmen. Darüber hinaus wird der Fluss der die Erde erreichenden hochenergetischen kosmogenen Neutrinos vorhergesagt.

Die Ergebnisse dieser Arbeit zeigen, dass das am besten passende Energiespektrum und die am besten passende chemische Zusammensetzung an den Quellen stark vom extragalaktischen Magnetfeld und der kosmologischen Entwicklung der Quellen abhängen. Es wird auch gezeigt, dass die Verteilung der Ankunftsrichtungen der UHECRs eine ausgeprägte dipolare Anisotropie und relativ schwache Beiträge höherer Ordnung zum Winkelleistungsspektrum aufweist. Dieses Ergebnis stimmt gut mit der jüngsten

Beobachtung einer dipolaren Anisotropie für UHECRs mit Ankunftsenergien über $8 \cdot 10^{18}\,\mathrm{eV}$ durch das Pierre-Auger-Observatorium überein und stellt eine wichtige Vorhersage für andere Energiebereiche und Winkelbeiträge höherer Ordnung dar. Die Vorhersagen für den kosmogenen Neutrinofluss sind mit Obergrenzen konsistent, die vom Pierre-Auger-Observatorium und dem IceCube Neutrino Observatorium ermittelt wurden. Es wird gezeigt, dass das extragalaktische Magnetfeld einen starken Einfluss auf den Neutrinofluss hat.

Durch die Ergebnisse dieser Arbeit wird das Wissen über UHECRs und die damit zusammenhängenden kosmogenen Neutrinos erheblich erweitert. Da die durchgeführten Simulationen vollständig mit den verfügbaren experimentellen Daten übereinstimmen, stellen die zugrundeliegenden Informationen und Annahmen ein äußerst realistisches astrophysikalisches Szenario dar, das für die zukünftige Erforschung der UHECRs eine sehr nützliche Grundlage ist. Des Weiteren sind die Ergebnisse für das Design zukünftiger Neutrinoobservatorien wichtig, da sie ermöglichen, das Detektorvolumen und die Beobachtungszeit abzuschätzen, die für den Nachweis hochenergetischer kosmogener Neutrinos in naher Zukunft erforderlich sind. Eine Beobachtung solcher Neutrinos würde die Multimessenger-Astronomie auf bisher unerreichte Energieskalen ausweiten.

Abstract

Despite intensive research over the past five decades, ultra-high-energy cosmic rays (UHECRs) are still an important topic of current research, since several crucial questions regarding UHECRs have remained unanswered. For example, neither the sources of UHECRs nor the properties of their sources are known so far. Furthermore, the flux of high-energy cosmogenic neutrinos originating from interactions of UHECRs with cosmic background photons has not yet been measured.

This work addresses these issues by elaborate computer simulations of the propagation of UHECRs from their sources to the Earth and a comparison with experimental data. The simulations take into account three-dimensional space, the cosmological evolution of the universe, interactions of UHECRs with cosmic background photons, and realistic assumptions about the extragalactic magnetic field. On this basis, it is studied which energy spectrum and chemical composition of the UHECRs must be assumed at their sources to obtain an energy spectrum and a chemical composition of the simulated UHECRs arriving at the Earth that are in best agreement with the corresponding data measured by the Pierre Auger Observatory. Moreover, the flux of high-energy cosmogenic neutrinos arriving at the Earth is predicted.

The results of this work show that the best-fitting energy spectrum and chemical composition at the sources depend strongly on the extragalactic magnetic field and the source evolution. It is also found that the distribution of the arrival directions of the UHECRs has a pronounced dipolar anisotropy and relatively weak higher-order contributions to the angular power spectrum. This finding agrees well with the recent observation of a dipolar anisotropy for UHECRs with arrival energies above $8 \cdot 10^{18}$ eV by the Pierre Auger Observatory and constitutes an important prediction for other energy ranges and higher-order angular contributions. The predictions for the cosmogenic neutrino flux are consistent with upper limits obtained from

the Pierre Auger Observatory and the IceCube Neutrino Observatory. It is shown that the extragalactic magnetic field has a strong influence on the neutrino flux.

This work's results significantly extend the knowledge about UHECRs and the associated cosmogenic neutrinos. Since the performed simulations are found to be completely consistent with the available experimental data, the underlying information and assumptions constitute a highly realistic astrophysical scenario that will be a very useful basis for future studies on UHECRs. Furthermore, the results are important for the design of future neutrino observatories, since they allow to assess the detector volume and observation time that are necessary to detect high-energy cosmogenic neutrinos in the near future. An observation of such neutrinos would push multimessenger astronomy to hitherto unachieved energy scales.

Contents

1 Introduction

The discovery of *cosmic radiation*, an ionizing radiation coming from outside the Earth's atmosphere, by Victor Franz Hess in August 1912 during his famous balloon flight [5] was preceded by a couple of balloon flights at lower altitudes in the years 1911 and 1912. At these earlier balloon flights, Victor Hess also performed measurements during the partial solar eclipse of 17 April 1912 and at night. Since he did not measure a significant reduction of cosmic radiation during the solar eclipse or at night, he concluded, assuming a straight-line propagation of the cosmic radiation, that the Sun was not the major source of cosmic radiation [5, 6]. These balloon flights can therefore be seen as an early search for the sources of cosmic radiation [7].

He had the opportunity to read important works by the Jesuit priest and physicist Theodor Wulf [8, 9], who did measurements on the top of the Eiffel Tower, and the physicist Albert Gockel [10–12], who did measurements during balloon flights in Switzerland. This allowed him to improve his measuring instruments [13].

Werner Kolhörster independently confirmed [14] Hess's discovery of cosmic rays during balloon flights up to a height of 6.3 km in 1913 [15] and during a balloon flight up to a height of 9.3 km in 1914 [16]. However, it took several years and much more investigations before Hess's finding was generally accepted. For his discovery of cosmic radiation, Victor Hess was awarded the Nobel Prize for Physics 1936[1].

The literature sometimes mentions that Robert Andrews Millikan invented the term "cosmic radiation" [17] (p. 361), which is today's generally used term. However, this seems not to be true [18], since the term appeared already a few years before Millikan's publication in the literature as its German translation "kosmische Strahlung" [19]. Nonetheless, the use of

[1] The Nobel Prize for Physics 1936 was awarded equally to Carl David Anderson for the discovery of the positron and to Victor Franz Hess for the discovery of cosmic radiation.

the term "cosmic radiation", consisting of "cosmic rays" [20], by the famous researcher and Nobel laureate Robert Millikan benefited the rapid spread of the term in the literature and the gradual disappearance of other earlier terms [21], such as "Hesssche Strahlung" [22–24], "Höhenstrahlung" [25–27], or "Ultrastrahlung" [28–31]. The term "radiation" or "ray" was used, since at these days the nature of cosmic rays was not yet clear and Millikan wrongly assumed that cosmic rays consist mostly of electromagnetic radiation. Nevertheless, this term is commonly used until today.

In the late 1920s, Dimitry Skobelzyn succeeded in photographing secondary particles produced by cosmic radiation in the Earth's atmosphere with the help of a cloud chamber [32].

An important method that was invented in 1929 by Walther Wilhelm Georg Bothe and that was of high importance for the further study of cosmic rays is the coincidence technique [33, 34]. In consideration of subsequent discoveries made by this technique, Walther Bothe was awarded the Nobel Prize for Physics 1954[2].

By progress in scientific ballooning [35–37], it was possible to ascend from the troposphere, the lowest layer of Earth's atmosphere, through the tropopause into the stratosphere more safely and to collect data at much higher altitudes in the 1930s [38–40]. For example, roughly two decades after Kolhörster's 9 km high balloon flight, Erich Regner [41], who used an unmanned balloon and automated data acquisition, succeeded in publishing data corresponding to maximum altitudes of about 28 km [42, 43]. Also more risky manned stratospheric balloon flights were performed using life support systems like pressure suits or pressurized spherical gondolas [44, 45]. A pioneer studying cosmic radiation in manned stratospheric balloon flights was Jean Piccard [46–48].

In 1938, Pierre Auger and collaborators were able to detect extensive air showers (EASs) initiated by cosmic rays entering the Earth's atmosphere using a coincidence measurement [49]. Pierre Auger estimated that he could observe in his measurements EASs initiated by primary particles with an energy of about 10^{15} eV.

The further investigation of the cosmic radiation led to an enormous

[2] The Nobel Prize for Physics 1954 was awarded equally to Max Born for his fundamental contributions to quantum mechanics and Walther Bothe for the development of the coincidence method and the discoveries made with it.

gain of knowledge in particle physics, such as to the discovery of several previously unknown particles. Important examples are the discovery of the positron [50] and the muon [51] in the 1930s as well as the charged pions [52, 53] and kaons [54] in the 1940s. In the 1950s, research in particle physics started to focus on particle accelerators. They were able to reach particle energies in the GeV range in these years [55, 56], and achieved increasingly high particle energies in the subsequent years.

The research interest shifted progressively to higher energies so that increasingly large particle accelerators and detectors for cosmic rays were built. In the 1960s, a primary cosmic ray with an energy of about 10^{20}eV could be detected at the Volcano Ranch experiment in New Mexico by observing an air shower that has been initiated by that particle [57].

The discovery of the cosmic microwave background (CMB) by Arno Allan Penzias and Robert Woodrow Wilson in 1964, for which they were awarded the Nobel prize in Physics 1978[3] [58, 59], was also important for understanding the propagation of cosmic rays through the universe [60].

Figure 1.1 shows Robert Woodrow Wilson reporting at the 65th Lindau Nobel Laureate Meeting (2015) [61] during the author's attendance about his and Penzias' famous discovery of the CMB based on measurements with the "Holmdel Horn Antenna", a horn-reflector type [62] antenna [63] (which was originally constructed in 1959 to support "Project Echo" [64, 65], a pioneering satellite communications experiment) at Bell Telephone Laboratories in Holmdel (New Jersey, USA).

Shortly after the discovery of the CMB it was recognized by Kenneth Ingvard Greisen, Georgiy Timofeyevich Zatsepin, and Vadim Alekseyevich Kuzmin that the photons of the CMB interact with protons of the highest-energy cosmic rays and thus reduce their energy during propagation [66, 67].

Over the years, more and more cosmic rays with particle energies of about 10^{18} eV or more have been detected in different experiments. A well-known example for such experimental observations is the discovery of the famous "Fly's Eye event" with an energy of about $3{\cdot}10^{20}$ eV in the 1990s [68]. Other independent experiments such as the Sydney University giant airshower

[3]The Nobel Prize for Physics 1978 was awarded to Pyotr Leonidovich Kapitsa (prize share: 50%) for his research and discoveries in low-temperature physics and jointly to Arno Allan Penzias (prize share: 25%) and Robert Woodrow Wilson (prize share: 25%) for the discovery of the cosmic microwave background.

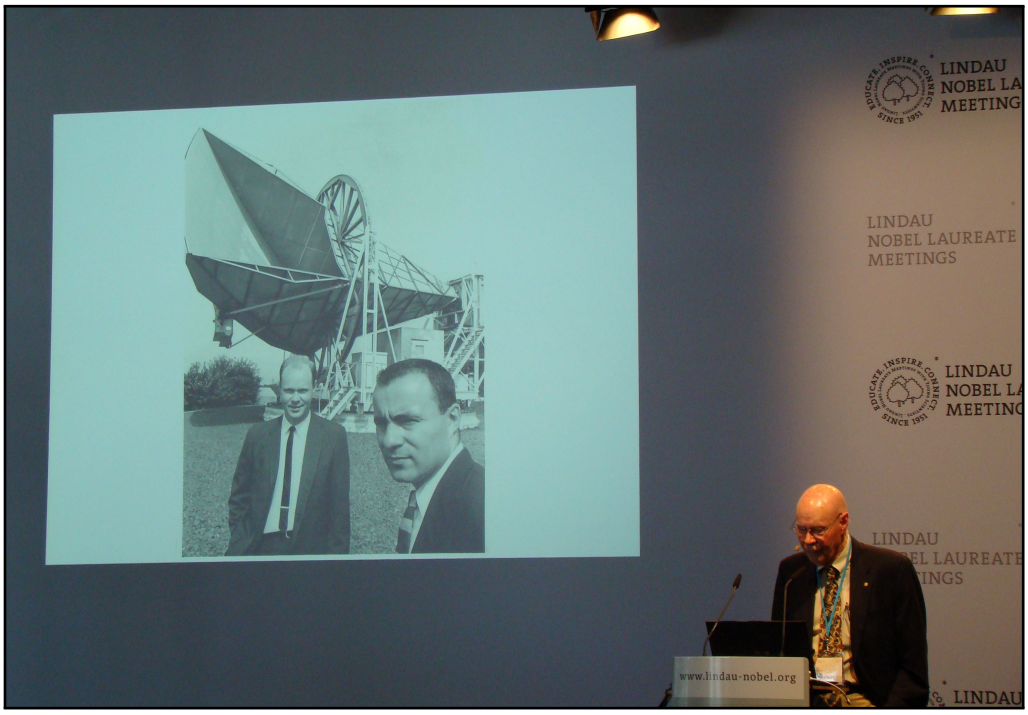

Figure 1.1: Robert Woodrow Wilson reporting about his famous discovery of the cosmic microwave background radiation at the 65th Lindau Nobel Laureate Meeting in 2015 [61]. In the photograph shown in this lecture, Robert W. Wilson (left) and Arno A. Penzias (right) stand in front of the "Holmdel Horn Antenna", a horn-reflector type [62] antenna [63] at Bell Laboratories (in Holmdel, New Jersey), which was originally constructed in 1959 to support "Project Echo" [64, 65], a pioneering satellite communications experiment. With this antenna, Wilson and Penzias discovered the cosmic microwave background radiation in 1964.

recorder (SUGAR) [69] in Australia were also able to detect cosmic rays with energies of about 10^{20} eV or beyond [70–72].

Cosmic rays with particle energies of about 10^{18} eV or more were found to be predominantly charged nuclei [73]. In fact, there could exist other cosmic particles like neutrinos or photons that reach such high energies, but a significant flux of such other particles at particle energies of 10^{18} eV or beyond could not be proven up to now. Instead, stringent limits highly confine their possible flux [74–80]. To distinguish the predominant cosmic charged nuclei with energies 10^{18} eV or more from the other possible highest-energy cosmic particles, the former are often referred to as *ultra-high energy cosmic rays* (UHECRs) [81]. UHECRs with energies beyond 10^{20} eV are sometimes referred to as "extremely high energy cosmic rays" (EHECRs) in the literature [82, 83]. Hence, UHECRs include all EHECRs, but not vice versa.

Great interest in the most energetic particles detected at the Earth led to the construction of new observatories for UHECRs with growing observation areas. On the northern hemisphere, the Telescope Array experiment, located in Utah (USA), has currently the largest observation area [84]. The presently largest detector for UHECRs in the world is the Pierre Auger Observatory [85]. It is located on the southern hemisphere in Argentina. The construction of this observatory started in 2002 and was completed in 2008 [85]. Its modular design allowed the Pierre Auger Observatory to start collecting data already in a partial configuration during the construction phase in 2004 [86]. Up to now, it collected the largest amount of UHECR data compared to all other existing detectors. The detection techniques used by the Pierre Auger Observatory are based on air-fluorescence detectors [87] and water-Cherenkov detectors [88].

The construction of the first air-fluorescence detectors for UHECRs in the 1960s did not lead to their successful detection [89–91]. This may be due to the use of too small mirrors and inadequate atmospheric conditions. An early successful detection of fluorescence light from an UHECR was achieved by Goro Tanahashi and collaborators at the end of the 1960s [92]. Later, the fluorescence-detector technique was applied in more sophisticated detectors such as "Fly's Eye" [93, 94] and its direct descendant, the "High-Resolution Fly's Eye" (HiRes) [95], which clearly demonstrated the potential of this

technique in the context of UHECRs [96]. One key difference between HiRes and its predecessor is – as is already reflected by their names – the higher resolution of HiRes that is achieved by larger mirrors and smaller pixels [97].

A large water-Cherenkov detector, often called "Porter's detector", was successfully developed at the end of the 1950s [98, 99]. Improved versions of water-Cherenkov detectors were later used in the "Haverah Park experiment", where water-Cherenkov detectors were distributed over an area of $12\,\mathrm{km}^2$ in North Yorkshire (UK) [71, 100]. The University of Leeds operated the Haverah Park experiment from 1967 until 1987. For the later Pierre Auger Observatory it was of great importance that the Haverah Park experiment was able to prevent the growth of microorganisms in a sealed container filled with water for multiple decades. Such a container is a crucial part of a water-Cherenkov detector whose optical properties could considerably be impaired by microorganisms. This experimental achievement demonstrated that stable operation of water-Cherenkov detectors is possible on long time scales. Today, water-Cherenkov detectors are used in the Pierre Auger Observatory in a version that is strongly enhanced compared to Porter's detector.

A more detailed historical overview regarding UHECRs can be found in Kampert and Watson [101]. Further important review articles concerning UHECRs are given by, e.g., Nagano and Watson [81], Sigl [102], Cronin [103], Kotera and Olinto [104], Letessier-Selvon and Stanev [105], and Watson [106].

Although UHECRs have been intensively investigated for more than half a century [57, 81, 107], several of the main questions regarding UHECRs are still unanswered [104]. UHECRs therefore remained as an important topic of research. Two of these crucial unresolved questions in high-energy astrophysics concern the origin of UHECRs [102, 108, 109] and the properties of their sources [102, 104, 110]. For example, it is not yet known from which particular astronomical sources UHECRs originate, what the chemical composition of the particles emitted at their sources is, and how the particles are accelerated [102, 111].

A way to address these fundamental issues is to make assumptions about the origin of UHECRs, the properties of their sources, and the UHECRs'

propagation through the universe, to simulate their propagation from their sources to the Earth under these assumptions, which constitute a particular astrophysical scenario, and to compare the simulation results with observational data of actual UHECRs measured at the Earth [112]. Typical observables for comparing the results of computer simulations and experiments are the energy spectrum [113], chemical composition [114], and distribution of arrival directions [115] of UHECRs reaching the Earth. This procedure allowed to make much progress in the last decades [109, 116–118], including the finding of indications for an extragalactic origin of UHECRs [119]. Candidates for extragalactic sources of UHECRs are, e.g., active galactic nuclei [120, 121] and starburst galaxies [122, 123].

Assuming that deflections of UHECRs by cosmic magnetic fields on the way from their sources to the Earth are not so strong that all information about the positions of the sources is lost, among the three observables the distribution of the arrival directions allows the most direct conclusions about the positions of the sources. In the last few years, strong efforts have been made to study the directional distribution of UHECRs arriving at Earth, and observational hints for an anisotropy in the arrival directions have been reported [124–127]. However, a statistically significant (significance level $s > 5\sigma$ with standard deviation σ) detection of an UHECR anisotropy was not possible until recently. The Pierre Auger Collaboration recently reported the discovery of a significant dipolar anisotropy ($s = 5.2\sigma$) for cosmic particles arriving with energies $E > 8\,\mathrm{EeV}$ [119]. This experimental work represents important progress towards the identification of the sources of UHECRs, but it still has some observational limitations. First, it focuses on the existence of a nonzero dipole moment in the orientational distribution of the arrival directions, as the statistics of the experimental data does not allow it to significantly prove higher-order multipole moments. Second, for similar reasons no higher arrival-energy ranges than $E > 8\,\mathrm{EeV}$ are taken into account. A third limitation arises from the observation of UHECRs at only a part of the sky [128]. By combining the data of the Pierre Auger Observatory with data from the Telescope Array, it has been possible to reach a full sky coverage for energies $E > 10\,\mathrm{EeV}$ [129, 130], but the data for this energy range did not allow one to find a significant ($s > 5\sigma$) anisotropy in the arrival directions and until writing of this section

there are no corresponding combined data for lower energies that show a significant anisotropy.

A promising way to get additional and independent information about the origin of UHECRs could be provided by "cosmogenic neutrinos", since they are not deflected by cosmic magnetic fields. These neutrinos are produced when UHECRs interact with cosmic background photons, e.g., from the CMB [66, 67] or extragalactic background light (EBL) [131, 132], while propagating through the universe. Since UHECRs and cosmic background photons exist, one can assume the existence of high-energy cosmogenic neutrinos [133]. However, up to now, their flux has not yet been measured. This is likely due to too small volumes and observation times of the present neutrino observatories. The largest of them is the IceCube Neutrino Observatory. It is located at the south pole and its construction was completed in December 2010 [134, 135]. Nevertheless, the Pierre Auger Observatory and IceCube Neutrino Observatory have provided upper limits for the flux of high-energy cosmogenic neutrinos [80, 136, 137]. Such predictions for the cosmogenic neutrino flux are important for next-generation neutrino detectors like GRAND 200k that are currently in the planning phase [138]. On the theoretical side, one-dimensional simulations of the propagation of UHECRs, the generation of cosmogenic neutrinos, and their flight to the Earth have been carried out and led to initial predictions for the neutrino flux [104, 139–141]. These simulations, however, had some significant limitations. Among them are the reduced number of spatial degrees of freedom and the fact that, e.g., a structured and spatially anisotropic extragalactic magnetic field (EGMF) [142–146], which can have a significant effect on the propagation of UHECRs [2, 147], cannot be directly and without approximations taken into account in one-dimensional simulations. As a workaround for this caveat of one-dimensional simulations, methods have been proposed that allow to post process the results of such one-dimensional simulations so that effects of an EGMF such as, e.g., magnetic suppression, are approximately incorporated retroactively [148, 149]. These approximative methods, however, often have very limited applicability, it is difficult to estimate the uncertainty associated with these approximations, and they cannot lead to an anisotropic distribution of the arrival directions of UHECRs.

Recently, a comparison between simulation results based on a one-di-

mensional astrophysical model and measurements from the Pierre Auger Observatory [114] yielded information on the energy spectrum and chemical composition of the UHECRs emitted at the sources. The most important assumptions that affect the simulation results concern the positions of the sources, the energy spectrum and chemical composition of the UHECRs at the sources, the CMB and EBL with which the UHECRs can interact, and the EGMF that bends the trajectories of charged particles. While the CMB is known with high accuracy and the influence of the EBL on the simulation results was recently addressed alongside other influences in Refs. Aab et al. [114] and Wittkowski et al. [1], the dependence of the simulation results on the other assumptions has not yet been studied in detail. Common simplifications in previous simulation studies are assuming a homogeneous distribution of the UHECR sources, although one can expect that the real sources are discrete objects that follow the mass distribution of the universe, and again one-dimensional simulations.

The objective of this work is to contribute to the solution of the most important questions in the context of UHECRs. This includes extending the knowledge about the sources of UHECRs, the properties of the sources, the propagation of UHECRs from their sources to the Earth, and the generation and propagation of high-energy cosmogenic neutrinos. For this purpose, the results of elaborate computer simulations of the propagation of UHECRs from their assumed sources to the Earth are presented and compared with recent experimental data. These simulations are highly complex and go beyond the simulations applied in previous studies that are described in the literature. Especially, they avoid the limitations of previous simulation studies and observational limitations mentioned further above. The enhanced simulations used for this work take into account all three spatial degrees of freedom, the cosmological time-evolution of the universe, discrete sources whose distribution follows the local mass distribution of the universe, all relevant interactions of UHECRs with cosmic background photons, i.e., with photons from the CMB and EBL, the generation and further propagation of secondary particles such as cosmogenic neutrinos, and deflections of the trajectories of charged particles in extragalactic and, where relevant, galactic magnetic fields. With the time-evolution of the universe, the simulations include cosmological effects such as the redshift evolution of

the photon background and the adiabatic expansion of the universe. Since the EGMF and galactic magnetic field are not yet known, the simulations involved realistic assumptions about these magnetic fields that are in line with the limited experimental information that are already available about them. Unlike the available experimental data on the distribution of the arrival directions of UHECRs, the results of the simulations are limited neither to a specific energy range nor to the consideration of particular multipole moments. Furthermore, the simulations correspond to a full sky coverage.

On the basis of these advanced simulations it is studied which energy spectrum and chemical composition of the UHECRs must be assumed at their sources to obtain an energy spectrum and a chemical composition of the simulated UHECRs arriving at the Earth that are in the best possible agreement with the corresponding data measured by the Pierre Auger Observatory. It is also studied how this depends on the EGMF and the source evolution.

To study the anisotropy in the arrival directions of UHECRs comprehensively, the associated angular power spectrum up to order 32 and its dependence on the arrival energies of the particles are considered. Moreover, the flux of high-energy cosmogenic neutrinos reaching the Earth and the influence of the EGMF on this flux are predicted. This work focuses on neutrinos with energies $E \geq 10^{17}\,\mathrm{eV}$, since for lower energies particle interactions in the intracluster medium cannot be neglected as sources of neutrinos [150].

The results of this work provide many important new insights in the context of UHECRs and high-energy cosmogenic neutrinos. They show, e.g., that the best-fitting energy spectrum and chemical composition at the sources depend strongly on the EGMF and the source evolution. Regarding the distribution of the arrival directions of the UHECRs it is found that this distribution has a pronounced dipolar anisotropy and rather weak higher-order contributions to the angular power spectrum. This finding agrees well with the recent observation of a dipolar anisotropy for UHECRs with arrival energies above $8 \cdot 10^{18}\,\mathrm{eV}$ by the Pierre Auger Observatory [119]. In contrast to earlier simulation studies [151–153], our results are in excellent agreement with the energy spectrum, chemical composition, as well as anisotropy of recent UHECR data collected by the Pierre Auger Obser-

vatory. Additionally, the results lead to important predictions for energy ranges and higher-order multipole moments that are not yet accessible by the existing observatories. With these features, this work can provide guidance for future experimental studies. Furthermore, the predictions for the flux of cosmogenic neutrinos are found to be consistent with upper limits determined by the Pierre Auger Observatory and IceCube Neutrino Observatory. The predicted cosmogenic neutrino flux is also found to be clearly below the three-year sensitivities of planned neutrino observatories, and it allows to estimate which detector size and detection time are necessary for the observation of the predicted cosmogenic neutrino flux. It is shown that neglecting the EGMF strongly affects the predictions for the cosmogenic neutrino flux. For the case of no EGMF, the results are also compared with the results of previous one-dimensional simulations from the literature.

This work is structured as follows. After a general introduction including a short historical overview in the present chapter 1, the journey of UHECRs from their sources to the Earth is described in chapter 2. Chapter 3 deals with the analysis of observations of UHECRs at the Earth and introduces the three observables for the investigation of UHECRs. In chapter 4, important methods that have been applied for the present work are presented. Results concerning the sources and their properties are described in chapter 5. Based on this, predictions regarding the propagation and arrival directions of UHECRs and the flux of cosmogenic neutrinos are presented in chapter 6. Finally, in chapter 7 a summary and an outlook for this work are given.

2 Journey of UHECRs

By the time UHECRs reach Earth, they have made a long journey from their sources to Earth. In the following, different parts of this journey will be discussed in more detail. The journey of UHECRs certainly begins at their sources, so section 2.1 discusses the possible, but still unknown, sources of UHECRs. UHECRs can arrive at Earth with their high observed energy only if they have been sufficiently accelerated before. Therefore, section 2.2 discusses various models for cosmic ray acceleration. During the propagation of the UHECRs from their sources to Earth, interactions with the cosmic photon backgrounds are also expected and need to be taken into account. In this light, section 2.3 discusses the propagation of UHECRs. There is evidence for the existence of a galactic magnetic field in the Milky Way. Due to the electric charge of the UHECRs, the influence of the galactic magnetic field on the UHECRs cannot be neglected. For this reason, section 2.4 deals with our galactic magnetic field. Similarly, the extragalactic magnetic field is important during the journey of UHECRs and needs to be taken into account. Consequently, section 2.5 deals with the extragalactic magnetic field. When the UHECRs hit the Earth's atmosphere and interact with it at the end of their long journey, extensive air showers are formed which are addressed in section 2.6. For completeness, the current detectors of the UHECRs, which are used to observe the extensive air showers and reconstruct the properties of the primary UHECRs, such as the energy, direction of arrival, and chemical composition, are discussed in detail in section 2.7.

2.1 Sources

Currently, the sources of the UHECRs are still unknown. A rough estimate of possible UHECR sources is provided by the "Hillas diagram". The origi-

nal Hillas diagram [154] has been frequently updated by many authors over the past decades (see, e.g., [104, 155]). An updated Hillas diagram is shown in Fig. 2.1. It shows various possible cosmic sites of UHECR acceleration like active galactic nuclei (AGN), gamma-ray bursts (GRBs), intergalactic medium (IGM) shocks, supernova remnants (SNRs), and other candidate sources depending on their observationally accessible size and characteristic magnetic field. In Fig. 2.1, only astrophysical objects above the red line can accelerate iron nuclei to energies above 10^{20} eV. Similarly, astrophysical objects above the blue line are candidates for the acceleration of protons to energies above 10^{21} eV. Obviously, UHECRs observed on Earth with energies higher than 10^{20} eV cannot be explained by SNRs, but SNRs are believed to be important sources of the less energetic galactic cosmic rays in the literature [156–160].

The basic idea behind the Hillas diagram is that the maximum energy a particle can reach in cosmic accelerators is limited by the size and the magnetic field of their accelerating region. A particle can remain in the accelerating region as long as its Larmor radius is smaller than the extent of the accelerator region. The acceleration stops when the Larmor radius of the particle exceeds the radius of the accelerator region and the particle escapes. This yields the maximum energy $E_{\max}$ that a particle of electric charge Ze (with the atomic number Z and elementary charge e) can gain in a cosmic UHECR accelerator of size R and with characteristic magnetic field B to:

$$E_{\max} \sim cZeBR\,. \tag{2.1}$$

This is the well-known "Hillas criterion" with the speed of light in vacuum c. Because of the dependence on Z, it follows directly from this condition that heavy nuclei, such as iron nuclei with $Z = 26$, are accelerated by the sources to higher maximum energies than light nuclei, such as protons with $Z = 1$. Assuming for simplicity that the chemical composition of UHECRs does not change significantly during their propagation from their sources to Earth, it can also be suggested on the basis of this criterion that the chemical composition of UHECRs observed at Earth should shift to heavier elements at the highest particle energies. Such expected behavior does not appear to contradict current observations, but the reader is referred to section 3.2 for more information on the chemical composition of UHECRs. Nonetheless it

should be noted that the Hillas criterion is a necessary but not a sufficient condition for cosmic accelerators. This is a reason why the sources of the UHECRs are still unknown. It is clear that the actual sources should fulfill additional conditions beyond the highly simplifying Hillas criterion. For example, the actual sources should be able to generate enough particles to explain the total observed flux of cosmic rays (see section 3.1). Furthermore, the sources should ensure that the energy lost by the accelerated particles by, e.g., radiation in the cosmic accelerator should not exceed the energy gained in the cosmic accelerator. Anyway, the Hillas diagram is a very useful estimate that helps to select particular sources as promising candidates.

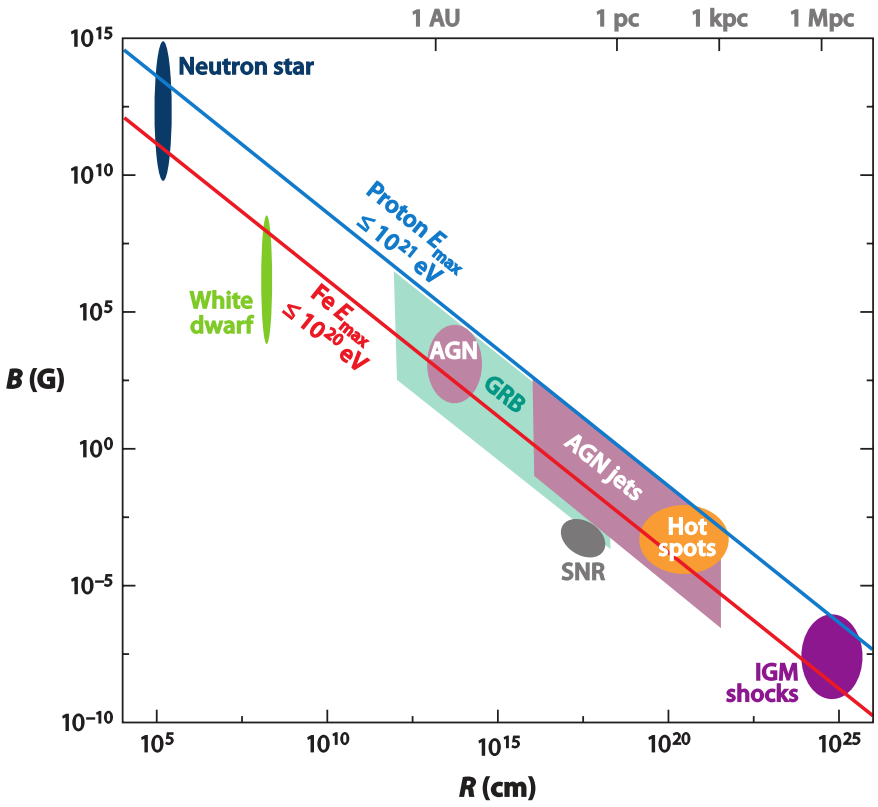

Figure 2.1: Updated Hillas diagram showing various possible cosmic sites of UHECR acceleration, such as active galactic nuclei (AGN), gamma-ray bursts (GRBs), intergalactic medium (IGM) shocks, supernova remnants (SNRs), and other candidate sources depending on their size R and characteristic magnetic field B. Astrophysical objects below the red line cannot accelerate iron nuclei to 10^{20} eV. To accelerate protons to energies above 10^{21} eV, only astrophysical objects above the blue line come into consideration. Figure: from Fig. 8 in [104].

2.2 Acceleration

The important question how the UHECRs observed at Earth are accelerated at their sources to extraordinarily high energies of 10^{20} eV and beyond, which corresponds to a macroscopic amount of energy of about 16 J or more for individual microscopic particles, is still unanswered. Finding an answer to this question is an extremely daunting challenge due to the fact that the sources of UHECRs (see section 2.1) are unknown. Otherwise, one could learn much about the acceleration mechanism by direct observations. Nonetheless, it should be noted that a vast number of articles exist presenting theories for the acceleration of UHECRs. In this context, the interested reader is referred to the many remarkable articles reviewing progress in the theoretical description of the acceleration of cosmic rays that have been published especially in the last half century. Examples are the publications of Drury [161], Blandford and Eichler [162], Jones and Ellison [163], Kirk and Duffy [164], Malkov and Drury [165], and Bell [166]. In the following, after a motivation how stochastic acceleration can lead to a power-law energy spectrum, a few important acceleration mechanisms like *Fermi acceleration* and *acceleration by unipolar inductors* are briefly discussed. The different acceleration mechanisms have in common that they are characterized by the transfer of energy from a macroscopic object, such as a shock front, moving magnetized plasma cloud, or fast rotating neutron star, to individual charged particles.

2.2.1 Motivation

In the following, it will be motivated by a simple example that stochastic acceleration can naturally lead to a power-law energy spectrum, as is expected for the accelerators of UHECRs based on the observations at Earth (see section 3.1 for more details on the energy spectrum of cosmic rays observed at Earth).

Assume a particle with initial energy E_0 and an acceleration process in which the particle's energy is increased proportional to the particle's current energy with each acceleration cycle [167]. In the 1st acceleration cycle, the particle energy then increases to $E_1 = E_0(1+\epsilon)$, where $\epsilon > 0$ is the relative energy gain per acceleration cycle. After the k-th acceleration cycle, the

particle has thus an energy $E_k = E_0(1+\epsilon)^k$. Consequently, to reach the final energy $E_k = E$, a number of

$$k = \frac{\ln(E/E_0)}{\ln(1+\epsilon)} \tag{2.2}$$

acceleration cycles is needed [168]. Let P (with $0 \leq P < 1$) be the probability per acceleration cycle that the particle leaves the accelerator region and will not be accelerated any further. Then, $(1-P)^k$ is the probability that the particle remains in the accelerator region during k acceleration cycles. So the number of particles with energies equal to or greater than E is given by

$$N(\geq E) \propto \sum_{j=k}^{\infty}(1-P)^j \,. \tag{2.3}$$

Taking advantage of equation (2.3) and the closed-form formula for the geometric series

$$\sum_{j=0}^{n} x^j = \frac{1-x^{n+1}}{1-x} \qquad \text{for } |x| < 1 \tag{2.4}$$

with the limiting case

$$\sum_{j=0}^{\infty} x^j = \frac{1}{1-x} \qquad \text{for } |x| < 1, \tag{2.5}$$

one obtains

$$N(\geq E) \propto \sum_{j=0}^{\infty}(1-P)^j - \sum_{j=0}^{k-1}(1-P)^j = \frac{(1-P)^k}{P} \,. \tag{2.6}$$

Using equations (2.2), (2.6), and $a^{\ln(b)} = b^{\ln(a)}$ results in

$$N(\geq E) \propto \frac{1}{P}\left(\frac{E}{E_0}\right)^{1-\tilde{\gamma}} \propto E^{1-\tilde{\gamma}} \,. \tag{2.7}$$

This is the integral form of a power-law energy spectrum with $\tilde{\gamma} = 1 - \frac{\ln(1-P)}{\ln(1+\epsilon)}$. The derivation shows also that, as the final particle energy E increases, it takes an increasing number of acceleration cycles and thus an increasing time to accelerate the particles. A limited accelerator lifetime would therefore be directly linked to a maximum particle energy.

2.2.2 Second-order Fermi acceleration

In 1949, Enrico Fermi presented a possible acceleration mechanism for cosmic rays [169]. It represents a famous example of a stochastic acceleration mechanism [170]. This mechanism, nowadays called second-order Fermi acceleration, is based on the scattering of ultra-relativistic, charged particles at randomly distributed magnetized plasma clouds in interstellar space. The energy gain through second-order Fermi acceleration will be discussed following [171].

Suppose that a particle of speed v and energy E_1 is ultra-relativistic ($v \approx c$) and that it enters a magnetized plasma cloud moving with speed $u = \|\vec{u}\| = \beta c$ under the angle θ_1. Here, β is the speed of the magnetized plasma cloud relative to the speed of light in vacuum c. The geometry of the scattering is shown in Fig. 2.2. After multiple isotropic scattering

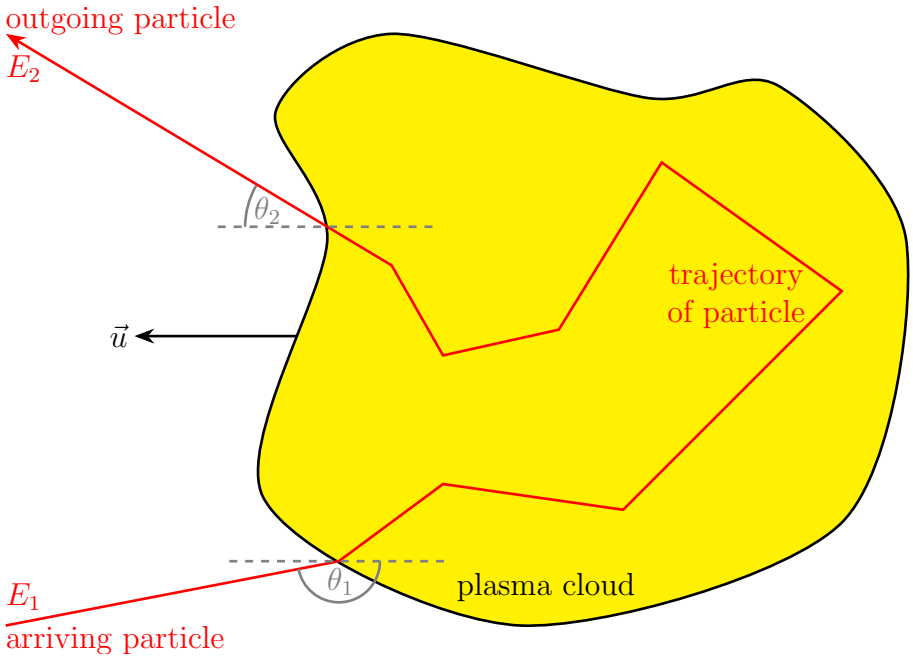

Figure 2.2: Sketch showing the geometry of scattering off a plasma cloud in second-order Fermi acceleration.

(in the cloud's reference frame) within the magnetized plasma cloud, the particle leaves the cloud with an energy E_2 at an angle θ_2. Quantities in the reference frame of the cloud will be denoted by a superscript $^\diamond$ in this section. By means of Lorentz transformation, the energy $E_1^\diamond$ of the arriving

particle in the reference frame of the cloud is given by

$$E_1^\diamond = \gamma_\mathrm{L} E_1 (1 - \beta \cos(\theta_1)) \,. \tag{2.8}$$

Here, $\gamma_\mathrm{L} = \frac{1}{\sqrt{1-\beta^2}}$ is the Lorentz factor. It can be assumed that, similar as for a magnetic mirror, the particle is scattered elastically in the reference frame of the cloud:

$$E_1^\diamond \approx E_2^\diamond \,. \tag{2.9}$$

One can also assume that, in the reference frame of the cloud, the particles are randomly scattered in all directions so that $\langle \cos(\theta_2^\diamond) \rangle = 0$ applies. For the energy E_2 in the laboratory system, a Lorentz transformation yields

$$E_2 = \gamma_\mathrm{L} E_2^\diamond (1 + \beta \cos(\theta_2^\diamond)) \,. \tag{2.10}$$

Thus, by means of equations (2.8)-(2.10), one obtains:

$$E_2 = \gamma_\mathrm{L}^2 E_1 (1 + \beta \cos(\theta_2^\diamond))(1 - \beta \cos(\theta_1)) \,. \tag{2.11}$$

However, the average value of θ_1 depends on the geometry of the scattering. The collision probability is a function of the relative speed $v_\mathrm{r} = v - u\cos(\theta_1)$ between the cloud and the particle. Hence, with the abbreviation $\tilde{x} = \cos(\theta_1)$, one obtains

$$\langle \cos(\theta_1) \rangle = \frac{\int_{-1}^{+1} \tilde{x}(v - u\tilde{x}) \,\mathrm{d}\tilde{x}}{\int_{-1}^{+1} (v - u\tilde{x}) \,\mathrm{d}\tilde{x}} = -\frac{1}{3}\frac{u}{v} \approx -\frac{1}{3}\beta \,. \tag{2.12}$$

In the last approximation, it was utilized that the particles are ultra-relativistic, i.e., $v \approx c$. The preceding considerations and in particular equation (2.11) result in

$$\langle E_2 \rangle = E_1 \frac{1 + \frac{\beta^2}{3}}{1 - \beta^2} = E_1 \left(1 + \frac{4}{3}\beta^2 + \mathcal{O}(\beta^4) \right) . \tag{2.13}$$

This yields the average relative energy gain

$$\left\langle \frac{\Delta E}{E} \right\rangle = \frac{\langle E_2 \rangle - E_1}{E_1} \approx \frac{4}{3}\beta^2 \propto \beta^2 \,. \tag{2.14}$$

The average relative energy gain increases with β^2, which means that it is

proportional to the square of the speed of the plasma cloud. This is the reason why this mechanism is nowadays called second-order Fermi acceleration. Assuming that the cloud has a typical speed $u \approx 15\,\mathrm{km/s}$ [169] leads to $\beta \approx 5 \cdot 10^{-5}$ and $\beta^2 \approx 3 \cdot 10^{-9}$. Thus, the average relative energy gain is quite small, suggesting that the mechanism is not very efficient.

2.2.3 First-order Fermi acceleration

A more efficient acceleration than the interaction with plasma clouds, which was discussed in the previous chapter 2.2.2, is given by first-order Fermi acceleration, which is also referred to as diffusive shock acceleration (DSA). The theory of first-order Fermi acceleration is reviewed, e.g., in [162]. This acceleration mechanism can take place at shocks in different astrophysical environments [172, 173], such as supernova shocks. The energy gain of this mechanism is proportional to β:

$$\left\langle \frac{\Delta E}{E} \right\rangle \propto \beta\,. \tag{2.15}$$

This is the reason why this mechanism is nowadays called first-order Fermi acceleration.

In the case of relativistic shocks, for the energy spectrum emitted at the source a spectral index γ (see section 3.1) of the range $\gamma \approx 2.1$-2.3 is predicted [174–176]. For acceleration at nonrelativistic shocks, a spectral index $\gamma \approx 2$ is predicted for the spectrum emitted at the source [161].

2.2.4 Acceleration by unipolar inductors

As another way for accelerating particles to ultrahigh-energies, unipolar inductors were proposed [177, 178]. Fast rotating compact objects with a strong magnetic field, which include numerous neutron stars, are able to induce strong electric fields capable of accelerating particles to ultra-high energies. Such fast rotating neutron stars are often associated with relativistic winds [179–181].

Neutron stars are spherical objects of high density [182] with a typical radius R_* of about 10 km [183]. A massive star with mass $M > 8M_\odot$ ($M_\odot$ is the solar mass) [184] can become a neutron star at the end of the stellar

evolution. If the mass of the star is too high, instead of a neutron star a black hole is formed. In contrast, if the mass is too low, a white dwarf is formed at the end of the stellar evolution. A neutron star can also be formed when a white dwarf of a binary system exceeds the Chandrasekhar limit [185] after accreting mass from its companion [186, 187].

Typically, a newborn neutron star rotates fast [188] and has a strong magnetic field. The mass M_* of neutron stars is theoretically limited upwards by the Tolman-Oppenheimer-Volkoff limit [189, 190]. Nevertheless, more recent works present slightly differing values for the maximum mass of neutron stars [191, 192]. Neutron stars with particularly strong magnetic fields are known as magnetars [193–195]. Magnetars exhibit magnetic fields of typically 10^{13}-$10^{15}\,\mathrm{G}$ [196]. However, also some ultra-long-period magnetars could exist [197].

The idea that UHECRs can be accelerated by unipolar induction in the relativistic winds of rapidly rotating magnetars has been the subject of discussion in [104, 177, 178] and led to the conclusion that the maximum energy that a particle with atomic number Z can reach by this process can be approximated by

$$E_{\mathrm{UI}} \approx Z \frac{\eta_*}{0.1} \frac{B_*}{10^{15}\,\mathrm{G}} \left(\frac{R_*}{10\,\mathrm{km}} \right)^3 \left(\frac{\Omega_*}{10^4\,\mathrm{s}^{-1}} \right)^2 10^{21}\mathrm{eV}\,. \tag{2.16}$$

Here, η_* parameterizes the fraction of the voltage drop acting on the particle, B_* is the magnetic flux density, R_* the radius of the neutron star, and Ω_* its angular frequency. When particles are accelerated by this kind of acceleration mechanism, for the energy spectrum emitted at the source a spectral index of $\gamma \approx 1$, corresponding to a quite hard energy spectrum, is possible [104].

2.2.5 Further acceleration mechanisms

Besides the famous acceleration mechanisms presented before (see sections 2.2.2-2.2.4), further possible acceleration mechanisms can be found in the literature. Examples are wakefield acceleration [198–200] and magnetic reconnection [201–203]. In addition, shear acceleration [204–206] should not remain unmentioned. Reference [207] and other publications criticize that

this mechanism has been discussed relatively little in the literature.

2.3 Propagation

As UHECRs propagate through the universe, they interact with cosmic background photons γ_{bp}. Important interactions in this context are electron pair production, photopion production and photodisintegration. Assuming the UHECR that interacts with a cosmic background photon is a proton p, electron pair production can be described by:

$$p + \gamma_{\mathrm{bp}} \rightarrow p + e^- + e^+ \,. \tag{2.17}$$

Still assuming that the UHECR is a proton, photopion production by interaction with a cosmic microwave background photon via the Δ resonance can be described by [66, 67]:

$$p + \gamma_{\mathrm{bp}} \rightarrow \Delta^+ \rightarrow \begin{cases} p + \pi^0 \\ n + \pi^+ \,. \end{cases} \tag{2.18}$$

Assuming that the UHECR interacting with the cosmic background photon is a nucleus X heavier than a proton with atomic number Z and mass number A, then two examples for a possible photodisintegration that also can change nucleus X to $X^{\#}$, if Z decreases, are given by

$${}^{A}_{Z}X + \gamma_{\mathrm{bp}} \rightarrow {}^{A-1}_{Z-1}X^{\#} + p \,, \tag{2.19}$$

$${}^{A}_{Z}X + \gamma_{\mathrm{bp}} \rightarrow {}^{A-1}_{Z}X + n \rightarrow {}^{A-1}_{Z}X + p + e^- + \bar{\nu}_e \,. \tag{2.20}$$

For the secondary free neutron n of equation (2.20), which is undergoing beta decay $n \rightarrow p + e^- + \bar{\nu}_e$, the mean decay path length is given by $9.2(E/\mathrm{EeV})\,\mathrm{kpc}$ [208]. Thus, it will usually have been decayed on extragalactic distance scales.

The whole universe is filled with cosmic background photons. Most relevant for UHECR propagation are the photons from the cosmic microwave background (CMB) and the photons from the extragalactic background light (EBL). As already mentioned in the introduction, the CMB was discovered by Arno Penzias and Robert Woodrow Wilson (see Fig. 1.1 on page 4) in 1964. Photons from the CMB are the oldest electromagnetic radiation that can be observed on Earth and originate from the epoch of recombination,

which can be roughly dated to $4 \cdot 10^5$ years after the Big Bang [209, 210]. The spectrum of the CMB is much better known than that of the EBL. The spectrum of the today observable CMB is very close to the spectrum of a perfect blackbody of temperature $T_0 = 2.7\,\mathrm{K}$ [211].

The extragalactic background light consists of all the accumulated radiation emitted by stars and accreting compact objects since the epoch of star and galaxy formation [212]. Direct measurements of the EBL are very challenging. In particular, they are hampered by galactic and other foreground emissions, such as zodiacal light [213–215]. That is also one of the reasons why there are different EBL models today such as [216, 217]. In the following, the latter and more recent Gilmore EBL model is used.

The propagation of UHECRs in the universe and their interactions with the photons of the CMB and EBL strongly depend on the chemical composition of the UHECRs and their energy. This can clearly be seen in Fig. 2.3 and Fig. 2.4. Figure 2.3 shows the propagation of an initial iron (^{56}Fe) nucleus over a distance of 10 Mpc in the EGMF of Das et al. for two different initial energies $E_0 = 5 \cdot 10^{20}\,\mathrm{eV}$ and $E_0 = 10^{21}\,\mathrm{eV}$. Effects of interactions with cosmic background photons during propagation (such as photodisintegration) are clearly visible. Figure 2.4 shows similar things as Fig. 2.3, but now instead of the propagation of an initial iron nucleus the propagation of an initial silicon (^{28}Si) nucleus is shown. In Fig. 2.4, one can also see effects of interactions with cosmic background photons during propagation (such as photodisintegration). As expected, the deflections of the particles in the extragalactic magnetic field decrease with increasing particle energies and decreasing atomic number of the initial UHECR. Further, a heavier nucleus, such as an iron nucleus in this example, can photodisintegrate into more particles than the lighter ^{28}Si nucleus, which can be seen in the aforementioned figures.

An excellent way to visualize at which chemical composition and at which particle energy which of the aforementioned processes is relevant is to visualize the energy loss length [167, 218] as a function of the particle energy for nuclei of different chemical compositions. In this work, the energy loss length was calculated based on the interaction rate tables of CRPropa 3 as described in Ref. [218]. Figure 2.5 clearly shows which interaction at which energy is most relevant for certain exemplary nuclei. Figure 2.5 (a)

shows for primary protons that in the energy range roughly between 2 and 50 EeV pair production on the CMB is the most relevant interaction, while for energies roughly below 2 EeV redshift losses from the expanding universe are most relevant. For $E \gtrsim 50\,\mathrm{EeV}$ it can be clearly recognized that the most important interaction is the well known GZK effect [66, 67] with pion production on the CMB. Here the EBL provides only a minor contribution, while for heavier nuclei the behavior is much different, which is shown in Fig. 2.5 (b)-(d). One can also see from Fig. 2.5 (c)-(d) that for the energies $E_0 = 5 \cdot 10^{20}\,\mathrm{eV}$ and $E_0 = 10^{21}\,\mathrm{eV}$ previously considered for iron nuclei and silicon nuclei, photodisintegration (on the CMB) is the most relevant process. Since the energy loss length is relatively small for these energies and nuclei, the nuclei photodisintegrate quite quickly in Fig. 2.3 and Fig. 2.4. It is also worth mentioning that at an energy of 100 EeV the energy loss length for protons and iron nuclei is roughly one order of magnitude greater than the energy loss length of intermediate mass nitrogen nuclei, for example.

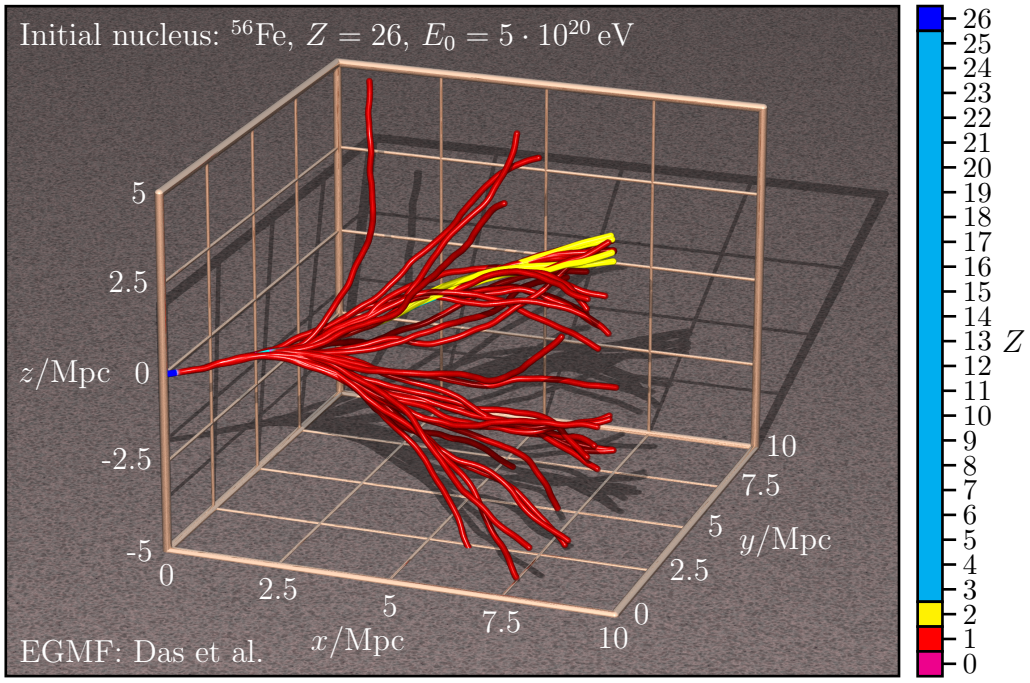

(a)

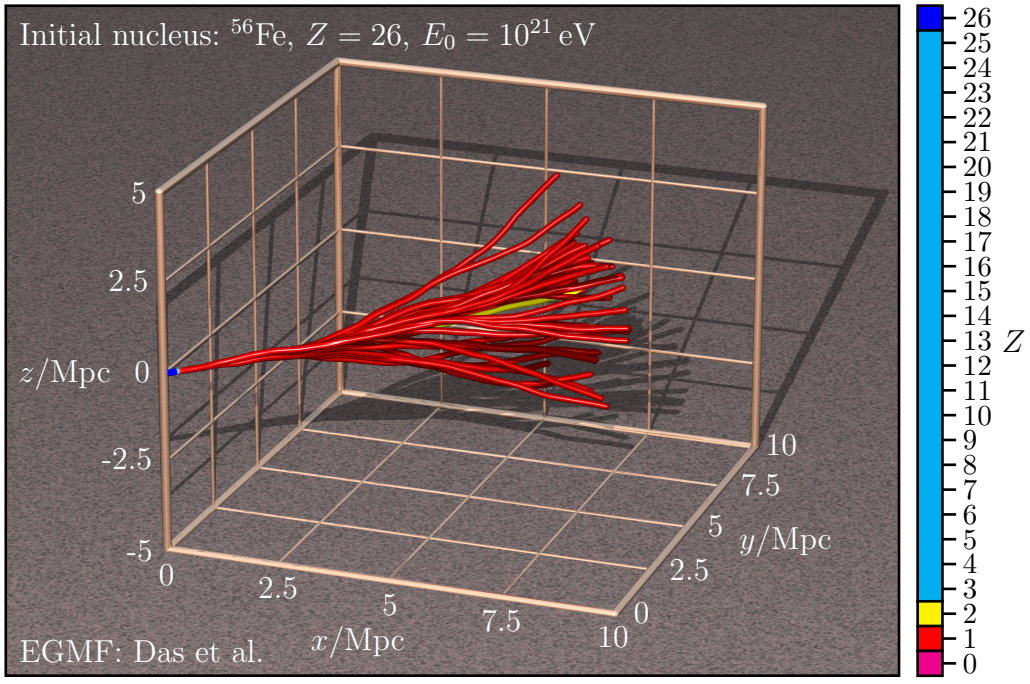

(b)

Figure 2.3: Propagation of an initial iron (^{56}Fe) nucleus over a distance of 10 Mpc in the EGMF of Das et al. for different initial energies E_0. Effects of interactions with cosmic background photons during propagation (such as photodisintegration) are clearly visible.

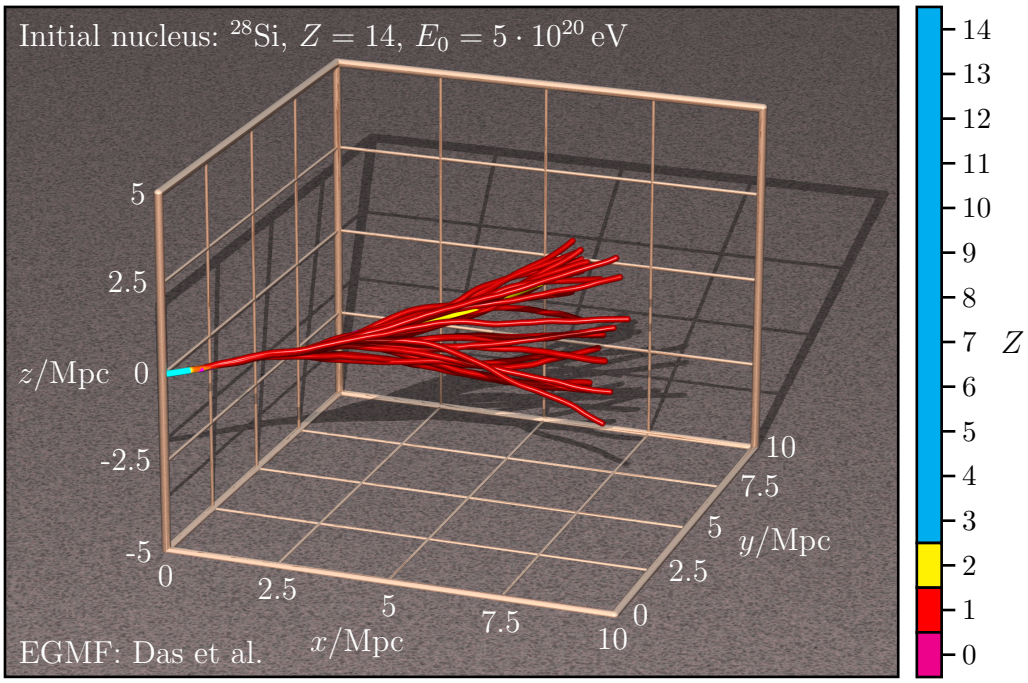

(a)

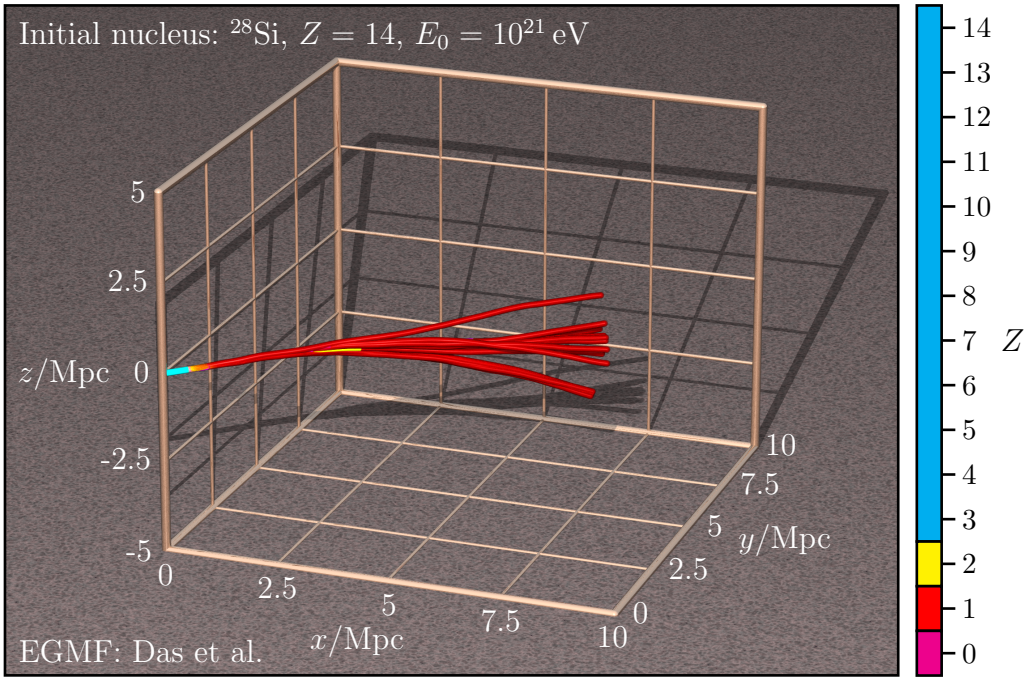

(b)

Figure 2.4: Similar as in Fig. 2.3, but now for an initial silicon (^{28}Si) nucleus.

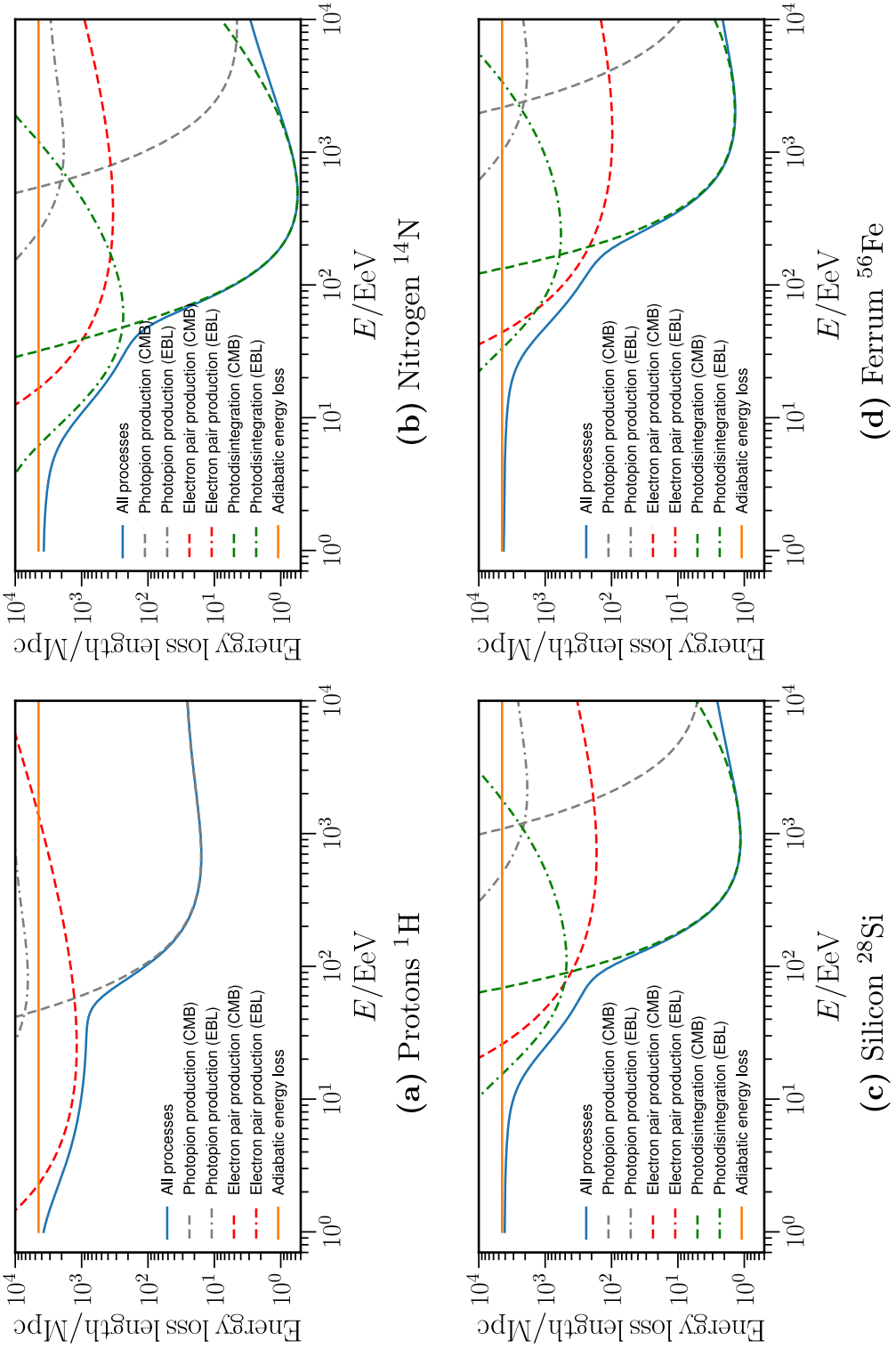

Figure 2.5: Energy loss lengths for four exemplary nuclei calculated with CRPropa 3. For the extragalactic background light (EBL) the Gilmore model [217] is used. Various contributions from different interactions with CMB and EBL photons are shown.

2.4 Galactic magnetic field

After many decades of intensive research, there seems to be consensus that magnetic fields are ubiquitous within the Milky Way and other galaxies of all types [219, 220]. One of the first known discoveries of the existence of extraterrestrial magnetic fields, the magnetic fields in sunspots observed by G. E. Hale, is already more than a century ago [221]. This famous observation was based on the Zeeman effect [222, 223]. In the following years, much improvements and important observations in radio astronomy have been archived, such as the discovery of the radio source Cygnus A by G. Reber and further investigation of it by J. S. Hey and his colleagues in 1946 [224, 225]. Early measurements of the galactic magnetic field (GMF) based on Faraday rotation were reported more than half a century ago [226, 227]. In these measurements, extragalactic polarized radio sources were used. In the 1970s, also measurements based on pulsars were performed [228].

An important achievement of the present millennium was the spacecraft-based investigation of the GMF using synchrotron emission data as measured, e.g., by the WMAP (Wilkinson Microwave Anisotropy Probe) spacecraft [229]. For this purpose, observations are typically performed at a sufficiently high frequency (e.g., 22 GHz, corresponding to a wavelength of about 1.4 cm) to neglect Faraday rotation of the synchrotron emission data [230].

The most distant space probe from Earth is the world-famous "Voyager 1" with a distance of about 166 au (in 2024) from Earth and this space probe is able to measure magnetic fields [231–233]. Also the identically constructed sister probe "Voyager 2", which is less distant from the Earth with a distance of about 139 au (in 2024), provides measurements with its magnetometer [234, 235]. Nonetheless, the distance that these space probes have travelled up to now is almost negligible compared to the dimensions of the Milky Way. Due to the large size of the Milky Way, its magnetic field (the GMF) cannot be measured directly by in-situ measurements of space probes, so indirect measurement methods have to be used.

Complementary information about the GMF can be achieved by Faraday rotation measure (RM) and polarized synchrotron radiation data. While RM data allow to get information about the component of the magnetic field

parallel to the line-of-sight (LOS) $B_\parallel$, polarized synchrotron radiation data give information about the magnetic field perpendicular to the LOS $B_\perp$. The *rotation measure* RM, which is usually measured in units of $\mathrm{rad\,m^{-2}}$, is given by

$$\begin{aligned} \mathrm{RM} &= \frac{e^3}{8\pi^2\varepsilon_0 m_e^2 c^3} \int_0^d n_e(s) B_\parallel(s)\,\mathrm{d}s \\ &\approx 2.62 \cdot 10^{-13}\mathrm{T}^{-1} \int_0^d n_e(s) B_\parallel(s)\,\mathrm{d}s \\ &\approx 0.81 \int_0^d \left(\frac{n_e(s)}{\mathrm{cm}^{-3}}\right)\left(\frac{B_\parallel(s)}{\mu\mathrm{G}}\right)\left(\frac{\mathrm{d}s}{\mathrm{pc}}\right)\mathrm{rad\,m^{-2}} \end{aligned} \tag{2.21}$$

Here, e is the elementary charge, ε_0 the electric constant, m_e the electron rest mass, c the speed of light in vacuum, $n_e(s)$ the total density of ionized electrons at point s [236], that is dominated by the thermal electron density, and $B_\parallel(s)$ is the component of the magnetic field parallel to the LOS at point s. One integrates over the full propagated path, from the origin ($s = 0$) to the observer at Earth ($s = d$), of the Faraday-rotated electromagnetic radiation. The *dispersion measure* DM of pulsars in our galaxy, with $\mathrm{DM} \propto \int_0^D n_e(s)\,\mathrm{d}s$ [228], offers a possibility to obtain information about $n_e(s)$ experimentally. Here, D is the distance from the pulsar to the observer at Earth along the LOS. The relation between the Faraday rotation angle Ψ and the wavelength λ of the rotated electromagnetic radiation is given by:

$$\Psi = \Psi_0 + \mathrm{RM}\,\lambda^2\,. \tag{2.22}$$

Here, Ψ_0 takes a possible intrinsic Faraday rotation in the sources into account. For example, typical interstellar rotation measures of about $50\,\mathrm{rad\,m^{-2}}$ would lead for $\lambda = 21\,\mathrm{cm}/(\lambda = 3\,\mathrm{cm})$ to a Faraday rotation of approximately $126°/(3°)$ [237]. To determine the RM, measurements of the Faraday rotation angle Ψ over a suitable frequency range are usually performed. Measurements at different frequencies are required to determine the RM without ambiguities. Next-generation radio telescopes like the Square Kilometre Array (SKA) are believed to give, especially through an extensive number of RMs, further insights into the cosmic magnetism in the future [238–241].

Since RM and polarized synchrotron radiation data provide complementary information about linearly independent components of the magnetic

field in the LOS, recent GMF models make extensive use of both of these types of experimental data. A recent, contemporary, popular, and important GMF model is the Jansson and Farrar GMF model (JF12 model) [230, 242]. The JF12 model was created under consideration of a huge set of Faraday rotation measurements and synchrotron radiation data. In this model, the GMF comprises three distinct components. A regular, a turbulent isotropic, and a turbulent anisotropic (called "striated") magnetic field component. In Refs. [243, 244], deflections of UHECRs in the JF12 model are extensively studied. The former work also makes a comparison with an older model for the GMF.

An impression of the influence of the JF12 model on the propagation of UHECRs can be obtained from Fig. 2.6. In this figure, exemplary trajectories of UHECRs that propagate through the JF12 model and reach the Earth are shown for three different UHECR rigidities $E/(Ze)$. The Galactic border is modeled as a sphere of radius 20 kpc around the Galactic center. As expected, there are decreasing deflections for increasing UHECR rigidities. Furthermore, it can be seen that, as one might expect, UHECRs that pass the Galactic center closely are deflected particularly strongly.

There exists a plenty of literature about the GMF. Progress in GMF observations is described, e.g., in Refs. [236, 245, 246]. Interesting review articles for further reading are Refs. [237, 247].

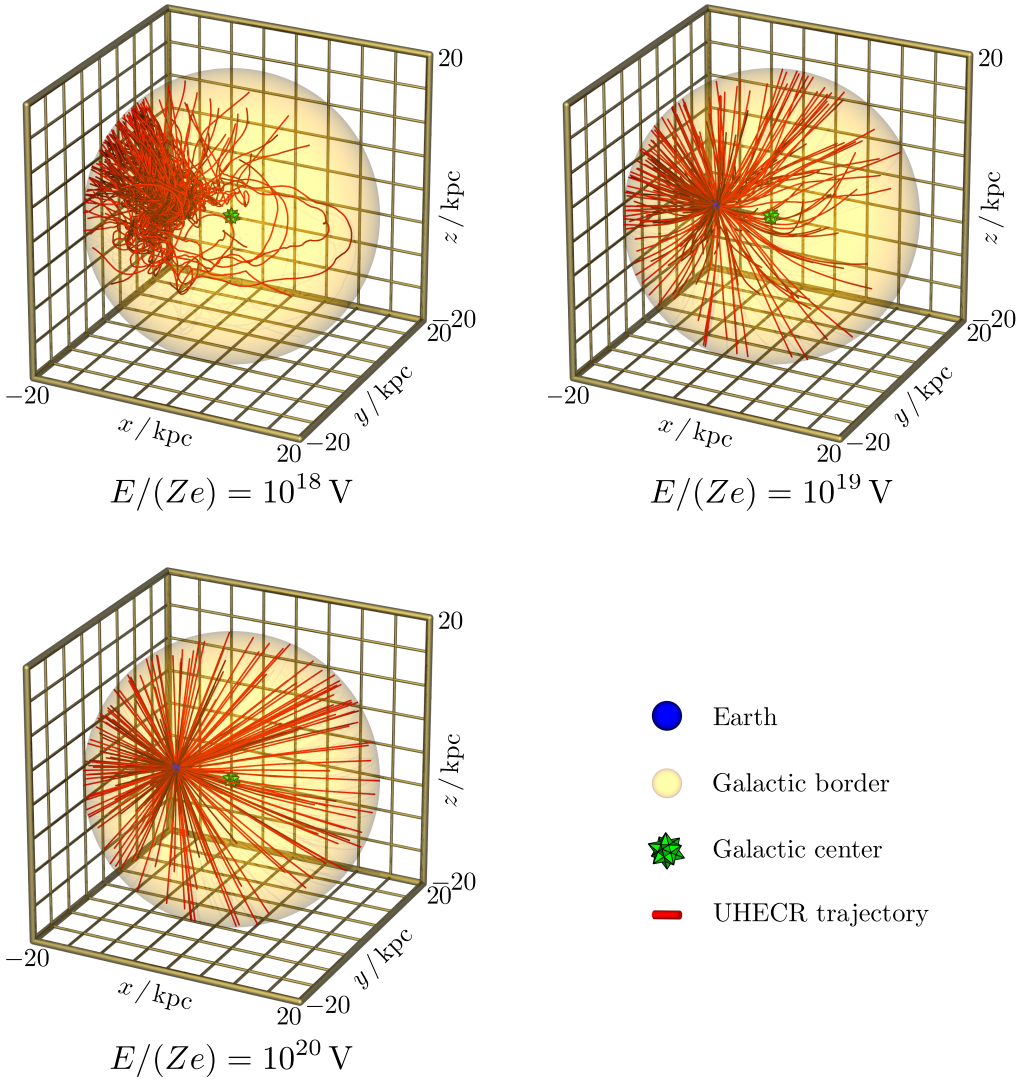

Figure 2.6: Exemplary UHECR trajectories (red) in the JF12 galactic magnetic field model that reach the Earth (blue sphere). The Galactic border (yellow sphere) is modeled as a sphere of radius 20 kpc around the Galactic center (green small stellated dodecahedron). Results are shown for three different UHECR rigidities $E/(Ze)$. The deflections of the trajectories decrease for increasing UHECR rigidities.

2.5 Extragalactic magnetic field

The knowledge about the extragalactic magnetic field is much less than the knowledge about the magnetic field in our galaxy (see section 2.4). An interesting article discussing observational methods for the detection and the measurement of the extragalactic magnetic field is given in Kronberg [142]. The answer to the important question, how the cosmic magnetic fields were generated, is still pending. Interesting reviews discussing possible mechanisms for the generation of cosmic magnetic fields can be found in Refs. [248, 249]. Observations indicate that in clusters magnetic fields of the order of 10^{-6} G and up to the order of 10^{-5} G at the center of clusters are not seldom [250–253]. For cosmic voids, that fill in comparison to clusters and filaments most of the volume of the Universe [254], magnetic fields in the range of 10^{-16} G [255, 256] to 10^{-9} G [257, 258] are expected. For cosmic filaments, magnetic flux densities lower than the values for clusters and higher than the values for voids are expected.

In the literature, many different models for the extragalactic magnetic field can be found. For a comparison of some recent models for the extragalactic magnetic field with regard to the cumulative filling factors, please consult Refs. [147, 259]. Starting from simple models assuming an uniformly distributed cosmic magnetic field up to recent strongly structured models (e.g., [113, 143, 146, 260]) in which often the cosmic magnetic field is correlated with the large-scale density structure of the universe, a considerable number of extragalactic magnetic field models exist. An important and strongly structured model for the extragalactic magnetic field is the model proposed in [261], which is sometimes called in the literature "benchmark field" [115]. This EGMF model, in the following called Benchmark EGMF, is based on the Dolag model [144] for the mass distribution and the Miniati model [143, 262] for the magnetic field in the universe. The Dolag model for the mass distribution is a prominent model for the local mass distribution of the universe, in which, inter alia, the positions and masses of prominent galaxy clusters largely coincide with their real counterparts. A huge advantage of the constrained Dolag model for the mass distribution is that, in contrast to other unconstrained models like [113, 146, 263], there is no ambiguity in the choice of the Earth's position. For a most realistic inter-

pretation of the observations on Earth, the use of a constrained simulation is preferable to the use of an unconstrained simulation. Since the Benchmark EGMF is based on the constrained Dolag model for the mass distribution, the position of the Earth is in the Benchmark EGMF also fixed.

A different and strongly structured model for the extragalactic magnetic field is the model of Das et al. [113]. Using a novel turbulence dynamo model [145], the researchers calculated their model for the extragalactic magnetic field. A comparison of these two strongly structured models for the extragalactic magnetic field is shown in Fig. 2.7. It is visible that the benchmark EGMF describes a relatively strong EGMF. Structures like clusters with the highest magnetic flux densities, filaments forming a web-like structure, and voids with the lowest magnetic flux density are clearly visible.

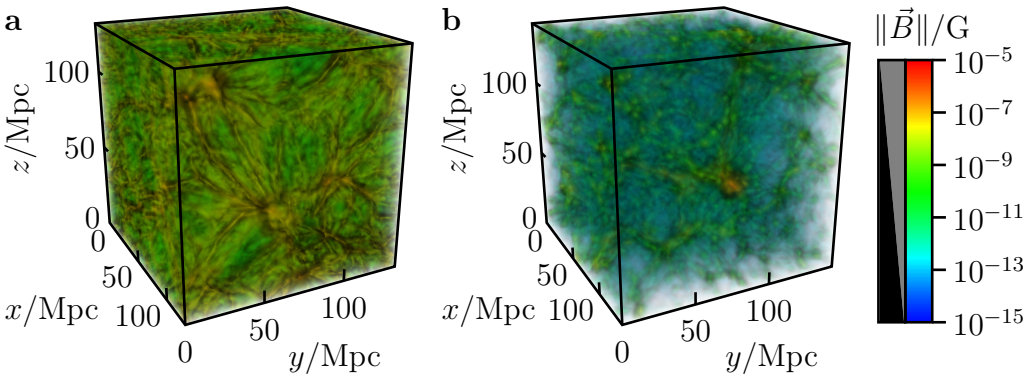

Figure 2.7: Comparison of two famous strongly structured models for the extragalactic magnetic field. The Benchmark EGMF model (left) proposed in [261] is compared with the model of Das et al. [113] (right). Structures like clusters with the highest magnetic flux densities, filaments forming a web-like structure, and voids with the lowest magnetic flux densities are clearly visible.

2.6 Extensive air showers

Today, large ground-based observatories are used to detect UHECRs. A major reason for this is the low flux of cosmic rays at ultra-high energies (see also section 3.1), which requires large detection areas. Since UHECRs interact in the atmosphere of our Earth and lead to *extensive air showers* (EASs) of secondary particles, it is obvious to reveal their existence and properties indirectly by the observation of these EASs and measuring properties of these EASs.

In Fig. 2.8, the longitudinal development of an vertically arriving (zenith angle $\Theta = 0°$) EAS is sketched. After its journey from its source to Earth, a primary UHECR enters the Earth's atmosphere at *atmospheric depth* $X = X_0 = 0\,\mathrm{g\,cm^{-2}}$. At X_1 it firstly interacts with a constituent of the atmosphere, which is often called "air nucleus". This first interaction takes place in the atmosphere of the Earth at a typical height of 15–35 km above sea level (a.s.l.) [264]. It initiates a cascade of secondary particles usually called "extensive air shower" or shortly "air shower". The air shower increases until it reaches its shower maximum at X_{max}. In the following, the air shower is attenuated until it can be detected from the SD stations at atmospheric depth X_2, which is often named X_{ground} or referred to as *vertical column density* or *overburden*. A typical value of X_2 is $880\,\mathrm{g\,cm^{-2}}$ for a vertical air shower hitting the Pierre Auger Observatory, which corresponds to its approximate mean altitude of 1400 m (a.s.l.) [265]. For an observatory at sea level, hit by a vertical air shower, a typical value would be $X_2 \approx 1030\,\mathrm{g\,cm^{-2}}$ [266]. Note that in Fig. 2.8 a vertical air shower that arrives under the zenith angle $\Theta = 0°$ is shown. For geometric reasons, air showers arriving under zenith angle $\Theta > 0°$ (sometimes also called "slant angle") need to penetrate a larger path through the Earth's atmosphere. For inclined air showers with $\Theta > 0°$, X_i is commonly referred to as "slant depth", instead of "atmospheric depth" for $\Theta = 0°$. The curvature of the Earth is often assumed to be negligible for $\Theta \leq 60°$, so that the following approximation can be used:

$$X(\Theta) \approx X(\Theta = 0)\ \sec(\Theta)\,. \tag{2.23}$$

As an example, for the Pierre Auger Observatory and $\Theta = 60°$, X_2 would

increase to approximately $1760\,\mathrm{g\,cm^{-2}}$ [267]. In cases where an error of up to 4% associated with this approximation is acceptable, this approximation can also be used for $\Theta \lesssim 80°$ [268]. If the air shower illustrated in Fig. 2.8 (assuming $X_2 > X_{\max}$) would arrive under a higher zenith angle Θ, less particles of the air shower would be able to reach ground level. For large zenith angles (typically $\Theta > 80°$), the curvature of the Earth is not negligible anymore, so that it needs to be taken into account. For this purpose, the Chapman function can be used [269]. Generally, it is useful to define the slant depth by the integral over the atmospheric density ρ, which the air shower passes on its path $\vec{r}(l)$ through the Earth's atmosphere:

$$X(l) = \int_l^\infty \rho(\vec{r}(l'))\,\mathrm{d}l' \,. \tag{2.24}$$

Here, l is the longitudinal coordinate along the shower axis with the air shower coming from ∞.

For the description of the longitudinal development of an air shower, often a *Gaisser-Hillas function* [271] is used:

$$N_{\mathrm{GH}}(X) = N_{\max}\left(\frac{X - X_1}{X_{\max} - X_1}\right)^{(X_{\max}-X_1)/\Lambda} e^{(X_{\max}-X)/\Lambda} \,. \tag{2.25}$$

Here, $N_{\max}$ is the maximum number of particles at $X_{\max}$. Λ and X_1 are shape parameters. X_1 occasionally lies in the region of the depth of the first interaction, but can also be negative. A Gaisser-Hillas function can also be used to extrapolate measured shower profiles, if a part of the measured shower profile lies outside the field of view of air-shower-observing telescopes. Sometimes a modified Gaisser-Hillas function with a reduced number of parameters is used. It can be gained by equation (2.25) and making use of the substitutions [272] $x = (X - X_1)/\Lambda$ and $x_{\max} = (X_{\max} - X_1)/\Lambda$. This yields the modified Gaisser-Hillas function

$$n_{\mathrm{GH}}(x) = N_{\max}\left(\frac{x}{x_{\max}}\right)^{x_{\max}} e^{x_{\max}-x} \,. \tag{2.26}$$

Sometimes in connection with air-fluorescence detector observations of air showers it seems more advantageous to use a Gaisser-Hillas type function $f_{\mathrm{GH}}(X)$ to describe the energy deposit on slant depth ($\frac{\mathrm{d}E}{\mathrm{d}X}$). Then essentially

in equation (2.25) $N_{\max}$ is exchanged for the maximum energy deposit on slant depth $\left(\frac{\mathrm{d}E}{\mathrm{d}X}\right)_{\max}$, which leads to

$$f_{\mathrm{GH}}(X) = \left(\frac{\mathrm{d}E}{\mathrm{d}X}\right)_{\max} \left(\frac{X - X_1}{X_{\max} - X_1}\right)^{(X_{\max}-X_1)/\Lambda} e^{(X_{\max}-X)/\Lambda} \,. \tag{2.27}$$

Integration of equation (2.27) then gives the calorimetric energy of the air shower, which leads after a correction for the so-called "invisible energy" [273], which is mainly attributable to neutrinos and muons, to the total energy of the air shower and thus the total energy of the primary cosmic ray initiating the air shower [274].

Usually, in the description of an EAS, three components are distinguished. These electromagnetic, hadronic, and muonic components of an EAS are illustrated in Fig. 2.9. The hadronic EAS component dominates only the very early development of the air shower, in which it is directly fed by interactions of the UHECR with the air nucleus. Particles that comprise the hadronic EAS component include baryons, where protons p, neutrons n contribute the major part, and mesons, where charged pions $\pi^{\pm}$, and charged kaons $K^{\pm}$ form the major contribution. The decay of charged pions and charged kaons of the hadronic component feeds the muonic component. Important decays in this context are the main decays of charged pions

$$\pi^+ \to \mu^+ + \nu_\mu \,, \tag{2.28}$$

$$\pi^- \to \mu^- + \bar{\nu}_\mu \tag{2.29}$$

and the main decays of charged kaons

$$K^+ \to \mu^+ + \nu_\mu \,, \tag{2.30}$$

$$K^- \to \mu^- + \bar{\nu}_\mu \,, \tag{2.31}$$

$$K^+ \to \pi^0 + \mu^+ + \nu_\mu \,, \tag{2.32}$$

$$K^- \to \pi^0 + \mu^- + \bar{\nu}_\mu \,. \tag{2.33}$$

Since neutrinos are always produced in these decays (see equations (2.28)–(2.33)), neutrinos are closely connected with the muonic component. Photons from the nearly instantaneous π^0 decay (π^0 mean lifetime [275, 276]: $\tau_{\pi^0} \approx 8 \cdot 10^{-17}\,\mathrm{s}$) in two photons ($\pi^0 \to 2\gamma_{\mathrm{p}}$) are the dominant source of the

electromagnetic EAS component [264]. The main muon ($\mu^{\pm}$) decay

$$\mu^{+} \rightarrow e^{+} + \nu_{e} + \bar{\nu}_{\mu} \tag{2.34}$$

$$\mu^{-} \rightarrow e^{-} + \bar{\nu}_{e} + \nu_{\mu} \tag{2.35}$$

contributes via $e^{\pm}$ also to the electromagnetic EAS component. It should be noted that this decay is particularly relevant for low-energy muons, since high-energy muons, due to relativistic time dilation, are able to cross the Earth's atmosphere and reach the ground without decay.

Taking as an illustrative example a proton with an energy of 10^{19} eV hitting the Earth's atmosphere vertically ($\Theta = 0$), 99% of the about 10^{10} particles of the EAS at sea level are photons (γ_{p}) and electrons (e^{-}) or positrons (e^{+}) of the electromagnetic component of the EAS, transporting 85% of the total energy of the EAS [105]. Muons are transporting in this example only 10% of the total energy of the EAS and the remaining 5% of the total energy of the EAS is split between other particles such as pions and neutrinos [105]. This example clearly shows the importance of the electromagnetic EAS component for EAS development.

Note that there is a connection between the electromagnetic EAS component and the radio emission of an EAS. The radio emission from EASs initiated by UHECRs is described in macroscopic models of the last two decades such as [277, 278] by the geomagnetic mechanism [279] and the charge-excess mechanism [280], whereby the latter is also known as the Askaryan effect [281, 282]. The geomagnetic and charge excess radio emission mechanisms can lead, due to their individual polarization patterns, to an asymmetric radio emission footprint at the position of the radio detectors [283–285].

Today, air shower simulation programs such as CONEX [286] and CORSIKA (COsmic Ray SImulations for KAscade) [287, 288] are available and used for detailed EAS simulations. Average lateral and longitudinal air shower profiles simulated with CORSIKA are shown, e.g., in Fig. 2 of Engel et al. [264]. The air showers shown there are vertical and initiated by 10^{19} eV protons.

A useful method to describe the developmental state of an air shower, is the introduction of the so-called *shower age* $\tilde{s}$ [289, 290]. It is possible to

quantify the shower age $\tilde{s}(X)$ by

$$\tilde{s}(X) = \frac{3}{1 + 2\frac{X_{\max}}{X}} \,. \tag{2.36}$$

Obviously, $\tilde{s}(X) \in [0, 3]$ and $\tilde{s}(X_{\max}) = 1$ apply here. The lateral development of an EAS initiated by an UHECR arriving under zenith angle Θ is sketched in Fig. 2.10. As it is shown in this figure, the SD stations are able to sample the lateral distribution of air shower particles at their positions at ground level. The publications of Nishimura, Kamata, and Greisen made an important contribution to the description of the lateral distribution of air-shower particles [291, 292]. The central function in this context is the Nishimura-Kamata-Greisen (NKG) function

$$\rho_{\mathrm{NKG}}(r) \propto C(\tilde{s}) \left(\frac{r}{r_{\mathrm{M}}} \right)^{\tilde{s}-2} \left(1 + \frac{r}{r_{\mathrm{M}}} \right)^{\tilde{s}-4.5} . \tag{2.37}$$

It describes the particle density at distance r perpendicular to the shower axis. $C(\tilde{s})$ is a normalization factor, r_{M} the Molière radius, and $\tilde{s}$ the shower age.

However, the development of EASs also depends on atmospheric conditions and their variations in time. This is obvious because, for example, an increase/decrease in air pressure can increase/decrease the amount of matter traversed by the air shower particles and thus affect air shower development. Thus, atmospheric conditions are usually monitored at modern observatories that observe EASs [293–295]. An investigation of atmospheric effects on EASs by the Pierre Auger Collaboration can be found in Abraham et al. [296].

For the interpretation of UHECRs, it is sometimes useful to focus on the energy in the center-of-mass frame (CMF). This is reasonable, for example, when an UHECR hits a particle at rest while crossing the Earth's atmosphere or when comparing with reachable CMF energies in particle collider experiments. To address the first example in more detail, the collision of two particles (particle I and particle II) is considered, where the first particle is moving and the second particle is at rest (fixed target). Particle I has mass m_{I}, momentum $\vec{p}_{\mathrm{I}}$, and energy E_{I} and particle II has mass m_{II}, momentum $\vec{p}_{\mathrm{II}}$, and energy E_{II}. Since energy and momentum form a four-vector,

particle I can be described by the four-momentum

$$\boldsymbol{p}_{\mathrm{I}} = \left(\frac{E_{\mathrm{I}}}{c}, \vec{p}_{\mathrm{I}} \right) . \tag{2.38}$$

The four-momentum of particle II in the laboratory frame (LF) is

$$\boldsymbol{p}_{\mathrm{II}} = \left(m_{\mathrm{II}} c, \vec{0} \right) . \tag{2.39}$$

Addition of equation (2.38) and (2.39) leads to the total four-momentum of the two-particle system

$$\boldsymbol{p} = \boldsymbol{p}_{\mathrm{I}} + \boldsymbol{p}_{\mathrm{II}} = \left(\frac{E_{\mathrm{I}}}{c} + m_{\mathrm{II}} c, \vec{p}_{\mathrm{I}} \right) . \tag{2.40}$$

Using the Einstein summation convention, the LF and the CMF (denoted by a prime ') are related by

$$\boldsymbol{p}^{\mu} \boldsymbol{p}_{\mu} = \boldsymbol{p}'^{\mu} \boldsymbol{p}'_{\mu} . \tag{2.41}$$

Since $\boldsymbol{p}'^{\mu} \boldsymbol{p}'_{\mu} = -E'^2 c^{-2}$ in the CMF, it follows for the center-of-mass energy E' of the two-particle system the result

$$\begin{aligned} E' &= \sqrt{(m_{\mathrm{I}}^2 + m_{\mathrm{II}}^2) c^4 + 2 E_{\mathrm{I}} m_{\mathrm{II}} c^2} \\ &\approx \sqrt{2 E_{\mathrm{I}} m_{\mathrm{II}} c^2} . \end{aligned} \tag{2.42}$$

The last approximation is possible in the ultra-relativistic limit that is with $E_{\mathrm{I}} \gg m_{\mathrm{I}} c^2$ always given for UHECRs.

For two particles flying towards each other with the same energy E_{I} and colliding, an analogous calculation yields $E' = 2E_{\mathrm{I}}$. Such a configuration is typically not encountered in UHECR collisions, but present in modern particle colliders.

The Large Hadron Collider (LHC) [297, 298] is currently the world's highest-energy particle collider [299]. Assuming, e.g., that a UHECR is a proton with $E_{\mathrm{I}} = 10\,\mathrm{EeV}$ that collides with a resting proton with rest mass $m_p \approx 938.27\,\mathrm{MeV/c^2}$ in the Earth's atmosphere, equation (2.42) yields a center-of-mass energy $E' \approx 137\,\mathrm{TeV}$. It greatly exceeds the center-of-mass energy in proton-proton collisions of 13 TeV [300], that was reached at the

LHC. This is one of the reasons why UHECRs are a highly interesting and important subject of research. Moreover, this is an uncertainty in the simulation of EASs, since hadronic interactions, especially for modeling the first interaction between the UHECR and the air nucleus, must be extrapolated to center-of-mass energies that are not reached by current man-made accelerators.

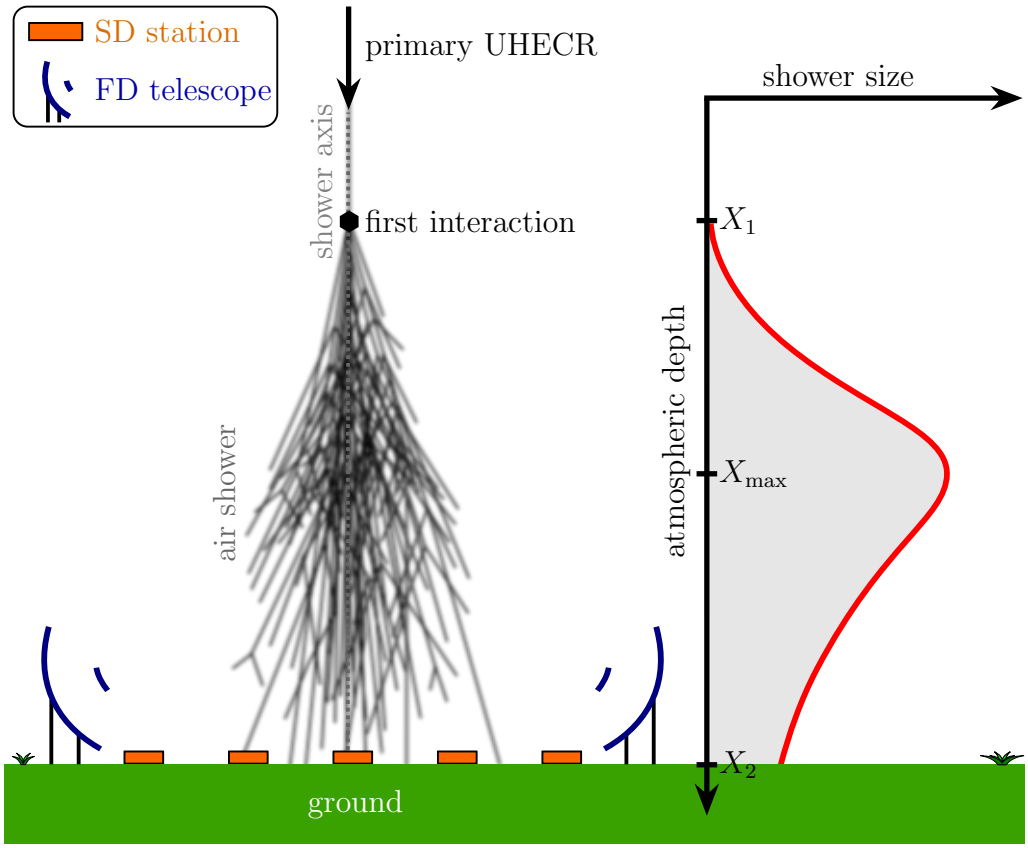

Figure 2.8: Sketch showing the longitudinal development of an EAS. A primary UHECR enters the Earth's atmosphere at atmospheric depth $X_0 = 0\,\mathrm{g\,cm^{-2}}$. At X_1 it firstly interacts with an constituent of the atmosphere. The air shower increases until it reaches its shower maximum at $X_{\max}$. In the following the air shower is attenuated until it can be detected from the SD stations at slant depth X_2, which is often also named X_{ground}. Under good atmospheric conditions with low light pollution, which can be expected on clear moonless nights, FD telescopes are able to observe this longitudinal development of an EAS.

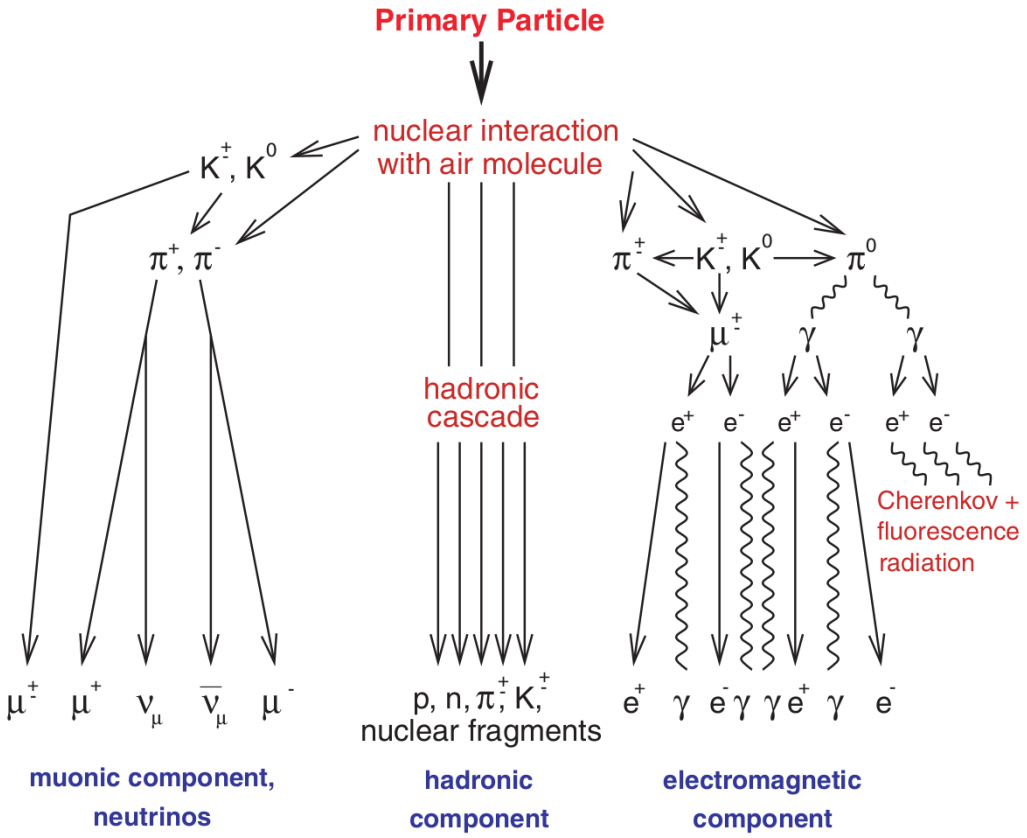

Figure 2.9: Schematic illustration showing the electromagnetic, hadronic, and muonic components of an EAS initiated by a primary particle. Figure: from Fig. 2 in [270].

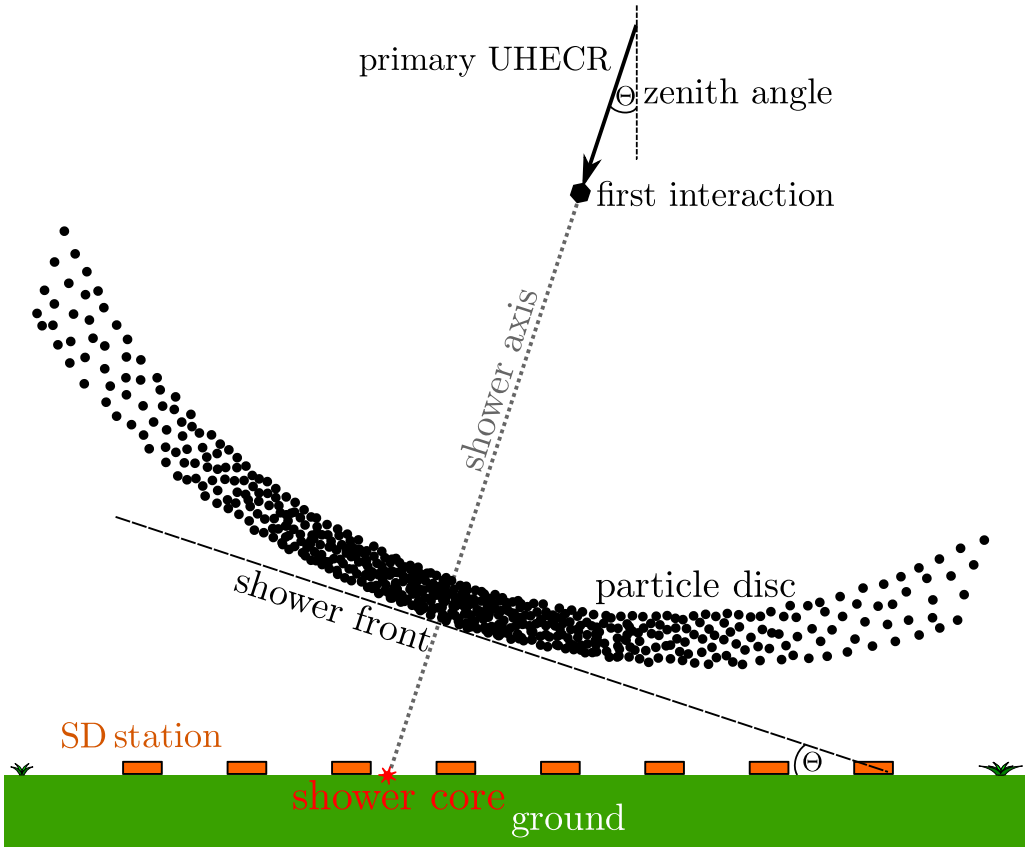

Figure 2.10: Sketch showing the lateral development of an EAS initiated of an primary UHECR arriving under zenith angle Θ. After the first interaction of the primary UHECR with an air nucleus a cascade of secondary particles is initiated and leads to an curved EAS's front with a typical thickness of a few meters in the center. Its thickness increases with a larger distance from the shower axis. The SD stations are able to sample the lateral distribution of air shower particles at their positions at ground.

2.7 Detectors

Since the discovery of cosmic radiation more than a century ago, many different detectors and observatories have been constructed for its detection. Today, the two largest observatories for the detection of UHECRs are the Pierre Auger Observatory (see section 2.7.1) and the Telescope Array (see section 2.7.2). For the long and successful operation of optical detection methods, such as air fluorescence telescopes that are used by these observatories, excellent meteorological conditions are necessary. This had a great influence on the choice of a location for the respective experiments. Important factors are clear cloudless skies, low precipitation, low light pollution (i.e., artificial light), and a low amount of dust and aerosols in the atmosphere. Besides large-scale UHECR observatories, there are also large-scale neutrino observatories (see section 2.7.3), which provide upper limits for the flux of cosmogenic neutrinos that are produced during the propagation of UHECRs. The locations of important large-scale UHECR and neutrino observatories are shown in Fig. 2.11.

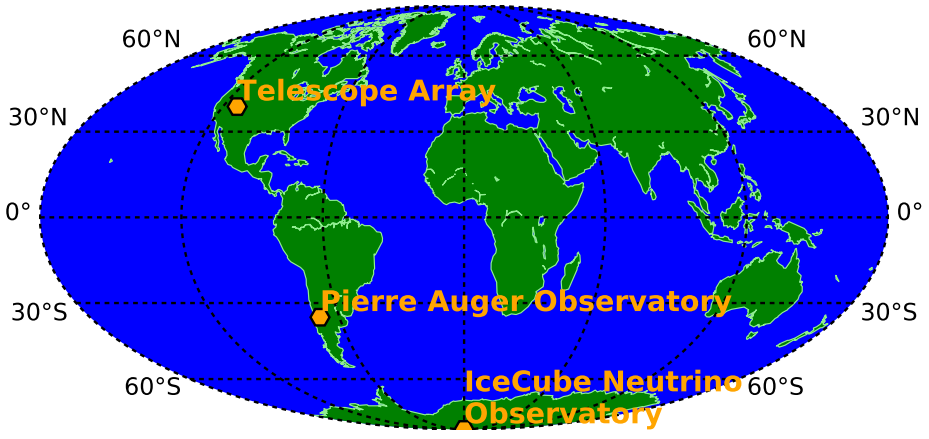

Figure 2.11: The locations of the large-scale UHECR observatories Telescope Array (in the northern hemisphere) and Pierre Auger Observatory (in the southern hemisphere) as well as the location of the large-scale IceCube Neutrino Observatory (in the southern hemisphere). In the background, a world map in Mollweide projection is shown.

2.7.1 Pierre Auger Observatory

The Pierre Auger Observatory is currently the worldwide largest cosmic ray observatory [301, 302]. It is located in Argentina near the city of Malargüe (approximately at latitude 35° S and longitude 69° W) [303]. Its mean altitude is about 1400 m a.s.l. and the detectors are installed at altitudes between 1340 m and 1610 m [88]. Consisting of a surface detector (SD) and a fluorescence detector (FD), which are two well-established independent detector systems, the Pierre Auger Observatory follows a hybrid concept [304].

2.7.1.1 Surface detector

The basic SD consists of an array of 1660 water-Cherenkov particle detector stations that are arranged on a triangular grid of 1.5 km spacing and cover an area of about 3000 km^2 [85]. In a 23.5 km^2 large part of the array, 61 SD stations are arranged more densely with 750 m spacing and in a 1.9 km^2 large part of the array, 19 SD stations are arranged with a spacing of only 433 m. The SD stations are cylindrical with diameter 3.6 m and often called "SD tank" or concisely "tank". Each SD station contains a sealed liner that is filled with 12 m^3 of ultra-pure water [85] to prevent the growth of microorganisms that would impair the optical properties and thus a stable long-term operation. The liner has a diffusively reflective inner surface and at its top three polyethylene windows that allow Cherenkov light produced in the water volume to pass. Cherenkov light is emitted when a charged particle like a muon μ^- or electron e^- moves with a velocity v through the water that is larger than the phase velocity c/n of light in the water, where n is the refractive index of the water.[1] For the detection of this Cherenkov light, a photomultiplier tube (PMT) with a diameter of 9 inch is located behind each window. The three PMTs are arranged symmetrically in the upper part of each tank with a radial distance of 1.2 m from the tank's center axis.

Further parts of a typical SD station are shown in Fig. 2.12. Note that the

[1] Assuming a refractive index of $n = 1.33$ for the water, which is used as medium, for a muon with rest mass $m_\mu = 105.66\,\mathrm{MeV/c^2}$ the minimum (threshold) kinetic energy $E_{\mathrm{Ch,min}}$ that is necessary for the emission of Cherenkov radiation can be estimated as $E_{\mathrm{Ch,min}} = m_\mu c^2((1 - 1/n^2)^{-1/2} - 1) \approx 55\,\mathrm{MeV}$. For an electron with rest mass $m_e = 0.51\,\mathrm{MeV/c^2}$ the same estimation leads to $E_{\mathrm{Ch,min}} \approx 0.3\,\mathrm{MeV}$.

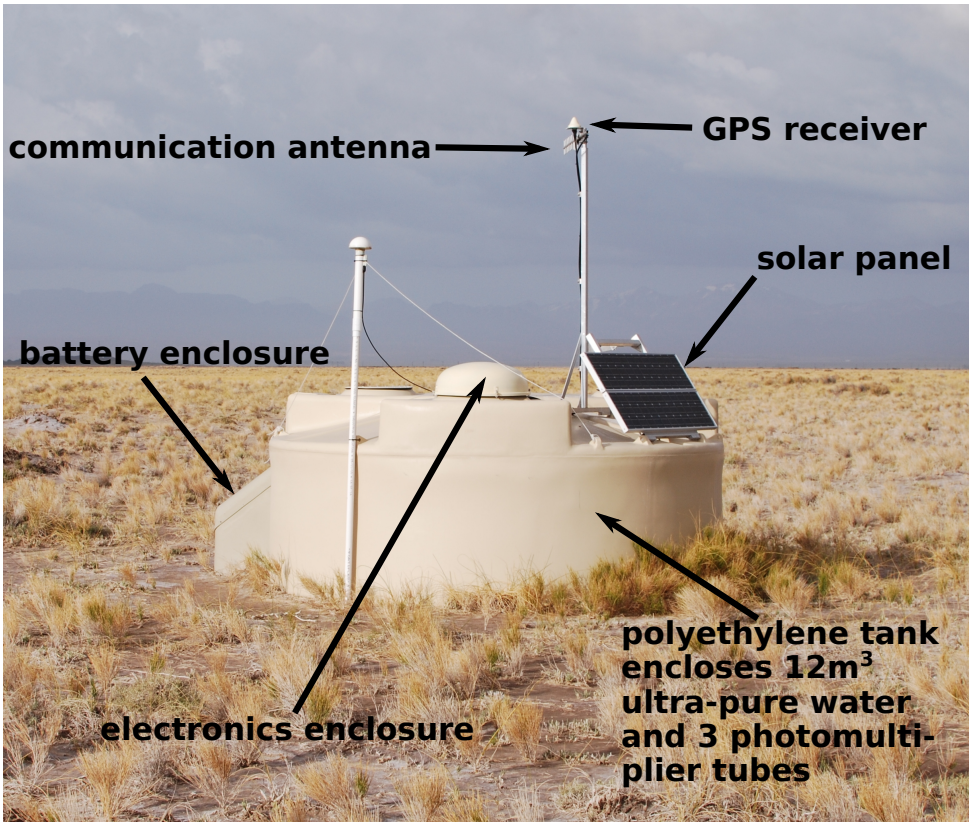

Figure 2.12: Surface detector (SD) station deployed in the SD field of the Pierre Auger Observatory. Important components visible from the outside are labeled. Adapted with permission from a photo by Sven Querchfeld.

additional antenna shown in Fig. 2.12 was part of the EASIER (Extensive Air Shower Identification with Electron Radiometer) project [305–307] and therefore is not a SD part that is prevalent in SD tanks. An important feature of the SD is its continuous operation and nearly 100% duty cycle.

2.7.1.2 Fluorescence detector

The FD of the Pierre Auger Observatory consists of 4 FD sites. They are placed at the boundary of the observatory. The FD site in the northern part of the observatory is called Loma Amarilla, the site in the eastern part is known as Los Morados, the one in the southern part as Los Leones, and the one in the western part as Coihueco. Each of the FD sites houses six independent air fluorescence telescopes that are also called "FD telescopes". The field of view of each telescope is 30° in azimuth and 1.5°-30° in elevation

above the horizon [87]. Thus, the six fluorescence telescopes located in one building cover together a field of view of 180° in azimuth. The air fluorescence telescopes overlook the SD and observe the atmosphere above the SD. They are able to observe the longitudinal development of an air shower, which is also sketched in Fig. 2.8 on page 43.

These telescopes observe the fluorescence light emitted by nitrogen molecules in the air, which have been excited by the passage of air shower particles. An important part of an FD telescope is a segmented mirror that focuses the faint fluorescence light on a camera [308]. The camera has 440 pixels that are arranged in 20 columns and 22 rows. In contrast to Cherenkov light that is emitted anisotropically in a Cherenkov cone around the direction of motion of air shower particles [99], the fluorescence light is emitted isotropically and thus it allows observations of air showers from relatively large distances. The limitation of FD measurements to dark and moonless nights results in a duty cycle of about 15%.

The basic FD described here and the basic SD described in the previous section 2.7.1.1 are supplemented by various enhancements and extensions that are described in section 2.7.1.3 and by the ongoing upgrade of the Pierre Auger Observatory that is shortly described in section 2.7.1.4.

2.7.1.3 Enhancements and extensions

There are multiple enhancements and extensions of the Pierre Auger Observatory. The Auger Engineering Radio Array (AERA) is the radio extension of the Pierre Auger Observatory [309]. It is able to detect cosmic rays by the radio emissions of extensive air showers [310]. AERA is a large array of radio antenna stations consisting of more than 150 autonomous radio stations that are spread over an area of about $17\,\mathrm{km}^2$. The radio antenna stations of AERA are sensitive to the radio emissions from the electromagnetic component of extensive air showers caused by UHECRs in the 30 - 80 MHz frequency band [310].

An other enhancement are the three “High Elevation Auger Telescopes” (HEAT) located near the Coihueco FD site. Each HEAT FD telescope is housed in an individual building. In comparison to the Pierre Auger Observatory FD telescopes, the HEAT telescopes have the ability to tilt them upwards by 29° with a hydraulic system and thus allow to observe

air showers developing much higher in the atmosphere. Usually HEAT telescopes are operated in tilted orientation for data acquisition. This mode is also called "upward mode". In the "downward mode", i.e. in horizontal orientation, the HEAT telescopes are usually used for service purposes or cross-calibration with, e.g., the FD telescopes [85]. By combination of data from Coihueco FD telescopes and HEAT telescopes an extended field of view above the horizon up to nearly 60° in elevation is possible, which allows to better observe the crucial region around the shower maximum for air showers initiated by lower energy cosmic rays, that would not be observable without the HEAT enhancement by the Pierre Auger Observatory. The HEAT telescopes are thus a low-energy extension of the FD of the Pierre Auger Observatory.

The low-energy extension of the surface detector of the Pierre Auger Observatory is called "Auger Muon and Infill for the Ground Array" (AMIGA) [311]. Close to HEAT and overlooked by its telescopes an "Infill array" of 23.5 km^2 size with additional surface detector stations and smaller spacing is installed. Additionally, AMIGA consists of a few muon detectors, which are scintillator counters buried under soil near the Infill stations. The SD stations, which are used in the Infill array, do not differ from the other SD stations and thus are not seldom added to the total number of SDs.

2.7.1.4 Ongoing upgrade

While these lines are being written, a major upgrade of the Pierre Auger Observatory under the name "AugerPrime" is in progress. A preliminary design report of the planned upgrade of the Pierre Auger Observatory from 2015 can be found in [312]. More recent descriptions of AugerPrime are given in Refs. [313, 314]. The main aim of this upgrade of the Pierre Auger Observatory is to increase its detection capabilities for UHECRs. This includes an improved measurement of the mass composition of UHECRs.

An important part of the upgrade will be the installation of a new detector on top of each existing SD station. The new detector is a *surface scintillator detector* (SSD), which is based on two plastic scintillator planes in a SSD box and will thus provide a complementary measurement of the air shower particles reaching the detector. The combination of these two detector types (surface scintillator detector and water-Cherenkov detector)

is important since they have different responses to the muonic and electromagnetic components of an air shower and thus improve the ability to reconstruct the mass composition of UHECRs. Each SSD box has a length of about 3.8 m and a width of about 1.3 m. The two in the SSD box contained scintillator modules of roughly 1 cm thickness will each have an area of 1.9 m^2 [315].

A further part of the upgrade consists of the addition of a fourth small (1″ diameter) PMT in the SD tanks to increase the dynamic range and new enhanced SD electronics which allow to read and process the data of the four PMTs and the SSD.

Also, an important part of the upgrade is to increase the duty cycle of the fluorescence detector by enabling measurements in periods of higher night sky background.

In addition, it is worth noting that a underground muon detector (UMD) will be buried under a several-meter layer of soil next to each of the SD stations in the Infill array. The UMD is shielded from the electromagnetic component of the air showers by the several-meter layer of soil under which it is buried, so the UMDs should provide a good measurement of the muon component of air showers and its time structure.

After good experience with AERA, a radio antenna will be installed on each SD station as part of the upgrade. In this way a impressively large radio detector (RD) with a size of 3000 km^2 will be formed, making it the world's largest radio array for the detection of UHECRs [316]. The aim of this RD is to detect the radio emission of air showers. The frequency range from 30 MHz to 80 MHz is important here [316, 317]. Considering the 1.5 km spacing of the radio antennas of the RD and the fact that the footprint of the radio emission on the ground increases with increasing zenith angle of the air shower, the RD is expected to provide good detection for zenith angles of the air shower greater than 60°. The duty cycle of the RD is expected to be similar to that of the SD since, unlike the FD, there are no restrictions on nights for operation.

With these improvements, many new and amazing findings can be expected in the coming years.

2.7.2 Telescope Array

The Telescope Array (TA) is located in the USA near Delta (Utah) at approximate latitude 39° N and longitude 113° W [318]. Its altitude is about 1400 m a.s.l.. It is collecting data since 2008 [319]. As the Pierre Auger Observatory (see previous section 2.7.1), also the Telescope Array consists of a SD and FD and follows a hybrid concept, but the detectors of both observatories differ. The TA uses scintillation detectors for the SD whereas the Pierre Auger Observatory uses water-Cherenkov[2] detectors.

2.7.2.1 Surface detector

The TA surface detector is described in detail in [84]. It consists of an array of 507 SD stations, that cover an area of about 700 km^2 and are arranged on a square grid with 1.2 km spacing. A typical TA SD station is shown in Fig. 2.13. It consists of an antenna for data transfer, a solar panel and battery dealing as power supply for the SD station, an electronics box, a Global Positioning System (GPS) receiver and a rectangular box, that includes the two-layered 3 m^2 plastic scintillator. During operation so far, the duty cycle of the TA surface detector was approximately 95% on average [320].

2.7.2.2 Fluorescence detector

The FD consists of 3 FD sites Black Rock Mesa (BR), Long Ridge (LR), and Middle Drum (MD). The BR and LR sites include 12 telescopes. The MD site includes 14 fluorescence telescopes. Since at the MD site old mirrors of the HiRes experiment are used [321], there is a deviation in the number of mirrors compared to the BR and LR sites. The BR site is shown in Fig. 2.15 (a) with a few solar panels in front and communication antennas on top of a building housing the FD telescopes. On the back side of the BR building, which cannot be seen by the reader in this figure, there are multiple openings in the building shell through which the FD telescopes can observe the sky at night (see Fig. 2.14 (a)). At day these openings need to be closed to protect the mirrors from soiling by, e.g., dust blown up by strong winds (see Fig. 2.14 (b)). Nevertheless, a regular cleaning of the

[2]SSDs as part of the ongoing upgrade of the Pierre Auger Observatory are not meant here and mentioned in chapter 2.7.1.4.

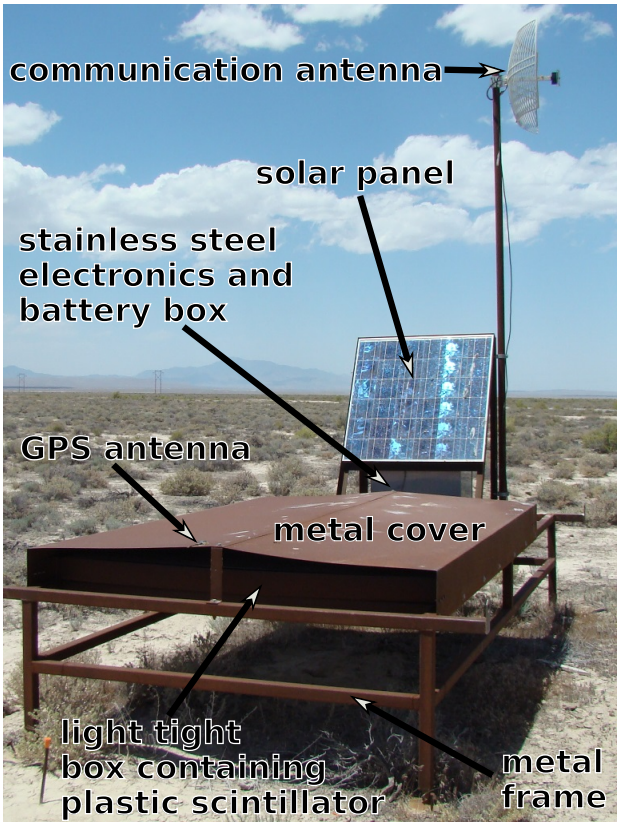

Figure 2.13: Telescope array surface detector (SD) station deployed in the SD field. Important components visible from the outside are labeled. The rectangular light tight box contains a two-layered $3\,\mathrm{m}^2$ plastic scintillator.

mirrors from the FD telescopes is necessary.

The BR building houses, inter alia, 6 lower and 6 upper telescopes, that view 17°–30° and 3°–17° in elevation above the horizon.

Each telescope consists of a primary mirror and a camera. The primary mirror of the fluorescence telescopes in the BR and LR sites consists of 18 mirror segments and can be seen in Figs. 2.15 (b), (c) and in a detailed view in (e). The camera of the BR and LR sites consists of 256 photomultiplier tubes (PMTs) in a camera box which deal as camera pixels. The camera box in the front of each mirror is covered by an UV band pass filter and can be seen in Fig. 2.15 (d). Of course there is also an electronics room for processing the data from the FD telescopes (see Fig. 2.15 (f)).

Similar to the fluorescence detector of the Pierre Auger Observatory, the duty cycle of the fluorescence detector of the Telescope Array is much

smaller than that of its surface detector. This is because for the fluorescence detectors of both, data collection is limited to nights that are clear and moonless only. During operation so far, the duty cycle of the TA fluorescence detector was approximately 10% [320].

(a) **(b)**

Figure 2.14: (a) Not completely closed openings in the FD building shell of the BR site through which the FD telescopes can observe the sky at night. The cables visible in the left part of the figure come from cameras of several FD telescopes. (b) Dust blown up by strong winds, observed from BR site during daylight.

2.7.2.3 Enhancements and extensions

An important extension of the Telescope Array is the "Telescope Array Low-energy Extension" (TALE) [322–324]. Aim of this extension is to increase the energy range in which the energy spectrum and chemical composition of cosmic rays can be observed to lower energies. It allows observing air showers induced by primary cosmic rays down to energies of $10^{16.5}$ eV ($3{\cdot}10^{16}$ eV). TALE is a hybrid detector consisting of a TALE SD and a TALE FD. The TALE FD station consists of 10 FD telescopes. Both the TALE FD station and the TALE SD stations are located near the TA Middle Drum (MD) station. By combination of data from the 14 Middle Drum TA FD telescopes and the 10 TALE FD telescopes an extended field of view above the horizon from 3° up to 59° in elevation is possible [323], which is important for the observation of low-energy cosmic rays. The TALE FD telescopes were completed in 2013. For the construction of the TALE FD telescopes,

refurbished parts of the HiRes experiment were used. Additionally, TALE SD stations with smaller spacing (of 600 m and 400 m [324]) than the TA SD stations were installed. Another low energy extension of the TA is called "Non-Imaging CHErenkov Array" (NICHE). It is located next to the TALE FD [325]. NICHE, as a low energy extension of the Telescope Array experiment, aims to measure cosmic rays and their composition in the energy range from about 10^{16} eV to 10^{18} eV. This is an energy range in which a change in composition from a galactic component to an extragalactic component is expected. For this purpose it uses detectors that are located at a small distance (of about 100 m) from each other. A prototype array of NICHE, with the name "j-NICHE", could already be deployed in 2017 [326]. NICHE was completely deployed in 2018. Further details on NICHE can be found in [326].

2.7.2.4 Ongoing extension

Currently an extension of the TA experiment, with the name "TA×4" experiment, is ongoing. Status and prospects of the TA×4 experiment are described in [327]. Recent details on the surface detector of the TA×4 experiment including information about the design and the expected performance can be found in [320].

The TA×4 SD stations are deployed in the northeast of the TA SD array near the TA Middle Drum FD station and in the southeast of the TA SD array near the TA Black Rock Mesa FD station. The previous conference proceeding [328] shows the planned locations and the size of the TA×4 detector in detail.

The spacing of the TA×4 SD stations is 2.08 km and thus greater than the 1.2 km spacing of the TA SD stations [328]. A larger distance between the TA×4 SD stations compared to the distance between the TA SD stations was chosen as a compromise to ensure a large detection area while saving money for less required new TA×4 SD stations. This is possible since the TA×4 is designed to study UHECRs with energies especially above 57 EeV and thus a higher spacing is possible to reduce costs and gain a larger detection area. If the TA×4 developers were interested in the detection of much lower UHECR energies, a much finer array of SD stations would have been chosen, since the size of the air showers and their footprint at SD

level decreases with decreasing energy of the air shower initiating primary UHECRs. The vice versa applies to increasing energy of air shower initiating primary UHECRs.

The higher spacing between the TA×4 SD stations causes a reduced angular resolution of about 2.2° in comparison to the 1° angular resolution of the TA SD [328]. The 500 TA×4 SD stations shall cover an roughly 3 times larger area than the 507 TA SD stations. Thus the TA×4 SD stations shall cover together with the TA SD stations an area of roughly 3000 km^2. This fact is also reflected in the name TA×4. Note, that the area is similar to the area covered by the SD of the Pierre Auger Observatory.

There are only small differences between the TA×4 SD stations and the TA SD stations. Their basic design (consisting of two-layered 3 m^2 plastic scintillators which scintillation light is read out using wave length shift fibers, photomultiplier tubes and readout electronics) does not differ. Among the differences is the use of better photomultiplier tubes for the TA×4 SDs with a higher quantum efficiency compared to the TA SDs. One of the minor differences is that each TA×4 SD station has bird spikes attached on top of the support frame of the solar panel [320]. The support frame of the solar panel can be seen in Fig. 2.13. However, since there is not a TA×4 SD station shown, the bird spikes are missing.

The scintillator boxes for the TA×4 SD stations were assembled in Japan since 2015. Three years later (2018) also in South Korea scintillator boxes for the TA×4 SDs were assembled. The TA×4 extension shall feature two FD stations, using telescopes of the HiRes experiment. These TA×4 FD stations, consisting of a north and a south FD station, overlook the TA×4 SD. The northern TA×4 FD station (that observed first light in 2018) houses 4 telescopes of the HiRes experiment, the latter 8 telescopes.

The fully assembled SD detectors are usually stored in a fenced area near the so-called “Lon and Mary Watson Millard County Cosmic Ray Center” (see Fig. 2.16) before they are transported to their final location in the detector field. A helicopter is usually used to transport the individual SD stations to their final position.

2.7.3 Large-scale neutrino detectors

The Pierre Auger Observatory offers the capability to detect ultra-high energy neutrinos (UHEνs)[329]. An experimental challenge in this context is to distinguish air showers initiated by UHEνs from the huge background of air showers initiated, e.g., by ultra-high energy protons or heavier nuclei impinging on the Earths atmosphere. One way to meet this experimental challenge for neutrinos with energies $\geq 10^{17}$eV, suggested many decades ago [330], is to observe EASs arriving at a large zenith angle. The underlying idea is that neutrinos, due to their small cross-sections, can produce air showers that are initiated much deeper in the atmosphere than, for example, air showers from ultra-high energy protons or heavier nuclei. Details on the identification of UHEνs in the data from the Pierre Auger Observatory in consideration of neutrinos that interact in the atmosphere and neutrinos that interact in the Earth's crust (usually called Earth-skimming neutrinos), can be found in [329].

An famous large-scale observatory for the detection of neutrinos is the IceCube neutrino observatory (sometimes also briefly referred to as IceCube), which is in detail described in [331]. The IceCube neutrino observatory is located at the geographic South Pole as shown in Fig. 2.11. It consists basically of a detector measuring Cherenkov photons from charged particles traversing the ice. The basic IceCube in-ice array has a volume of about one cubic kilometer in the Antarctic ice. The *digital optical module* (DOM) is the basic detection unit used in IceCube [332]. The basic IceCube in-ice array consists of 86 hexagonally arranged strings, with which the DOMs are connected at depths between 1450 m and 2450 m. There are 60 DOMs connected to each of these strings. The vertical distance between each DOM is about 17 m and the horizontal distance between the strings is about 125 m.

Other parts of the IceCube neutrino observatory are the more densely instrumented "DeepCore" sub-array, which is located inside the basic IceCube in-ice array and the detector "IceTop" [333], which is located on the surface of the ice at an altitude of 2835 m a.s.l..

The design, which includes both the size of the detector and the spacing between the DOMs, was configured to detect neutrinos in the energy range of approximately TeV to PeV, which was successful [334]. Nevertheless, the IceCube neutrino observatory can also provide upper limits for neutrinos

with higher energies, which are of particular interest.

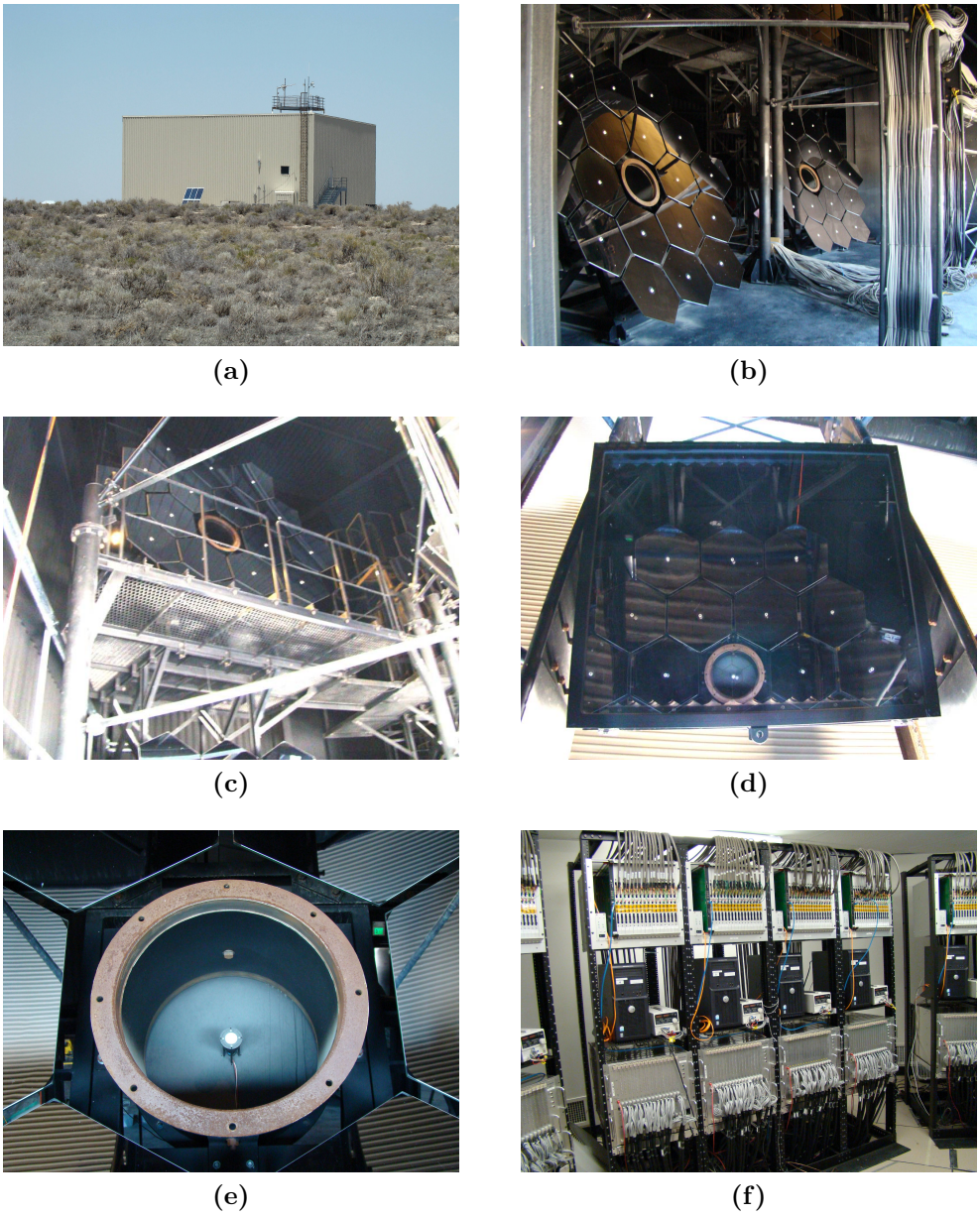

Figure 2.15: Parts of the Telescope Array Black Rock Mesa (BR) fluorescence detector (FD) site. Fluorescence detector building (a) that houses 6 lower and 6 upper telescopes viewing 17°-30° and 3°-17° in elevation above the horizon, two mirrors (b) of the lower BR FD telescopes. Each one of this BR FD mirrors has a diameter of about 3 m and is subdivided into 18 hexagonal segments. Two mirrors of the upper BR FD telescopes (c), camera box covered by an UV band pass filter in the front of each mirror consisting of a array of 256 (16×16) photomultiplier tubes (PMTs) which deal as camera pixels (d), light source for calibration purposes (e), and electronics room (f).

(a) **(b)**

Figure 2.16: (a) Lon and Mary Watson Millard County Cosmic Ray Center in Delta, Utah, (b) fully assembled TA SDs stored in a fenced area next to the Cosmic Ray Center until their deployment in the detector field.

3 Analysis of UHECR observations

3.1 Energy spectrum

The flux of cosmic rays depends strongly on energy. Therefore, many experiments and observatories were in the past and are still today concerned with the precise measuring of the cosmic ray "differential energy spectrum" $J(E)$, that is observable at the Earth:

$$J(E) = \frac{\mathrm{d}^4 N}{\mathrm{d}A\,\mathrm{d}t\,\mathrm{d}\Omega\,\mathrm{d}E}(E)\,. \tag{3.1}$$

In the literature, it is also referred to as "energy spectrum". This short term will be used in the following. The energy spectrum quantifies the number of particles $\mathrm{d}N(E)$, per unit area $\mathrm{d}A$, unit time $\mathrm{d}t$, unit solid angle $\mathrm{d}\Omega$, and unit energy interval $\mathrm{d}E$ [335]. Often, the energy spectrum is given in units of $\mathrm{m}^{-2}\,\mathrm{s}^{-1}\,\mathrm{sr}^{-1}\,\mathrm{eV}^{-1}$. Sometimes, the *integral energy spectrum*

$$J_{\mathrm{I}}(E \geq \tilde{E}) = \int_{\tilde{E}}^{\infty} J(E)\,\mathrm{d}E \tag{3.2}$$

is used, which can be calculated by integration of the differential energy spectrum.

The all-particle cosmic ray energy spectrum measured by various experiments and observatories at the Earth is visualized in Fig. 3.1. In Fig. 3.1 (a) measurements with particle energies above $10^{11}\,\mathrm{eV}$ and in Fig. 3.1 (b) data with particle energies above $10^{15}\,\mathrm{eV}$ up to beyond $10^{20}\,\mathrm{eV}$ are shown. Usually, the cosmic ray energy spectrum is defined to range from about $10^{9}\,\mathrm{eV}$ to beyond $10^{20}\,\mathrm{eV}$ [336]. At energies less than about $10^{9}\,\mathrm{eV}$, cosmic rays and thus their energy spectrum are considerably affected by the *solar*

modulation [337, 338].

Above an energy of about 10^{14} eV, the flux of cosmic rays is so small that direct measurements of primary cosmic rays by balloon- or satellite-borne cosmic ray detectors is extremely impractical and futile. Therefore, indirect detection of cosmic rays via extensive air showers (see Section 2.6) needs to be used for higher energies.

In Fig. 3.1 (a), the energy spectrum appears quite structureless. The nearly linear course of the data in this double logarithmic representation suggests that the energy spectrum observed at the Earth can be roughly described by a power law $E^{-\gamma}$ with spectral index γ. Such a power-law spectrum, which spans many orders of magnitude in energy, suggests a non thermal origin of cosmic rays. Characteristic features in the shape of the energy spectrum are typically named according to their resemblance with a human leg: "knee", "second knee", and "ankle". For an additional feature, the so-called "instep" at approximately $1.4 \cdot 10^{19}$ eV, the interested reader is referred to [339, 340].

While it is believed that UHECRs with energies above the "ankle" have a predominantly extragalactic origin, one believes that for lower energies a non-negligible contribution of particles with a galactic origin cannot be excluded [119, 341, 342]. At the highest observed energies, there is a strong flux suppression - the so called "cutoff". For the sake of clarity, data from spectrum measurements of a selection of exemplary experiments and observatories are shown.

Note that it is important to distinguish between the energy spectrum observed at the Earth which is shown in Fig. 3.1, and the energy spectrum emitted at the sources of cosmic rays, since interactions during the cosmic-ray propagation can lead to differences between both energy spectra.

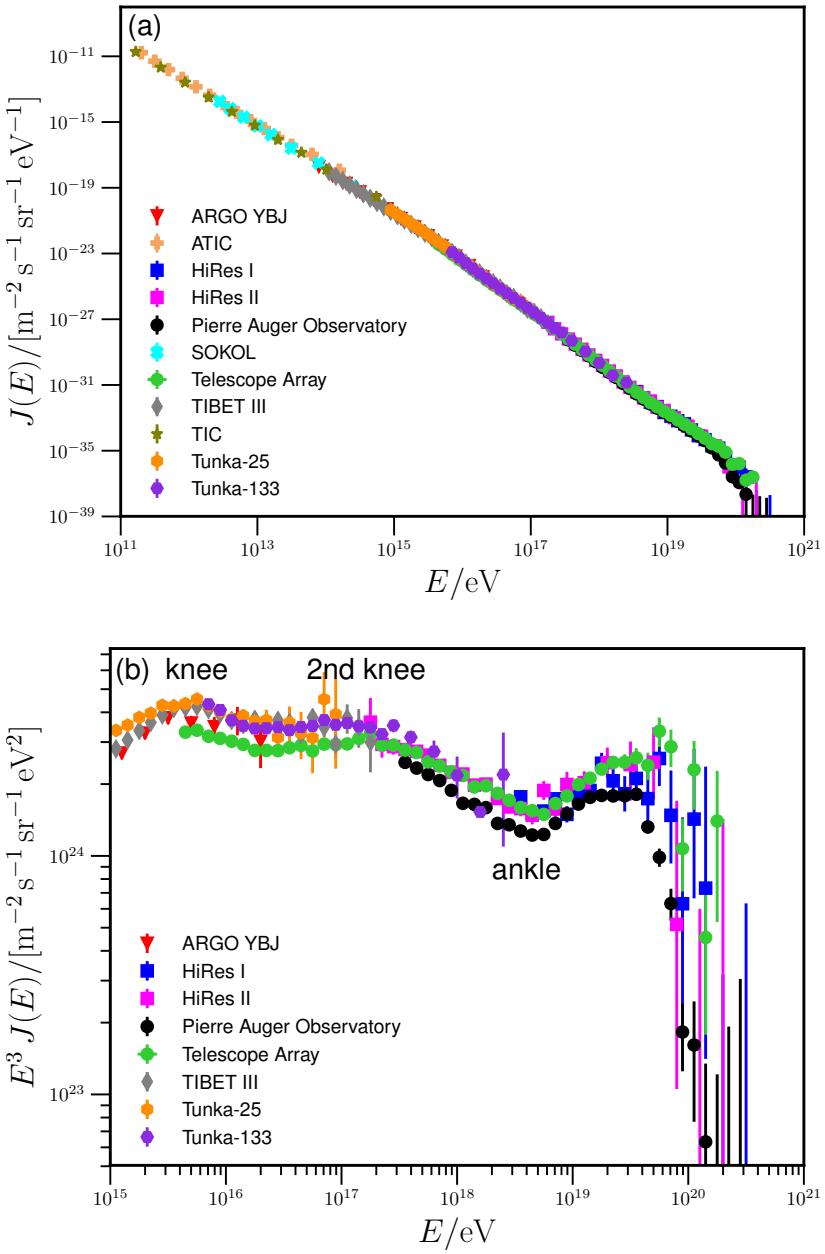

Figure 3.1: All-particle cosmic ray energy spectrum measured by various experiments and observatories above (a) $10^{11}\,\mathrm{eV}$ and (b) $10^{15}\,\mathrm{eV}$. In the latter case, the values are rescaled by a factor E^3 to make features like the "ankle" clearly visible. Results of the experiments ARGO-YBJ ("all particle") [343], ATIC [344], HiRes I and HiRes II [345], Pierre Auger Observatory [346], SOKOL [347], Telescope Array ("TA combined (ICRC 2015)") [348], TIBET III ("QGSJET+HD") [349], TIC [350], Tunka-25 [351], and Tunka-133 [352] are shown.

3.2 Composition

As mentioned in section 3.1, direct measurements of primary cosmic rays by balloon- or satellite-borne cosmic ray detectors are restricted to particle energies $E \lesssim 10^{14}\,\mathrm{eV}$. For higher energies ($E \gtrsim 10^{14}\,\mathrm{eV}$) indirect detection of cosmic rays via EAS is common. An important article with the focus on the interesting energy range above $10^{15}\,\mathrm{eV}$ that reviews how data of EASs are related to the mass composition of cosmic rays is Kampert and Unger [112]. A reliable indicator of the composition of the primary particle is the depth of the shower maximum X_{max}. There is a consensus that X_{max} depends on the mass of the primary UHECR. Although most of the information is contained in the complete X_{max} distribution, many publications focus only on the first two moments $\langle X_{\mathrm{max}} \rangle$ and $\sigma(X_{\mathrm{max}})$, which are very informative for the composition of UHECRs and thus very important for comparison with other experiments. Note that, unlike $\langle X_{\mathrm{max}} \rangle$ and $\sigma(X_{\mathrm{max}})$, the X_{max} distribution is usually not adjusted for detector effects. The X_{max} distribution in various energy intervals as measured by the Pierre Auger Observatory is visualized in Fig. 3.2. As expected, with increasing energy the number of detected UHECR events decreases. In Fig. 3.3, measurements of $\langle X_{\mathrm{max}} \rangle$ by various experiments and observatories are shown as a function of the logarithm of the particle energy E. Assuming the same particle energy, air showers initiated by heavy nuclei such as iron nuclei have a smaller $\langle X_{\mathrm{max}} \rangle$ than air showers initiated by light nuclei such as protons, as can be seen in Fig. 3.3. Usually, experimental results, e.g., for $\langle X_{\mathrm{max}} \rangle$ and $\sigma(X_{\mathrm{max}})$, are compared with predictions based on air shower simulations. For energy ranges that are not accessible by particle accelerators, extrapolations of measured particle accelerator data to higher energies are necessary as a basis for these air shower simulations [354]. Especially for modeling the first interactions in UHECR air showers, substantial extrapolations of cross sections measured at lower center-of-mass energies in collider experiments are usually needed.

Such a comparison with predictions based on air shower simulations has been made in Fig. 3.3. In this figure, predictions based on air shower simulations for pure protons and pure iron nuclei are shown for comparison, taking into account three different and well-known hadronic interaction

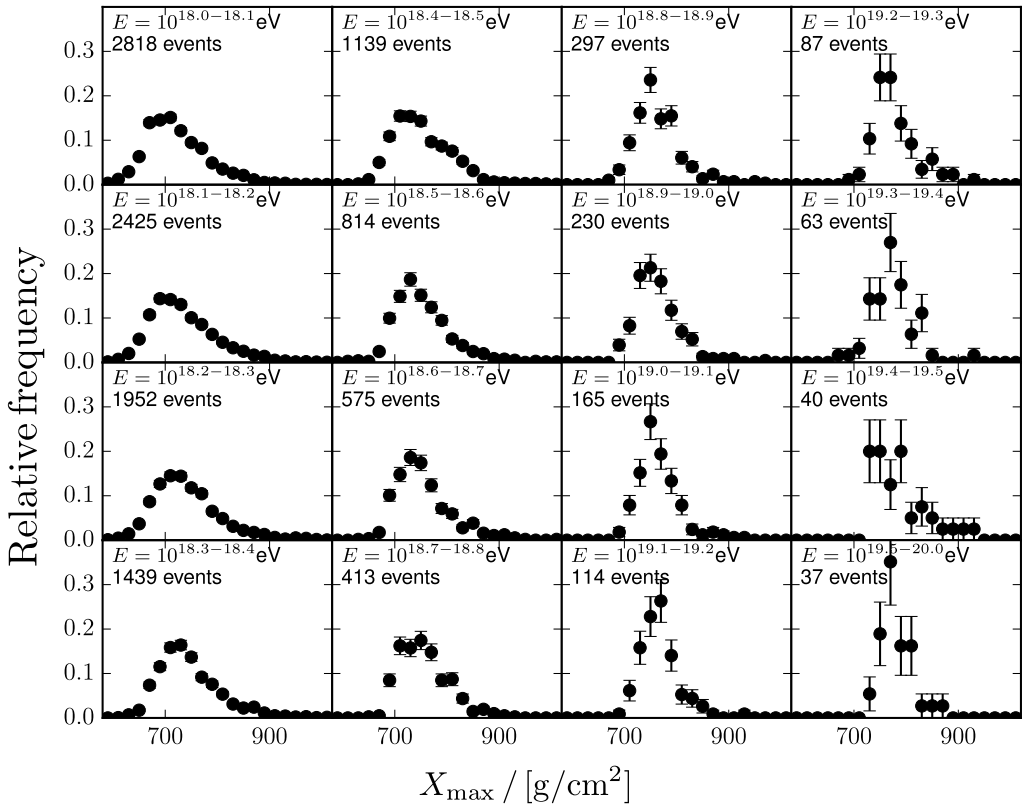

Figure 3.2: $X_{\max}$ distribution in various energy intervals as measured by the Pierre Auger Observatory. As expected, the statistics fall with increasing energy. Data: from [274].

models. Since in Fig. 3.3 also radio results of the Pierre Auger Observatory are shown, which are labeled with "RD", it should be noted that after the amazing progress made in the past years, recent AERA results have shown good agreement between the Pierre Auger Observatory radio and fluorescence measurements of $\langle X_{\max} \rangle$ [355].

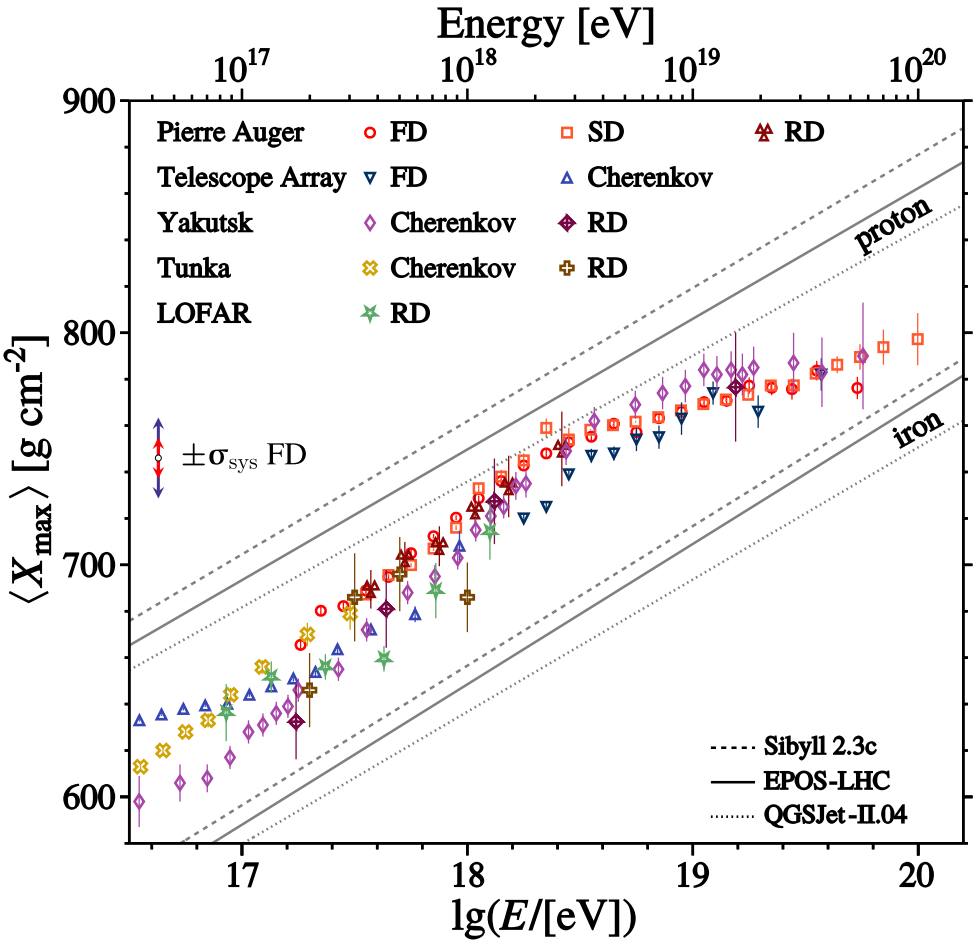

Figure 3.3: Measurements of $\langle X_{\max} \rangle$ by various experiments and observatories in a range of multiple decades of particle energy E. The results of different detection techniques are also shown. For comparison, predictions for pure protons and iron nuclei when considering three different and popular hadronic interaction models are shown: EPOS-LHC, QGSJET II.04, and SIBYLL2.3c. Figure: from [353].

3.3 Arrival directions

Since UHECRs can be detected, numerous attempts have been made to obtain information about their unknown sources from the distribution of their arrival directions and possible anisotropies in this distribution. A major challenge for finding the sources of UHECRs is the fact that UHECRs are deflected during their propagation from their sources to Earth in the extragalactic magnetic field (see section 2.5) and the galactic magnetic field (see section 2.4), thus hiding their origin. In addition, it is important to have a sufficiently high number of detected UHECRs in order to be able to distinguish an actual anisotropy in the distribution of the UHECR arrival directions from a random distribution. The UHECRs detected during the operation of the two largest observatories for the detection of UHECRs, namely the Pierre Auger Observatory (see section 2.7.1) and the Telescope Array (see section 2.7.2), are particularly suitable for this purpose.

Since large-scale surveys of galaxies and clusters of galaxies, such as the 2MASS Redshift Survey [356], mapping the distribution of matter across the nearby universe to some extent showed an anisotropic distribution, an anisotropic distribution of the arrival directions of UHECRs could be possible, provided that the UHECR sources follow the anisotropic local matter distribution and the deflections of UHECRs in the extragalactic magnetic field and galactic magnetic field are not too strong.

In the past, numerous searches for anisotropies in the arrival directions of UHECRs were unsuccessful. For example, several anisotropy tests were performed in the article [357], but none of these tests was able to provide statistically significant evidence of anisotropy. The anisotropy tests in the aforementioned article included, for example, an updated investigation of the correlation of events with AGNs in the Véron-Cetty and Véron (VCV) catalog [358]. Also investigating the autocorrelation of events, the cross-correlation of UHECR arrival directions with various catalogs of potential UHECR sources, and other tests could not show a statistically significant evidence of anisotropy in this article.

Even the recent use of arrival directions of the highest-energy UHECRs detected in the northern hemisphere by the TA Collaboration, more precisely of UHECRs with $E > 100\,\mathrm{EeV}$, i.e., EHECRs, could not solve the

decades-old mystery of the sources of UHECRs. In this context, reference should be made to the recently published article by the TA Collaboration [359]. In this article, the TA Collaboration reports, inter alia, on the detection of a particularly energetic EHECR with an energy of $E_{\mathrm{TA052721}} = 244 \pm 29(\mathrm{stat.})^{+51}_{-76}(\mathrm{syst.})\,\mathrm{EeV}$ on May 27th, 2021 using the TA SD. Note that this reported energy E_{TA052721} has already been calibrated to the energy that the TA FD would measure using the factor 1.27^{-1} [360].

Interestingly, the sky area, which is referred to as the location of the so-called "Local Void" [361], and the arrival direction of this EHECR, which is particularly interesting due to its very high energy, show a match. In addition, considering deflections in the GMF and assuming various elements of which the EHECR could have consisted did not change the fact that the arrival direction of this EHECR and the sky area of the Local Void are consistent. This is surprising, as there are also a few galaxies in the Local Void, such as NGC 6503 [362], but none that were previously considered as possible sources of UHECRs by a notable number of researchers.

Totally contrary to the expectations of the TA researchers, the 28 EHECRs examined by the TA in the aforementioned article did not show clustering, which means a clear anisotropy in their arrival directions, but instead an isotropic distribution. The EHECR with E_{TA052721} came from a different direction than that of the medium-scale "TA hot spot" [124] and there was also no evident clustering in the direction of the TA hot spot.

As in review [363], it can be concluded that so far no small-scale or medium-scale anisotropies could be detected conclusively ($s \geq 5\sigma$). Nevertheless, interesting hints for anisotropies need to be further studied, especially in view of an increasing number of observed UHECRs in the upcoming years. With increasing statistics due to detector enhancements such as AugerPrime (see section 2.7.1.4) and TA×4 (see section 2.7.2.4), one can look forward to an exciting time and exciting new results on the arrival directions of UHECRs in the upcoming years.

In contrast, at lower energies ($E > 8\,\mathrm{EeV}$) and on large angular scales, the first observation of a significant ($s > 5\sigma$) large-scale dipolar anisotropy [119] in the arrival directions of UHECRs by the Pierre Auger Collaboration was a great breakthrough. More research on this dipolar anisotropy can be found in [364, 365]. The dipolar anisotropy seems to increase in amplitude

with energy. Since the dipole points far away from the direction of the Galactic center, this suggests an extragalactic origin of the UHECRs.

The following section 3.3.1 provides information on map projections, since the use of map projections is not uncommon in connection with UHECRs. In section 3.3.2, a short overview about directional expansions is given.

3.3.1 Map projections

In connection with the arrival directions of UHECRs, the use of map projections is not uncommon. The history of map projections is several millennia long [366–368]. But even in this decade, new map projections have been invented and studied [369].

To illustrate different global map projections, it is shown in Fig. 3.4 a world map in which the positions of the Pierre Auger Observatory, the Telescope Array, and the Ice-Cube Neutrino Observatory are marked with yellow hexagons using six different map projections. The world map used can also be found in a labeled version in Fig. 2.11, using a Mollweide map projection for its representation. To visualize the (angular and areal) distortion inherent in the different projections and to show how the distortion varies for different positions on the map, Tissot's indicatrices (red ellipses) are used [370, 371]. It is useful to note that for equal area map projections, all indicatrices have the same area, but for conformal map projections, all indicatrices are circles. Hence, of the six map projections compared, the Hammer-Aitoff projection, as well as the Mollweide projection and the Sinusoidal projection are equal area map projections. All three are also frequently found in publications related to UHECRs (for example Refs. [372–374]), with the latter (Sinusoidal projection) seeming to be far more common in older publications than in recent publications. Since not all Tissot's indicatrices of the projections are circles, it is easy to see that none of the shown map projections is a conformal map projection. However, being a conformal map projection is not ordinary a necessary property of a map projection in the context of UHECRs, so that this property, in contrast to the property of being an equal area map projection, can usually be neglected in the sense of a compromise. Such a compromise is unavoidable, because distortions are inevitable when mapping the sphere onto the plane (by map projection) Gauss [375].

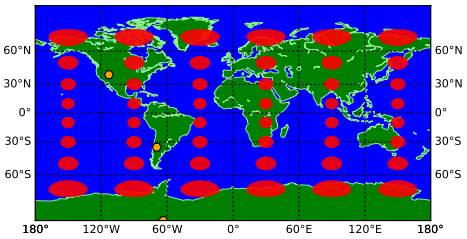

(a) Gall stereographic projection

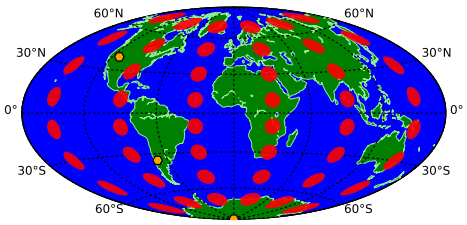

(b) Hammer-Aitoff projection

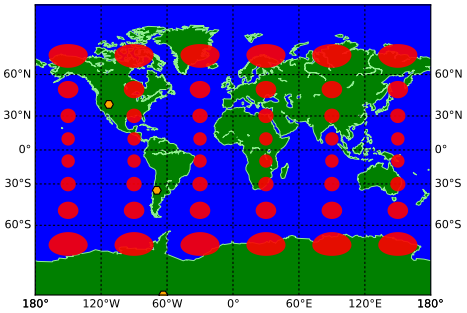

(c) Miller cylindrical projection

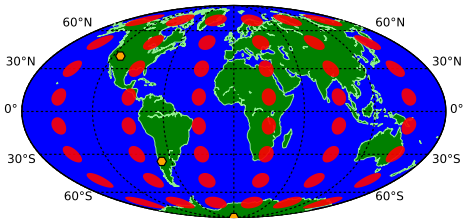

(d) Mollweide projection

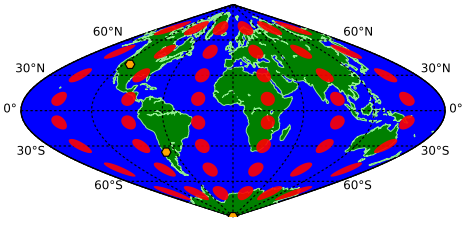

(e) Sinusoidal projection

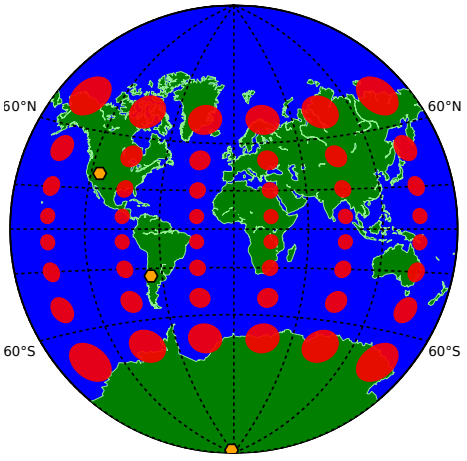

(f) Van der Grinten projection

Figure 3.4: Comparison of common full-sky map projections. Tissot's indicatrices (red ellipses) are used to visualize the (angular and areal) distortion inherent in the different projections and to show how the distortion varies for different positions on the map. Note that for equal area map projections, all indicatrices have the same area, but for conformal map projections, all indicatrices are circles.

3.3.2 Directional expansions

When a scalar quantity is given as a function I of some direction (e.g., the intensity of UHECRs arriving at the observer as a function of the arrival direction), there are different possibilities to specify the direction variable and thus to parametrize the function. One commonly chosen option is to use spherical angular coordinates $\theta \in [0, \pi]$ and $\phi \in [0, 2\pi)$ to specify the direction. The directional distribution function is then parametrized as $I(\theta, \phi)$. Another option is to specify the direction by a normalized direction vector $\hat{n}$ and thus to parametrize the distribution function as $I(\hat{n})$.

A relation between both types of direction variables can be obtained by a parametrization of the direction vector $\hat{n}$ by the angular coordinates θ and ϕ:

$$\hat{n}(\theta, \phi) = \begin{pmatrix} \sin(\theta)\cos(\phi) \\ \sin(\theta)\sin(\phi) \\ \cos(\theta) \end{pmatrix}. \tag{3.3}$$

For both parametrizations $I(\theta, \phi) \equiv I(\hat{n})$, the directional distribution function can be expanded with respect to its directional variable(s). The directional expansion of $I(\theta, \phi)$ with respect to the spherical angular coordinates θ and ϕ constitutes an *angular multipole expansion*. It is therefore also called *spherical multipole expansion*.

Following the notation of [376], the expansion is given by

$$I(\theta, \phi) = \sum_{l=0}^{\infty} \sum_{m=-l}^{l} I_{lm} Y_l^m(\theta, \phi) \tag{3.4}$$

with the spherical harmonics

$$Y_l^m(\theta, \phi) = \sqrt{\frac{2l+1}{4\pi} \frac{(l-m)!}{(l+m)!}} P_l^m(\cos(\theta)) e^{\mathrm{i}m\phi}, \tag{3.5}$$

where the associated Legendre polynomials $P_l^m(x)$ are defined as

$$P_l^m(x) = \frac{(-1)^m}{2^l l!} (1-x^2)^{m/2} \partial_x^{l+m} (x^2-1)^l. \tag{3.6}$$

The expansion coefficients I_{lm} with $l = 0, \ldots, \infty$ and $m = -l, \ldots, l$ are

in general independent and given by

$$I_{lm} = \int_0^{\pi} \mathrm{d}\theta \, \sin(\theta) \int_0^{2\pi} \mathrm{d}\phi \, I(\theta, \phi) Y_l^{m\star}(\theta, \phi), \tag{3.7}$$

where the star $\star$ denotes complex conjugation. Since the expansion coefficients (3.7) are not rotationally invariant, the *total power* of $I(\theta, \phi)$

$$\int_0^{\pi} \mathrm{d}\theta \, \sin(\theta) \int_0^{2\pi} \mathrm{d}\phi \, |I(\theta, \phi)|^2 = \sum_{l=0}^{\infty} (2l+1) C_l \tag{3.8}$$

and the *angular power spectrum* given by the contributions

$$C_l = \frac{1}{2l+1} \sum_{m=-l}^{l} |I_{lm}|^2 , \tag{3.9}$$

which are rotationally invariant, are often of particular interest. A further quantity of interest in this context is the *dipole amplitude*. It can be obtained from the value of C_1 as $\frac{3}{2\sqrt{\pi}} \sqrt{C_1}$ [127].

4 Methods

4.1 Simulation of the propagation of UHECRs and neutrinos

The simulation process is sketched in a strongly simplified form in Figure 4.1. When simulating the propagation of UHECRs, their original attributes

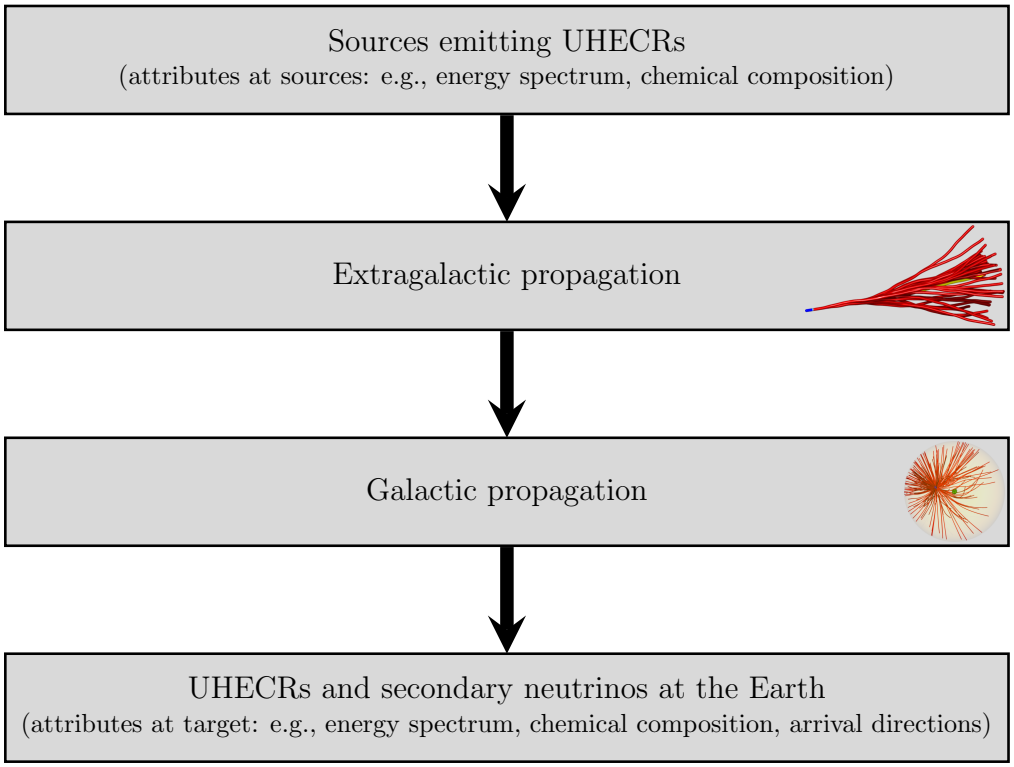

Figure 4.1: Schematic overview of the simulation process.

at their sources (such as their initial energy spectrum, chemical composition, and momentum) can be influenced by interactions with the extragalactic photon background, deflections in extragalactic and galactic magnetic fields, and cosmological effects such as the redshift evolution of the photon

background and the adiabatic expansion of the universe. The UHECRs that arrive at their target Earth usually have different attributes than they had when they were emitted from their sources.

In order to simulate the propagation of UHECRs from their sources to the target Earth, the author made use of the four-dimensional mode of the Monte Carlo code CRPropa 3 [261, 377]. All three spatial degrees of freedom and the cosmological time evolution of the universe are taken into account in this four-dimensional mode. It was assumed that the sources are discrete objects. The positions of the sources were randomly selected following the large-scale structure of Dolag et al. [144], a model for the universe's local mass distribution that is popular. Near-Earth sources, whose UHECRs are only marginally influenced by the EGMF, were considered to have a minimum distance of $d_{\min} = 10\,\mathrm{Mpc}$ from the observer in order to reduce their effect. This excludes the Council of Giants including Centaurus A. Because neutrinos are able to reach the Earth from greater distances than UHECRs, a value of $z_{\max} \approx 1.3$ for simulations focusing on UHECRs and $z_{\max} \approx 4$ for simulations focusing on neutrinos was selected for the sources' maximal redshift. A maximum comoving distance of $d_{\max} \approx 4\,\mathrm{Gpc}$ in the first case and $d_{\max} \approx 7\,\mathrm{Gpc}$ in the second case are equivalent to this choice. In line with established density bounds, the source density ρ has been selected as $\rho \approx 10^{-4}\,\mathrm{Mpc}^{-3}$ [378]. Apart from that, it was assumed that all sources have the same properties and that they emit UHECRs isotropically, consisting of the five[1] representative elements ^{1}H, ^{4}He, ^{14}N, ^{28}Si, and ^{56}Fe with a power-law energy spectrum $J_0(E_0) = \mathrm{d}N_0/\mathrm{d}E_0$ with an exponential cut-off for rigidities $E_0/Z_\alpha \geq R_{\mathrm{cut}}$:

$$J_0(E_0) \propto \sum_\alpha f_\alpha E_0^{-\gamma} \begin{cases} 1\,, & \text{if } \frac{E_0}{Z_\alpha} < R_{\mathrm{cut}}\,, \\ e^{1-\frac{E_0}{Z_\alpha R_{\mathrm{cut}}}}\,, & \text{if } \frac{E_0}{Z_\alpha} \geq R_{\mathrm{cut}}\,. \end{cases} \tag{4.1}$$

According to [2], $\mathrm{d}N_0(E_0)$ stands for the number of particles emitted with an energy within the range from E_0 to $E_0 + \mathrm{d}E_0$. The variable Z_α denotes

[1] In contrast, the author reported in [1] results for only four instead of five representative elements, namely: ^{1}H, ^{4}He, ^{14}N, and ^{56}Fe. A comparison with the author's results subsequently reported in [2] reveals that neglecting the intermediate mass nuclei of element ^{28}Si reduces the agreement between the simulated data and the measurement data collected by the Pierre Auger Observatory.

the atomic number of an element $\alpha \in \{\mathrm{H}, \mathrm{He}, \mathrm{N}, \mathrm{Si}, \mathrm{Fe}\}$, while R_{cut} stands for the so-called cut-off rigidity, above which the particle flow emitted at the sources undergoes exponential suppression. The fraction of particles of an element α among all emitted particles, and thus the chemical composition of the UHECRs at their sources, are described by the parameters f_α with $\alpha \in \{\mathrm{H}, \mathrm{He}, \mathrm{N}, \mathrm{Si}, \mathrm{Fe}\}$ and normalization condition $\sum_\alpha f_\alpha = 1$. Moreover, γ symbolizes the spectral index. To acquire trustworthy statistics, the simulations were carried out until over $5 \cdot 10^6$ UHECRs had arrived at the observer. The simulations covered the propagation of UHECRs and secondary neutrinos, but the propagation of ultra-high energy photons (which could not have been measured so far) to Earth was disregarded.

The model of Gilmore et al. [217] (the so-called "fiducial" model) was chosen for the EBL. Furthermore, the photodisintegration cross sections from the TALYS code[2] [379, 380] with adjusted parameters as specified in [218] (this is the default in CRPropa 3) were used. Besides that, reflective boundary conditions were utilized in conjunction with the extensively structured Benchmark EGMF (see section 2.5) that represents a relatively strong EGMF [381, 382]. Until colliding with a sphere, called the "observer", with a radius of r_{obs}, the particles propagated through the EGMF. The observer was positioned at the Earth and recorded all particles arriving with redshift $-0.025 < z < 0.025$, ensuring that no simulated particle collided with the observer more than once. The use of a smaller sphere or redshift range was found to have no qualitative impact on the simulation results. The observer of radius $r_{\mathrm{obs}} = 1\,\mathrm{Mpc}$ was selected for simulations concentrating on UHECRs, while a radius r_{obs} of 2 Mpc was selected for neutrino simulations (in order to accomplish adequate statistics), alongside the aforementioned redshift range for improved statistics. It was found that the redshift window should be set symmetrically around 0 in order to achieve the highest possible statistics and the largest possible redshift window.

Simulations have been performed with EGMF (model I) and without EGMF (model II). In each case, various values of the source parameters γ, R_{cut}, and f_α were examined, and a fitting procedure akin to that discussed in [114] was employed to identify the specific parameter values that yield the optimal agreement between the energy spectrum and chemical composition

[2] `http://www.talys.eu/documentation/`

of the simulated UHECRs observed at the observer and the corresponding data from the Pierre Auger Observatory (refer to chapter 5). The assumptions specified above establish several astrophysical models [2, 3].

Through appropriate post-processing of the simulation data for the UHECRs and cosmogenic neutrinos at the observer, the values for the spectral index are indirectly incorporated rather than directly via the energy spectrum at the sources. The spectral index in the initial energy spectrum was set to one in order to speed up the simulations and improve the statistics at high energies. Afterwards, the re-weighting technique described in [383] was applied to the simulation data in order to properly change the spectral index to its target value. Finally, the simulation outcomes for the fluxes of UHECRs and neutrinos at the observer are rescaled by a suitable global constant factor to facilitate comparison of the simulated neutrino flux with the upper limits for the neutrino flux from the Pierre Auger and IceCube Neutrino Observatories. This factor has been determined so that the simulated flux of UHECRs at arrival energy 10^{19} eV equals the flux of UHECRs recorded at this energy by the Pierre Auger Observatory.

For the simulations where the arrival directions were considered, as in section 6.2, the effect of the GMF on the particles was calculated with CRPropa using the JF 2012 model of Jansson and Farrar [230, 242, 261] for the GMF. It is assumed, as it is usual in the energy range under consideration, that the GMF has an influence on the arrival directions of the UHECRs, but not on their energy spectrum or chemical composition.

In the previously mentioned case distinctions for simulations that focus on UHECRs and simulations that focus on neutrinos, the first case corresponds to the simulations done for chapter 5 and sections 6.1 and 6.2 that have focused on UHECRs and the second case corresponds to the simulations done for section 6.3 that have focused on neutrinos.

4.2 Fitting procedure

In contrast to [114], which involves folding the simulated energy spectrum with a function that models detector effects before comparing it to the raw data from the Pierre Auger Observatory, the fitting procedure applied in the present work directly fits the simulated energy spectrum to the published data for the energy spectrum from the Pierre Auger Observatory [346], which has already been adjusted for detector effects. Only experimental data exceeding 5 EeV (which is approximately the energy that is associated with the "ankle" in the experimental energy spectrum [346]) were considered when fitting the energy spectrum, as the data for lower energies may include a substantial galactic contribution.

The Pierre Auger Observatory measures "the position of the maximum of energy deposition per atmospheric slant depth" [384], which is commonly called "depth of the shower maximum" X_{max} [274], by observing the longitudinal profile of extensive air showers (see section 2.6) instead of directly measuring the chemical composition of the UHECRs arriving at Earth. Currently, the most established technique for determining the mass composition of UHECRs is the measurement of the composition-sensitive quantity X_{max}. To enable a direct comparison with the experimental data (see section 3.2), the simulation outcomes for the chemical composition of the arriving UHECRs were converted into a distribution of the quantity X_{max}. The generalized Gumbel functions [385], which are based on air-shower simulations using the CONEX code [386] and the EPOS-LHC model for hadronic interactions [387], were used to parametrize the X_{max} distribution for particles arriving with energy E and mass number A. The obtained Gumbel distribution was multiplied by the energy-dependent detector acceptance and the product was convolved with the energy-dependent detector resolution in order to account for detector effects [274].

In order to identify the source properties (i.e., f_α, γ, and R_{cut}) which optimally describe the Pierre Auger Observatory data, a fit procedure akin to that proposed by Erdmann and Walz [388] was implemented. The only data of simulated UHECRs that are taken into consideration in this procedure are those of the UHECRs that arrived at the observer. Initially, these data are binned with regard to the energy E^{s} and atomic number Z^{s} at

the sources and with regard to the energy E^{o} and mass number A^{o} at the observer [389]. This results in the matrices $(E_i^{\mathrm{s}}, Z_j^{\mathrm{s}})_{i,j}$ and $(E_k^{\mathrm{o}}, A_l^{\mathrm{o}})_{k,l}$, where the element $(E_i^{\mathrm{s}}, Z_j^{\mathrm{s}})$ denotes the number of UHECRs with initial energy E_i^{s} and atomic number Z_j^{s}. The number of particles with observed energy E_k^{o} and mass number A_l^{o} are described by the element $(E_k^{\mathrm{o}}, A_l^{\mathrm{o}})$. A propagation tensor $(p_{k,l,i,j})_{k,l,i,j}$ with

$$(E_k^{\mathrm{o}}, A_l^{\mathrm{o}}) = \sum_{i,j} p_{k,l,i,j}(E_i^{\mathrm{s}}, Z_j^{\mathrm{s}}) \tag{4.2}$$

is derived from these matrices. The fraction of UHECRs that are emitted at the sources with energy E_i^{s} and atomic number Z_j^{s} and that reach the observer with energy E_k^{o} and mass number A_l^{o} is designated as the tensor's element $p_{k,l,i,j}$. The energy spectrum and chemical composition at the sources are mapped by this tensor onto the energy spectrum and mass spectrum at the observer. In the simulations, the energy spectrum at the sources, described by equation (4.1), is a function of the parameters f_α, γ, and R_{cut}. The parameters f_α symbolize the chemical composition at the sources. Thus, without requiring extra time-consuming simulations, the propagation tensor $(p_{k,l,i,j})_{k,l,i,j}$ enables a fast calculation of the energy spectrum and mass spectrum at the observer for every choice of the free parameters f_α, γ, and R_{cut}.

By utilizing the matrix $(E_k^{\mathrm{o}}, A_l^{\mathrm{o}})_{k,l}$, it is possible to determine the probability $p_{k,l}$ of observing a particle with energy E_k^{o} and mass number A_l^{o}. Furthermore, the probability of observing a particle with energy E_k^{o} is denoted by $p_k = \sum_l p_{k,l}$ in this work. The energies E_k^{o} are multinomially distributed. The total particle flux is not utilized as a free parameter. The logarithm of the likelihood $\mathcal{L}_J$ for observing an energy spectrum with N_k events detected at energy E_k^{o} can be written with $N = \sum_k N_k$ as

$$\ln(\mathcal{L}_J) = \ln(N!) - \sum_k \ln(N_k!) + \sum_k N_k \ln(p_k)\,. \tag{4.3}$$

The benefit of using the multinomial likelihood in equation (4.3) is that it can account for bins with zero observed events, unlike the methodology in [388], which assumes a normal distribution in the bins of the energy spectrum. A further possible advantage of equation (4.3) is that in the

future it could also be used for an energy- and mass-dependent exposure that alters the probabilities $p_{k,l}$.

Furthermore, one can address the likelihood $\mathcal{L}_{X_{\max}}$ of the observed $X_{\max}$ distribution. Therefore, utilizing the procedure mentioned above, a corresponding matrix $(E_k^{\mathrm{o}}, X_{\max,m}^{\mathrm{o}})_{k,m}$ was calculated from the matrix $(E_k^{\mathrm{o}}, A_l^{\mathrm{o}})_{k,l}$, where the element $(E_k^{\mathrm{o}}, X_{\max,m}^{\mathrm{o}})$ describes the number of particles with the observed energy E_k^{o} and the depth of the shower maximum $X_{\max,m}^{\mathrm{o}}$. The probability $\hat{p}_{k,m}$ of observing a particle with energy E_k^{o} and depth of the shower maximum $X_{\max,m}^{\mathrm{o}}$ was obtained from the matrix $(E_k^{\mathrm{o}}, X_{\max,m}^{\mathrm{o}})_{k,m}$ for each k and m. The likelihood $\mathcal{L}_{X_{\max}}$ of observing an $X_{\max}$ distribution given that N_k events are detected with energy E_k^{o} and $N_{k,m}$ events are detected with energy E_k^{o} as well as depth of the shower maximum $X_{\max,m}^{\mathrm{o}}$ is described by

$$\mathcal{L}_{X_{\max}} = \prod_k N_k! \prod_m \frac{1}{N_{k,m}!} \hat{p}_{k,m}^{N_{k,m}} \,. \tag{4.4}$$

The individual likelihoods $\mathcal{L}_J$ and $\mathcal{L}_{X_{\max}}$ are multiplicative since the energy spectrum and $X_{\max}$ distribution observed by the Pierre Auger Observatory can be considered here as independent measurements. This yields the following result for the combined likelihood of the observed energy spectrum and $X_{\max}$ distribution:

$$\mathcal{L} = \mathcal{L}_{X_{\max}} \mathcal{L}_J \,. \tag{4.5}$$

In order to determine which values of the parameters f_α, γ, and R_{cut} lead to the optimal agreement of the simulation results with the corresponding data from the Pierre Auger Observatory, it is possible to use all three likelihoods, which are denoted here by the symbols $\mathcal{L}_J$, $\mathcal{L}_{X_{\max}}$, and $\mathcal{L}$.

The deviances are useful for quantifying how well the simulation outcomes match with data from the Pierre Auger Observatory for a certain selection of values for f_α, γ, and R_{cut}. Therefore, the following deviances were considered:

$$D_J = -2 \ln\left(\frac{\mathcal{L}_J}{\mathcal{L}_J^{\mathrm{sat}}}\right), \tag{4.6}$$

$$D_{X_{\max}} = -2 \ln\left(\frac{\mathcal{L}_{X_{\max}}}{\mathcal{L}_{X_{\max}}^{\mathrm{sat}}}\right), \tag{4.7}$$

$$D = -2 \ln\left(\frac{\mathcal{L}}{\mathcal{L}^{\mathrm{sat}}}\right) = D_J + D_{X_{\max}} \,. \tag{4.8}$$

In this context, $\mathcal{L}_J^{\mathrm{sat}}$, $\mathcal{L}_{X_{\mathrm{max}}}^{\mathrm{sat}}$, and $\mathcal{L}^{\mathrm{sat}}$ represent the likelihoods associated with $\mathcal{L}_J$, $\mathcal{L}_{X_{\mathrm{max}}}$, and $\mathcal{L}$ for the saturated model that perfectly describes the Pierre Auger Observatory data. $\mathcal{L}_J^{\mathrm{sat}}$ and $\mathcal{L}_{X_{\mathrm{max}}}^{\mathrm{sat}}$ are specified by

$$\mathcal{L}_J^{\mathrm{sat}} = \prod_k \frac{N!}{N_k!} \left(\frac{N_k}{N}\right)^{N_k} \tag{4.9}$$

and

$$\mathcal{L}_{X_{\mathrm{max}}}^{\mathrm{sat}} = \prod_k N_k! \prod_m \frac{1}{N_{k,m}!} \Big(\frac{N_{N,k}}{N_k}\Big)^{N_{k,m}} . \tag{4.10}$$

The values of the parameters for f_α, γ, and R_{cut} that provide the best possible agreement when comparing the simulation results for the observed energy spectrum, X_{max} distribution, or both energy spectrum and X_{max} distribution with the corresponding data from the Pierre Auger Observatory, respectively, are determined by minimizing the deviances D_J, $D_{X_{\mathrm{max}}}$, and D with respect to f_α, γ, and R_{cut}. Following [388], Bayesian inference was performed using a Markov chain Monte Carlo method implemented in the package PyMC 2.3 [390] to estimate the uncertainties in the best-fit values of the parameters f_α that originate from uncertainties in the data from the Pierre Auger Observatory. Estimates for the uncertainties in the best-fit values were obtained using the profile likelihood method as described in [114] with respect to the parameters γ and R_{cut}. For these parameters, values that correspond to the deviance interval $D_{\mathrm{min}} \leq D \leq D_{\mathrm{min}} + 1$, where D_{min} is the minimal value of the deviance D, were used.

In the fit procedure discussed above, only Pierre Auger Observatory data for energies exceeding $10^{18.7}\,\mathrm{eV} \approx 5\,\mathrm{EeV}$ were taken into account, as it is widely believed that observed UHECR events are mostly extragalactic in origin for these energies [104, 391]. The Pierre Auger Observatory data used for this energy range contain 15 nonzero data points for the energy spectrum and a total of 110 nonzero data points for the X_{max} distribution [129]. The logarithmic energies $\log_{10}(E/\mathrm{EeV})$ at the sources were binned in increments of 0.02, whereas at the observer they were binned in larger increments of 0.1, for the purpose of constructing the matrices $(E_i^{\mathrm{s}}, Z_j^{\mathrm{s}})_{i,j}$, $(E_k^{\mathrm{o}}, A_l^{\mathrm{o}})_{k,l}$, and $(E_k^{\mathrm{o}}, X_{\mathrm{max},m}^{\mathrm{o}})_{k,m}$. The second bin width is the same as the bin width of the considered energy spectrum data from the Pierre Auger Observatory. For the mass number A and the atomic number Z, increments of one were used.

The author chose a bin width of $1\,\mathrm{g/cm^2}$ for the simulated $X_{\max}$ distribution and binned the $X_{\max}$ data according to energy in the same manner as for the energy spectrum. For the data from the Pierre Auger Observatory under consideration, the bin width for the $X_{\max}$ distribution is $20\,\mathrm{g/cm^2}$ and the $X_{\max}$ data are binned with respect to the logarithmic energy $\log_{10}(E/\mathrm{EeV})$, using a bin width of 0.1 until $\log_{10}(E/\mathrm{EeV}) = 1.5$ and a final bin width of 0.5.

4.3 Calculation of the angular power spectrum

For the analysis of the distribution of the UHECR arrival directions at Earth, this distribution was binned into a HEALPix grid[3] [392] composed of 49152 cells, each with an identical solid angle. Note that these cells do not have to be rectangular in shape. This led to a coarse-grained distribution $\mathcal{N}(E, \hat{\boldsymbol{n}})$ of the number of detected UHECRs. Here, the number of detected UHECRs $\mathcal{N}$ is a function of their arrival energy E and arrival direction $\hat{\boldsymbol{n}}$. The unit vector $\hat{\boldsymbol{n}}$ corresponds to the normalized and sign-inversed momentum vector of an UHECR arriving at the target Earth. The angular resolution of the coarse-grained distribution was chosen similar to that of the Pierre Auger Observatory [393] in the relevant energy range by selecting 49152 cells. The rescaled particle number distribution $(\mathcal{N}(E, \hat{\boldsymbol{n}}) - \langle\mathcal{N}\rangle(E))/\langle\mathcal{N}\rangle(E)$, where $\langle\,\cdot\,\rangle$ denotes an angular average, describes the relative fluctuations in the particle number. This function was expanded into spherical harmonics $Y_l^m(\hat{\boldsymbol{n}})$:

$$\frac{\mathcal{N}(E, \hat{\boldsymbol{n}}) - \langle\mathcal{N}\rangle(E)}{\langle\mathcal{N}\rangle(E)} = \sum_{l=0}^{l_{\max}} \sum_{m=-l}^{l} a_{lm}(E) Y_l^m(\hat{\boldsymbol{n}}) \,. \tag{4.11}$$

In this equation, $l_{\max}$ represents the maximum order of the expansion of interest, and $a_{lm}(E)$ are the expansion coefficients that depend on energy. The corresponding angular power spectrum for the arrival direction distribution of the simulated UHECRs is thus given by

$$C_l(E) = \frac{1}{2l+1} \sum_{m=-l}^{l} |a_{lm}(E)|^2 \,. \tag{4.12}$$

[3] `http://healpix.jpl.nasa.gov/`

where $l \in \{0, \ldots, l_{\max}\}$. The rescaling of $\mathcal{N}(E, \hat{\boldsymbol{n}})$ implies $C_0(E) = 0$. The $C_l(E)$ coefficients depend on the energy and are rotationally invariant. These coefficients describe the angular distribution of the UHECR arrival directions for $l \geq 1$, roughly corresponding to solid angle scales of $2\pi/l\,\mathrm{sr}$ (i.e., angular scales of π/l sr). Thus, to examine the distribution of arrival directions and identify potential anisotropies, the angular power spectrum is a valuable quantity. The subsequent discussion focuses on the angular power spectrum rather than the orientations associated with the multipoles. This is because the orientations depend strongly on the details of the model for the local mass distribution of the universe, while the angular power spectrum is a far more robust and reliable quantity.

In order to identify the coefficients $C_l(E)$ that can be significantly measured (with $s > 5\sigma$) in the near future, the upper 5σ confidence bounds for isotropy were determined. It can be estimated that in the upcoming years, UHECR observatories will detect roughly 50000, 34988, and 18288 UHECR events with energies greater than 8 EeV, 10 EeV, and 15 EeV, respectively. In addition, it were generated 10^7 data sets of 50000, 34988, and 18288 UHECR events with random arrival directions uniformly distributed on the unit sphere for these three energy intervals. Based on these data sets, the mean values and standard deviations (σ) of the coefficients C_l were calculated. This, in turn, allowed for the calculation of the upper 5σ confidence bound for isotropy.

5 Reconstructed source properties

Using the methods described in chapter 4 and data from the Pierre Auger Observatory, the author was able to reconstruct the properties of the sources of the UHECRs that have been detected at the Earth. In this chapter, the reconstructed properties of the sources are presented. Furthermore, the effects of the EGMF and the cosmological evolution of the sources on the reconstructed source parameters are addressed.

5.1 Dependence on the extragalactic magnetic field

The best-fit parameter values and the corresponding minimal deviances, presented in Table 5.1, are obtained by employing models I (which includes EGMF) and II (which excludes EGMF). These values are obtained through fitting the spectral index γ, the cut-off rigidity R_{cut}, and the element fractions f_α with $\alpha \in \{\mathrm{H}, \mathrm{He}, \mathrm{N}, \mathrm{Si}, \mathrm{Fe}\}$ to the Pierre Auger Observatory data by minimizing the deviance D.

The table shows that the best-fit values for the parameters γ, R_{cut}, and f_α markedly depend on the chosen EGMF. One can see in Table 5.1 that the minimal deviance D_{min} is less for model I than for model II, indicating that the author's model incorporating an EGMF is in better agreement with the data from the Pierre Auger Observatory compared to his model excluding an EGMF. For reference and comparison, Table 5.1 also presents the findings from the prior global fit to the experimental data [114]. This previous fit is based on 1D simulations of UHECR propagation, assuming a

Model	γ	$\log_{10}\left(\frac{R_{\mathrm{cut}}}{\mathrm{eV}}\right)$	$f_{\mathrm{H}}/\%$	$f_{\mathrm{He}}/\%$	$f_{\mathrm{N}}/\%$	$f_{\mathrm{Si}}/\%$	$f_{\mathrm{Fe}}/\%$	$D_{\mathrm{min}} = D^{J}_{\mathrm{min}} + D^{X_{\mathrm{max}}}_{\mathrm{min}}$
I	$1.61^{+0.08}_{-0.07}$	$18.88^{+0.03}_{-0.07}$	$3.0^{+1.6}_{-3.0}$	$2.1^{+1.2}_{-2.1}$	$73.5^{+4.4}_{-2.2}$	$21.0^{+1.2}_{-0.8}$	$0.4^{+0.2}_{-0.4}$	$191.9 = 37.3 + 154.6$
II	$0.61^{+0.05}_{-0.06}$	$18.48^{+0.01}_{-0.02}$	$11.0^{+4.6}_{-11.0}$	$13.8^{+6.6}_{-13.8}$	$67.9^{+12.7}_{-9.9}$	$7.2^{+2.2}_{-1.3}$	$0.1^{+0.1}_{-0.1}$	$221.3 = 48.7 + 172.6$
see [114]	$0.87^{+0.08}_{-0.06}$	$18.62^{+0.02}_{-0.02}$	0	0	88	12	0	$191.9 = 29.2 + 162.7$

Table 5.1: In order to obtain the best-fit parameter values for γ, R_{cut}, and f_α listed here with $\alpha \in \{\mathrm{H}, \mathrm{He}, \mathrm{N}, \mathrm{Si}, \mathrm{Fe}\}$, the deviance D was minimized. The minimum deviance D_{min} and its components D^{J}_{min} and $D^{X\mathrm{max}}_{\mathrm{min}}$ were calculated for the models: model I, which includes EGMF, and model II, which excludes EGMF [2]. The results of the 1D simulations reported by [114] are also presented for comparison. Caption: cf. Tab. 1 in [2]. Table: from Tab. 1 in [2].

homogeneous source distribution and excluding an EGMF. [1] It is interesting that for model II, in which the EGMF is excluded and 4D simulations with discrete sources following the local mass distribution of the universe are used, γ and R_{cut} remain similar while the deviance increases. When including the EGMF in the 4D simulations (model I), on the other hand, a strong increase in both γ and R_{cut} is caused, but the deviance is at the same level as it is in the 1D simulations. This indicates that the impact of the EGMF on the simulation results is higher than that of the source distribution. Specifically, neglecting the EGMF yields hard spectral indices ($\gamma < 1$), while including the EGMF yields softer spectral indices ($\gamma > 1$). Since most UHECR acceleration models predict $\gamma > 1$, this is an important finding. According to [149], this could be interpreted as an effect of magnetic horizons and magnetic suppression. Moreover, the data in Table 5.1 reveal that all models exhibit a high fraction of nitrogen (f_{N}) and a low fraction of iron (f_{Fe}), implying that nitrogen (as a representative of intermediate mass nuclei) predominates in the chemical composition of UHECRs at their sources.

Apart from the highly pronounced global minimum of the deviance D, there is only one distinct local (second) minimum at $\gamma \approx 2$. This was previously noted in [114] and appears to be a common feature regardless of the specific model. Using the parameter values of γ, R_{cut}, and f_α associated with the local (second) minimum of D results in a weaker agreement between the simulation outcomes and the experimental data. Table 5.2 lists these values alongside the corresponding values of D, which exceed the deviance D values listed in Table 5.1, indicating a weaker agreement between the simulation outcomes and the experimental data for the parameter values associated with the local (second) minimum of D.

While the simulation results corresponding to the second minimum of D are still in well agreement with the Pierre Auger Observatory data for the energy spectrum (see the values of D_J), the agreement deteriorates when comparing the results for the X_{max} distribution (see the values of $D_{X_{\mathrm{max}}}$).

[1] The fit procedure applied in [114] differs marginally from the one used here, but it can be anticipated that this has only a negligible impact on the outcomes.

Model	γ	$\log_{10}\left(\frac{R_{\mathrm{cut}}}{\mathrm{eV}}\right)$	$f_{\mathrm{H}}/\%$	$f_{\mathrm{He}}/\%$	$f_{\mathrm{N}}/\%$	$f_{\mathrm{Si}}/\%$	$f_{\mathrm{Fe}}/\%$	$D = D_J + D_{X_{\mathrm{max}}}$
I	$2.30^{+0.02}_{-0.02}$	$20.00^{+0.14}_{-0.08}$	$12.7^{+0.4}_{-3.3}$	$5.2^{+2.8}_{-5.2}$	$38.3^{+2.0}_{-1.7}$	$42.5^{+7.7}_{-2.1}$	$1.3^{+0.7}_{-1.3}$	$243.0 = 45.8 + 197.2$
II	$2.01^{+0.03}_{-0.03}$	$19.90^{+0.10}_{-0.09}$	$1.0^{+0.6}_{-1.0}$	$35.5^{+7.0}_{-1.3}$	$17.2^{+3.1}_{-17.2}$	$44.9^{+12.7}_{-3.1}$	$1.4^{+0.6}_{-1.4}$	$286.9 = 24.2 + 262.7$

Table 5.2: Similar to Tab. 5.1, but this time corresponding to the local (second) minimum instead of the global minimum of the deviance D for models I and II. Caption: cf. Tab. 2 in [2]. Table: from Tab. 2 in [2].

5.2 Dependence on the cosmological evolution of the sources

In the past, the EGMF was usually neglected when the effect of the cosmological evolution of the sources was investigated (see, for example, [394]). To address and close this gap, following the approach in [114], the author parameterized the emissivity of the sources with $\propto (1+z)^m$, where z represents the redshift of the sources and m is a source evolution parameter. In Table 5.3, the best-fit parameter values of γ and R_{cut} are listed considering model I and different source evolutions, showing the impact on the results for different source evolutions.

m	γ	$\log_{10}\left(\frac{R_{\mathrm{cut}}}{\mathrm{eV}}\right)$	$D_{\mathrm{min}} = D^{J}_{\mathrm{min}} + D^{X_{\mathrm{max}}}_{\mathrm{min}}$
3	$1.20^{+0.06}_{-0.07}$	$18.70^{+0.02}_{-0.02}$	$184.0 = 28.2 + 155.8$
0	$1.61^{+0.08}_{-0.07}$	$18.88^{+0.03}_{-0.07}$	$191.9 = 37.3 + 154.6$
-3	$1.78^{+0.07}_{-0.08}$	$18.77^{+0.03}_{-0.05}$	$199.0 = 41.2 + 157.8$
-6	$1.95^{+0.06}_{-0.10}$	$18.77^{+0.03}_{-0.04}$	$202.0 = 40.5 + 161.5$
-9	$2.05^{+0.08}_{-0.09}$	$18.78^{+0.02}_{-0.02}$	$203.4 = 42.2 + 161.2$

Table 5.3: To obtain the best-fit parameter values for γ and R_{cut} listed here, the deviance D was minimized. For different values of the source evolution parameter m, the minimum deviance D_{min} and its components D^{J}_{min} and $D^{X\mathrm{max}}_{\mathrm{min}}$ were calculated for model I. Caption: cf. Tab. 3 in [2]. Table: from Tab. 3 in [2].

Among the source evolution parameters considered, $m = 3$ shows the best agreement with the experimental data, while smaller m values decrease this agreement and increase the spectral index γ. Data compatibility with first-order Fermi acceleration of UHECRs or other acceleration mechanisms that produce emission spectra with a spectral index of about 2 can be achieved by assuming a negative source evolution with $m \approx -6$. If the EGMF is ignored, even more negative source evolutions are necessary for data compatibility with first-order Fermi acceleration (see [114, 394]).

6 Predictions for the target properties

The author simulated the propagation of UHECRs from their sources to the Earth, using the best-fit parameter values from Tab. 5.1. In this way, he generated simulation data about UHECRs arriving at the Earth, which can be compared to the experimental results of the Pierre Auger Observatory. In this chapter, the simulation outcomes and their agreement with experimental results are discussed, focusing on the energy spectrum and composition of the incoming UHECRs, their arrival direction distribution, and the cosmogenic neutrino flux.

6.1 Energy spectrum and composition

The energy spectrum and first and second moments of the $X_{\max}$ distribution, obtained by simulations for the best-fit parameter values of model I, are shown in Figure 6.1. For comparison, the corresponding data from the Pierre Auger Observatory are also shown. It is evident that the simulation data show good agreement with the experimental data from the Pierre Auger Observatory. In Fig. 6.1(a), the dashed curves highlight the contributions from detected nuclei, belonging to different intervals of the mass number A, to the energy spectrum. The dotted lines in Fig. 6.1(b) and (c) illustrate simulation results that one would obtain for scenarios where the detected UHECRs would consist exclusively of protons or iron nuclei for comparison. The experimental data with energies below the "ankle", which is at approximately 5 EeV, were excluded from the fit procedure described in section 4.2 due to their potential considerable galactic contribution. To indicate this in Fig. 6.1, the regions below 5 EeV are highlighted in gray. The reduced agreement of the experimental data and the fit curve in the gray

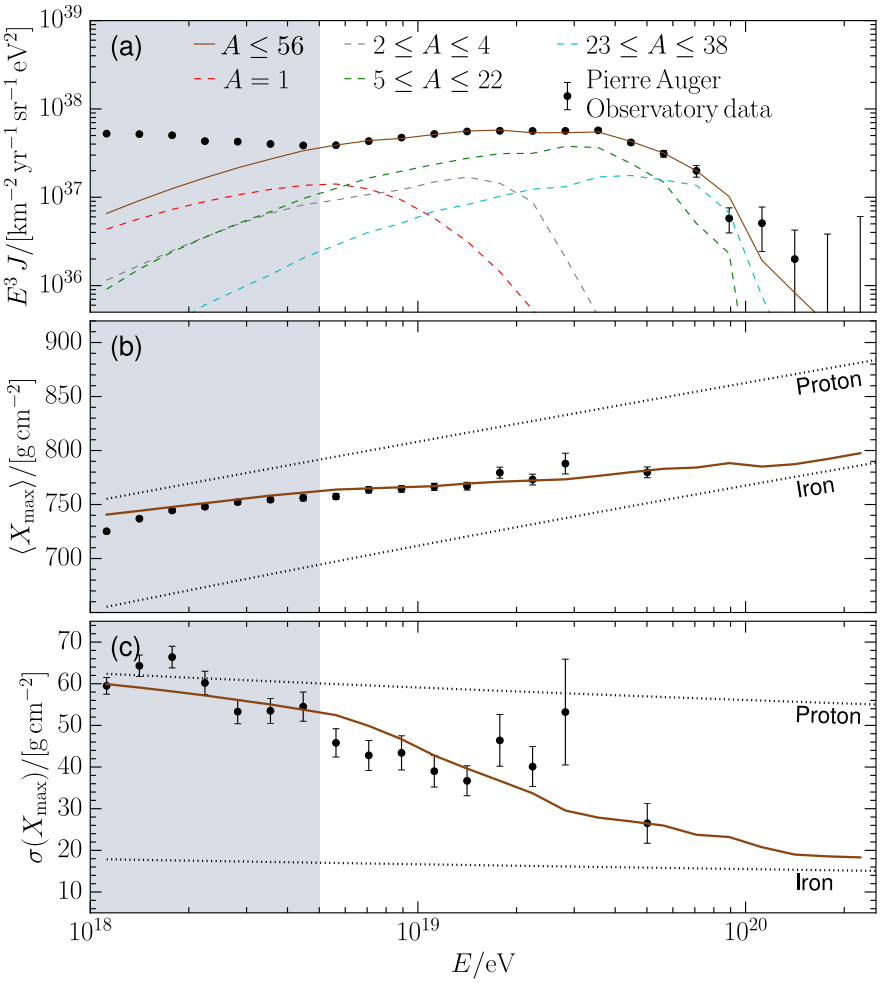

Figure 6.1: The authors' simulation results are presented as follows: (a) the energy spectrum $J(E)$, (b) the mean $\langle X_{\mathrm{max}}\rangle$, and (c) the standard deviation $\sigma(X_{\mathrm{max}})$ of the X_{max} distribution. These results, represented as brown solid curves, correspond to the best-fit parameter values for f_α, γ, and R_{cut} in model I (see Tab. 5.1) and exhibit good agreement with the experimental data from the Pierre Auger Observatory. The Pierre Auger Observatory data [274, 346], depicted with data points and error bars, is also shown for comparison. In (a), additional curves highlight the contributions to the energy spectrum from detected nuclei of different intervals of mass numbers A. The black dotted lines in (b) and (c) illustrate the results that one would obtain if only protons (upper lines) or iron nuclei (lower lines) hit the atmosphere and initiate EASs. Experimental data with energies below the "ankle" at approximately 5 EeV (highlighted in gray regions) were excluded from the fit procedure described in section 4.2, due to their potential considerable galactic contribution. Caption: cf. Fig. 1 in [2]. Figure: adapted from Fig. 1 in [2].

region in Fig. 6.1(a) suggests that there is indeed a considerable galactic contribution. This contribution seems to increase with decreasing energy. If one is interested in UHECRs at energies below the "ankle", one should therefore model an additional galactic contribution in the simulations. The energy range below the "ankle" has been studied extensively in various other works to which the interested reader is referred.

6.2 Anisotropy in the arrival directions

For simulated UHECRs arriving at Earth with energies $E > 8\,\mathrm{EeV}$, $E > 10\,\mathrm{EeV}$, or $E > 15\,\mathrm{EeV}$, the angular power spectrum of the arrival directions up to order $l_{\mathrm{max}} = 32$ is shown in Fig. 6.2. Remarkably, across all three energy ranges, the results indicate a statistically significant ($s > 5\sigma$) dipolar anisotropy. In contrast, on smaller solid angle scales, the arrival directions' distribution is always consistent with an isotropic directional distribution. The significant dipolar anisotropy, without the presence of higher-order anisotropies for arrival energies E greater than 8 EeV (see Fig. 6.2(a)), shows excellent agreement with the data of the Pierre Auger Observatory. The Pierre Auger Collaboration reported in 2017 the observation of a significant ($s > 5\sigma$) dipolar anisotropy in the arrival directions of UHECRs in [119]. Isotropy for the higher-order multipole moments was reported in [127].

The results of this work for arrival energies $E > 10\,\mathrm{EeV}$ (see Fig. 6.2(b)) are well in line with [130], which mentions indications of a dipolar anisotropy for the same energy range. While this finding is not statistically significant at the 5σ level, the simulation results suggest that the dipolar anisotropy in the experimental data is likely to become significant also in this energy range once sufficient data are available. According to [130], higher-order contributions to the angular power spectrum up to order $l = 20$ were taken into account and found to be compatible with isotropy. This shows consistency with the simulations again, leading to the prediction that no significant anisotropy will be found for even larger l values in upcoming experiments in the next years. The predictions for arrival energies $E > 15\,\mathrm{EeV}$ (see Fig. 6.2(c)) are anticipated by the author to get confirmed by future experimental research. Currently, there seem to be no relevant experimental

studies that examine the angular power spectrum of the arrival directions of UHECRs within this energy range.

For energies E exceeding 8 EeV, 10 EeV, and 15 EeV, the respective values of $C_1(E)$ are 3.74×10^{-3}, 6.28×10^{-3}, and 1.34×10^{-2}. The related dipole amplitudes, calculated as $\frac{3}{2\sqrt{\pi}}\sqrt{C_1(E)}$, are approximately 5.2×10^{-2}, 6.7×10^{-2}, and 9.8×10^{-2}, respectively. It is remarkable that the dipole amplitudes for energies E above 8 EeV and 10 EeV are close to the values determined through experimental research [119, 130]. The values of $C_4(E)$ are striking across all examined energy ranges; however, they are unlikely to be measured with a significance level of $s > 5\sigma$ in the coming years using the current UHECR observatories. It should be noted that the non-vanishing size of the observer can cause an artificial deflection that diminishes the observed multipole moments [115]. This reduction becomes stronger with increasing l; it can be disregarded for small l, but results for large l should be considered as lower limits. Nevertheless, up to $l_{\max} = 32$, this effect remains sufficiently small, ensuring that it does not qualitatively alter any results presented in this work.

A remarkable feature of the simulation results presented here is their good agreement with the energy spectrum, mass spectrum, and angular power spectrum of the available experimental data. Previous research has often concentrated on either the energy spectrum and mass spectrum or the anisotropies in the arrival directions of UHECRs. However, these studies have not provided a coherent explanation that accounts for all three observables simultaneously [104, 151, 152, 395]. The small number of exceptions did not use an EGMF with a realistic structure or had difficulties in simultaneously reproducing the experimental results for all observables. One example is the published research by [153], in which a too strong anisotropy was reported in the arrival directions. Unlike these previous studies, the author's research is grounded in an astrophysical scenario that yields results consistent with the available experimental UHECR data for the energy spectrum, mass spectrum, and anisotropies. Additionally, it enables predictions for energy ranges and contributions to the angular power spectrum where sufficient experimental data are still missing.

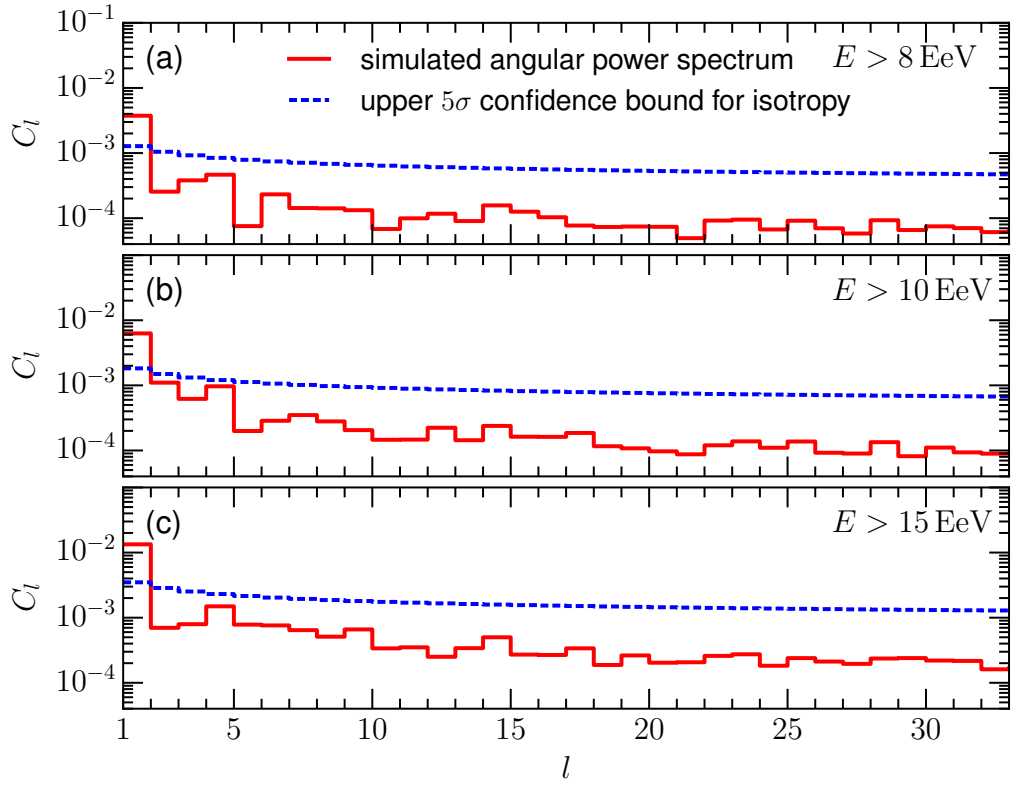

Figure 6.2: The angular power spectrum $\{C_l(E)\}$ for the arrival directions of the simulated UHECRs arriving at Earth with energies (a) $E > 8\,\mathrm{EeV}$, (b) $E > 10\,\mathrm{EeV}$, and (c) $E > 15\,\mathrm{EeV}$ is shown together with the corresponding upper 5σ confidence bounds for isotropy. It is evident that a significant dipolar anisotropy exists across all energy intervals (indicated by the values of $C_1(E)$). Meanwhile, the higher-order $C_l(E)$ results are consistent with isotropy. Caption: cf. Fig. 1 in [3]. Figure: from Fig. 1 in [3].

6.3 Flux of cosmogenic neutrinos

The author's predictions for the energy-dependent flux of high-energy cosmogenic neutrinos of all flavors reaching Earth are illustrated in Figure 6.3. In this figure, two corresponding curves are shown: one representing simulations that took the EGMF into account and one representing simulations that neglected the EGMF. Additionally, it replicates results from a previous one-dimensional (1D) simulation by [141] which were based on a "combined fit" model without considering the EGMF. The figure also includes the differential upper limits for the cosmogenic neutrino flux that have been obtained from data collected by the Pierre Auger Observatory [136] and the IceCube Neutrino Observatory [137]. By assuming equal ratios of neutrino flavors, the single-flavor findings from [141] and the single-flavor upper limit from [136] have been scaled to all-flavor data by multiplying by three. Additionally, the figure includes the predicted 3-year sensitivities of the planned and probable future neutrino observatories ARA37 [396], ARIANNA [397] ("optimal wind" sensitivity), GRAND 200k (Mauricio Bustamante, private communication), and Trinity [398].

The predicted fluxes of cosmogenic neutrinos are several orders of magnitude smaller than the upper limits shown and are therefore in agreement with the measurements made by the observatories. It is not surprising that no high-energy cosmogenic neutrinos have been detected to date, since the predicted neutrino fluxes are much lower than the upper limits. The results obtained for the case of an absence of an EGMF ("Without EGMF" in Fig. 6.3) closely match those of the one-dimensional simulation. However, the curve for the case where an EGMF is present ("With EGMF" in Fig. 6.3) clearly deviates from the curve for the case without an EGMF. For predicted cosmogenic neutrino fluxes, both curves begin at roughly the same values at a neutrino energy of $E = 10^{17}\,\mathrm{eV}$ and decrease as E increases. The curve corresponding to the presence of an EGMF runs above the other curve everywhere, and the enhancement factor increases with increasing E. At $E = 10^{19}\,\mathrm{eV}$, there is a roughly four-order-of-magnitude difference in the neutrino fluxes. This reveals that, via the charged UHECRs, the EGMF has a considerable influence on the high-energy cosmogenic neutrino flux. One can also see that the predicted cosmogenic neutrino fluxes are clearly

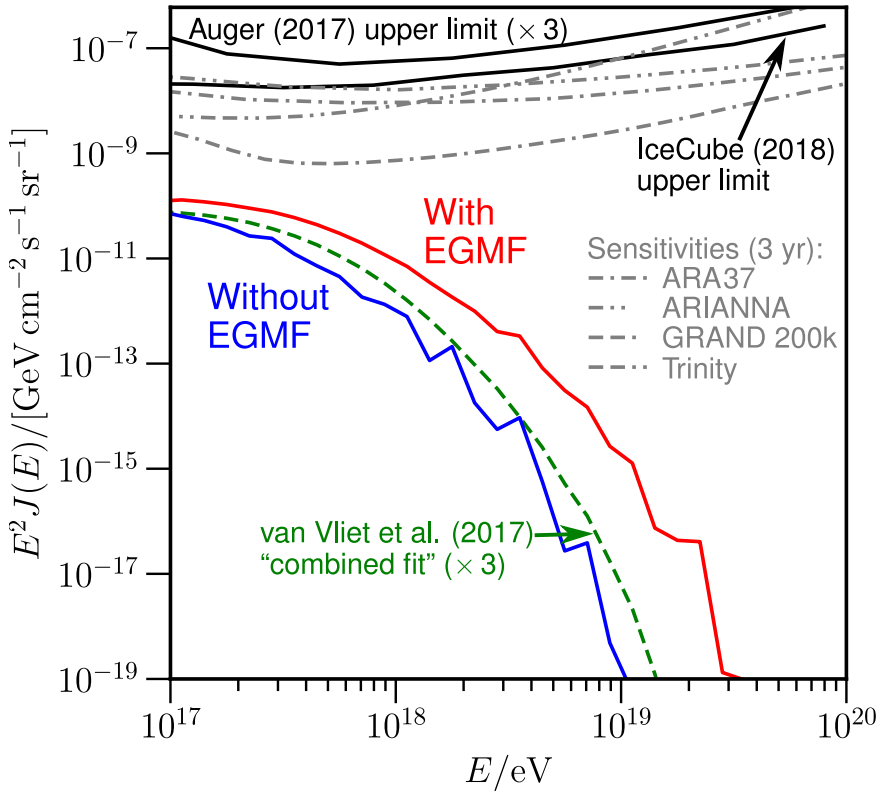

Figure 6.3: The author's predictions for the all-flavor flux $J(E)$ of high-energy cosmogenic neutrinos reaching Earth are shown as a function of neutrino energy E, distinguishing between scenarios that include (red) and exclude (blue) the extragalactic magnetic field (EGMF). The one-dimensional simulation results (green) from [141][1], which did not account for the EGMF, are shown alongside the differential upper limits (black) for the neutrino flux obtained from both the Pierre Auger Observatory [136] and the IceCube Neutrino Observatory [137] as references. Additionally, the projected sensitivities of ARA37 [396], ARIANNA [397] (with "optimal wind" sensitivity), GRAND 200k (Mauricio Bustamante, private communication), and Trinity [398] are depicted in gray. Caption: cf. Fig. 1 in [4]. Figure: from Fig. 1 in [4].

below the 3-year sensitivities anticipated for the considered future neutrino observatories.

The observation that the EGMF increases the neutrino flux can be partially explained by the fact that UHECRs are deflected in a magnetic field, resulting in longer path lengths and therefore more interactions with the photon background. In addition, these deflections reduce the UHECR horizon, which is the region encompassing all sources from which UHECRs can reach the Earth. When the EGMF reduces this horizon and the number of enclosed sources, these sources must be brighter than in the absence of an EGMF to match the UHECR flux observed by the Pierre Auger Observatory. Consequently, the EGMF alters the derived source properties (see chapter 5), leading to a greater UHECR emission by sources both within and outside the UHECR horizon. Since neutrinos can reach the Earth from regions beyond the UHECR horizon, the increased luminosity of UHECR sources increases the flux of cosmogenic neutrinos arriving at Earth.

It is important to note that this result does not conflict with the propagation theorem, which asserts that "For a uniform distribution of identical sources with separation much less than the characteristic propagation lengths, the diffuse spectrum of UHECRs has a universal (standard) form, independent of the mode of propagation." [399]. This theorem does not apply to the present work for two key reasons: First, the sources in the present simulations are not uniformly distributed in space but instead follow a structured mass distribution. Second, the low source density used in the simulations (approximately $10^{-4}\,\mathrm{Mpc}^{-3}$) corresponds in a system with uniformly distributed sources to a typical source separation of about 20 Mpc. According to [399], for the propagation theorem to be applicable, a typical source separation of 3 Mpc or less, corresponding to a source density of around $4 \cdot 10^{-2}\,\mathrm{Mpc}^{-3}$ or higher, would be required.

[1] The data for energies exceeding 10^{18}eV are not presented in [141], but were obtained through a private communication with Arjen van Vliet.

7 Summary and outlook

In the previous chapters, the propagation of UHECRs was studied to obtain information about their sources and the flux of high-energy cosmogenic neutrinos, originating from interactions of UHECRs with cosmic background photons, at the Earth. For this purpose, elaborate computer simulations of the propagation of UHECRs from their assumed sources through the universe to the Earth were performed and a comparison with data from large-scale cosmic-ray experiments was made. The performed simulations took into account all three spatial degrees of freedom, the cosmological time-evolution of the universe, a discrete distribution of the sources that follows the local large-scale mass distribution of the universe, different energy spectra and chemical compositions of the UHECRs at their sources, interactions of UHECRs with cosmic background photons resulting, e.g., in the generation of high-energy cosmogenic neutrinos, the propagation of secondary particles like the cosmogenic neutrinos, and realistic and structured models of the extragalactic and, where relevant, galactic magnetic fields.

On this basis, it was studied (i) for which energy spectrum and chemical composition of the UHECRs at their sources the energy spectrum and chemical composition of the simulated UHECRs arriving at the Earth are in the best possible agreement with the corresponding data measured by the Pierre Auger Observatory, (ii) how the source parameters describing the initial energy spectrum and chemical composition reconstructed in this way are affected by the EGMF, (iii) how the directions of the UHECRs arriving at the Earth are distributed, and (iv) how the flux of cosmogenic neutrinos with energies $E \geq 10^{17}\,\mathrm{eV}$ arriving at the Earth depends on their arrival energy and – via the propagation of the preceding UHECRs – on the EGMF.

The results of the simulations were found to be in very good agreement with the available UHECR data collected by the Pierre Auger Observa-

tory. They showed that the source parameters for the energy spectrum and chemical composition of the UHECRs reconstructed from the Pierre Auger Observatory data depend strongly on the EGMF and the source evolution [1, 2]. Assuming a nonvanishing EGMF resulted in a better agreement of the simulated UHECRs arriving at the Earth and the Pierre Auger Observatory data than neglecting the EGMF. This shows that in simulation studies on the propagation of UHECRs the EGMF should be taken into account. In the case with an EGMF, soft spectral indices (> 1) were found, whereas without an EGMF the spectral indices were much harder. This behavior is qualitatively consistent with predictions of [149]. Moreover, for both situations the Pierre Auger Observatory data suggested that the chemical composition of the UHECRs at their sources is dominated by intermediate-mass nuclei, which is in accordance with previous one-dimensional simulations [114]. The source parameters deduced from the local second minimum of the deviance are well in line with a spectral index of about 2, but they are disfavored by the Pierre Auger Observatory data. In the presence of an EGMF, a positive source evolution parameter shows the best agreement with the experimental data. For decreasing values of the source evolution parameter, the agreement becomes worse while the spectral index becomes larger. In case of a negative source evolution parameter of ≈ -6 the spectral index is ≈ 2 and thus similar to what is predicted for first-order Fermi acceleration of UHECRs. In the absence of an EGMF, even more negative source evolutions would be required to see compatibility of the data with first-order Fermi acceleration [114, 394].

Regarding the distribution of the arrival directions of the UHECRs, a pronounced dipolar anisotropy and rather weak higher-order contributions to the angular power spectrum were found [3]. The dipolar anisotropy is energy-dependent, but clearly pronounced for all arrival-energy ranges the author considered ($E > 8\,\mathrm{EeV}$, $E > 10\,\mathrm{EeV}$, and $E > 15\,\mathrm{EeV}$). These findings agree well with the observation of a significant dipolar anisotropy [119], and no significant departure from isotropy for the higher-order multipole moments [127], for UHECRs with arrival energies $E > 8\,\mathrm{EeV}$ by the Pierre Auger Observatory. They are also well in line with indications of a dipolar anisotropy, and higher-order contributions ($2 \leq l \leq 20$) to the angular power spectrum that are compatible with isotropy, reported for $E > 10\,\mathrm{EeV}$

in a combined study of the Pierre Auger Collaboration and the Telescope Array Collaboration [130]. For higher energies and higher-order multipole moments, there seem to be no experimental findings corresponding to the results of the present work, which therefore constitute an important prediction that is likely to get confirmed as soon as sufficient experimental data are available.

The simulations yielded also predictions for the flux of high-energy cosmogenic neutrinos at the Earth [4]. These findings are consistent with upper limits for the neutrino flux obtained from the Pierre Auger Observatory and IceCube Neutrino Observatory. Corresponding simulations where the EGMF was neglected led to strongly different predictions with up to four orders of magnitude lower neutrino fluxes that are in line with results from a previous one-dimensional simulation. This shows that the EGMF has a major influence also on the neutrino flux and that it typically must not be neglected in theoretical studies on the generation and propagation of cosmogenic neutrinos. Since considering an EGMF leads to higher cosmogenic neutrino fluxes, predictions from previous simulations that neglected the EGMF can be considered only as lower bounds for the cosmogenic neutrino flux.

With the obtained results [1–4], this work significantly extends the knowledge about the sources and propagation of UHECRs as well as the associated flux of cosmogenic neutrinos. The excellent agreement of the simulation results and related experimental data covers the energy spectrum, chemical composition, and anisotropy in the arrival directions of the detected UHECRs. This shows that the information and assumptions underlying the simulations constitute a highly realistic astrophysical scenario [2] that consistently describes the properties of the sources of UHECRs, their emission at the sources, and the propagation to the Earth. This gives important hints on the still unknown identity of the real sources of UHECRs and the properties of these sources. Furthermore, with its outstanding features, this astrophysical scenario is a very useful basis for future simulation studies on UHECRs. One could use simulations based on this scenario, e.g., to predict the flux of photons that originate from interactions of UHECRs with the extragalactic background light. These photons are interesting, since they provide additional information about the sources of UHECRs, but up to now

it was not yet possible to detect photons with the particularly attractive energies $E > 10^{18}\,\mathrm{eV}$. Therefore, predictions for the flux of such photons would be very useful. These predictions could be compared with the upper photon flux limits determined by the Pierre Auger Observatory [400] and would help to design future gamma-ray detectors [401, 402].

The results of this work are important also for the design of future neutrino observatories such as ARA [403], ARIANNA [404], GRAND [405], IceCube-Gen2 [406], POEMMA [407], and Trinity [398] that are currently in the planning phase. With the predictions of this work for the cosmogenic neutrino flux, one can assess which detector volume and observation time are necessary to detect high-energy cosmogenic neutrinos in the near future. The observation of such neutrinos is an important goal in current astrophysics, since it would push multimessenger astronomy [408] from below $10^{15}\,\mathrm{eV}$ [409] to entirely new energy scales.

Bibliography

[1] D. Wittkowski, T. Winchen, and K.-H. Kampert, "Influence of the extragalactic background light and magnetic field on the energy spectrum and chemical composition of ultra-high-energy cosmic rays," Internal note of the Pierre Auger Collaboration **GAP2017-001** (2017).

[2] D. Wittkowski for the Pierre Auger Collaboration, "Reconstructed properties of the sources of UHECR and their dependence on the extragalactic magnetic field," in *Proceedings of the 35th International Cosmic Ray Conference (ICRC 2017)*, Proceedings of Science (SISSA, Trieste, 2018) p. 563.

[3] D. Wittkowski and K.-H. Kampert, "On the anisotropy in the arrival directions of ultra-high-energy cosmic rays," Astrophysical Journal Letters **854**, L3 (2018).

[4] D. Wittkowski and K.-H. Kampert, "On the flux of high-energy cosmogenic neutrinos and the influence of the extragalactic magnetic field," Monthly Notices of the Royal Astronomical Society Letters **488**, L119–L122 (2019).

[5] V. F. Hess, "Über Beobachtungen der durchdringenden Strahlung bei sieben Ballonfahrten," Physikalische Zeitschrift **13**, 1084–1091 (1912).

[6] V. F. Hess, "Mitteilungen aus dem Institut für Radiumforschung XXX. Beobachtungen der durchdringenden Strahlung bei sieben Freiballonfahrten," Sitzungsberichte der mathematisch-naturwissenschaftlichen Classe der kaiserlichen Akademie der Wissenschaften **121**, 349–350 (1912).

[7] M. Friedlander, "A century of cosmic rays," Nature **483**, 400–401 (2012).

[8] T. Wulf, "Über die in der Atmosphäre vorhandene Strahlung von hoher Durchdringungsfähigkeit," Physikalische Zeitschrift **10**, 152–157 (1909).

[9] T. Wulf, "Beobachtungen über die Strahlung hoher Durchdringungsfähigkeit auf dem Eiffelturm," Physikalische Zeitschrift **11**, 811–813 (1910).

[10] A. Gockel, "Luftelektrische Beobachtungen bei einer Ballonfahrt," Physikalische Zeitschrift **11**, 280–282 (1910).

[11] A. Gockel, "Messungen der durchdringenden Strahlung bei Ballonfahrten," Physikalische Zeitschrift **12**, 595–597 (1911).

[12] J. Lacki, "Albert Gockel, a pioneer in atmospheric electricity and cosmic radiation," Astroparticle Physics **53**, 27–32 (2014).

[13] R. G. A. Fricke and K. Schlegel, "100th anniversary of the discovery of cosmic radiation: The role of Günther and Tegetmeyer in the development of the necessary instrumentation," History of Geo- and Space Sciences **3**, 151–158 (2012).

[14] D. Fick and D. Hoffmann, "Werner Kolhörster (1887-1945): The German pioneer of cosmic ray physics," Astroparticle Physics **53**, 50–54 (2014).

[15] W. Kolhörster, "Messungen der durchdringenden Strahlung im Freiballon in größeren Höhen," Physikalische Zeitschrift **14**, 1153–1156 (1913).

[16] W. Kolhörster, "Messungen der durchdringenden Strahlungen bis in Höhen von 9300 m," Verhandlungen der deutschen Physikalischen Gesellschaft **16**, 719–721 (1914).

[17] R. A. Millikan and I. S. Bowen, "High frequency rays of cosmic origin I. Sounding balloon observations at extreme altitudes," Physical Review **27**, 353–361 (1926).

[18] M. Walter and A. W. Wolfendale, "Early history of cosmic particle physics," European Physical Journal H **37**, 323–358 (2012).

[19] A. Gockel and T. Wulf, "Beobachtungen über die Radioaktivität der Atmosphäre im Hochgebirge," Physikalische Zeitschrift **9**, 907–911 (1908).

[20] R. A. Millikan and G. H. Cameron, "The origin of the cosmic rays," Physical Review **32**, 533–557 (1928).

[21] J. R. Hörandel, "Early cosmic-ray work published in German," AIP Conference Proceedings **1516**, 52–60 (2013).

[22] E. Steinke, "Neue Untersuchungen über die durchdringende Hesssche Strahlung," Zeitschrift für Physik **48**, 647–689 (1928).

[23] E. Steinke, "Wasserversenkmessungen der durchdringenden Hessschen Strahlung," Zeitschrift für Physik **58**, 183–193 (1929).

[24] E. Regener, "Über die durchdringendste Komponente der Ultrastrahlung (Hessschen Strahlung)," Naturwissenschaften **19**, 177–179 (1931).

[25] L. Myssowsky and L. Tuwim, "Versuche über die Absorption der Höhenstrahlung im Wasser," Zeitschrift für Physik **35**, 299–303 (1926).

[26] W. Bothe and W. Kolhörster, "Das Wesen der Höhenstrahlung," Zeitschrift für Physik **56**, 751–777 (1929).

[27] G. Molière, "Die räumliche und Winkelverteilung der Teilchen in den Luftschauern der Höhenstrahlung," Naturwissenschaften **30**, 87–89 (1942).

[28] P. Kunze, "Untersuchung der Ultrastrahlung in der Wilsonkammer," Zeitschrift für Physik **83**, 1–18 (1933).

[29] E. Regener, "Der Energiestrom der Ultrastrahlung," Zeitschrift für Physik **80**, 666–669 (1933).

[30] G. Pfotzer, "Dreifachkoinzidenzen der Ultrastrahlung aus vertikaler Richtung in der Stratosphäre," Zeitschrift für Physik **102**, 41–58 (1936).

[31] A. Ehmert, "Die Absorptionskurve der harten Komponente der kosmischen Ultrastrahlung," Zeitschrift für Physik **106**, 751–773 (1937).

[32] D. Skobelzyn, "Über eine neue Art sehr schneller β-Strahlen," Zeitschrift für Physik **54**, 686–702 (1929).

[33] W. Bothe, "Zur Vereinfachung von Koinzidenzzählungen," Zeitschrift für Physik **59**, 1–5 (1930).

[34] L. Bonolis, "Walther Bothe and Bruno Rossi: The birth and development of coincidence methods in cosmic-ray physics," American Journal of Physics **79**, 1133–1150 (2011).

[35] C. A. Ziegler, "Technology and the process of scientific discovery: The case of cosmic rays," Technology and Culture **30**, 939–963 (1989).

[36] J. Nishimura, "Scientific ballooning in the 20th century; a historical perspective," Advances in Space Research **30**, 1071–1085 (2002).

[37] W. V. Jones, "Evolution of scientific ballooning and its impact on astrophysics research," Advances in Space Research **53**, 1405–1414 (2014).

[38] I. S. Bowen and R. A. Millikan, "Cosmic-ray intensities in the stratosphere," Physical Review **43**, 695–700 (1933).

[39] L. P. Harrison, "The exploration of the free atmosphere," Scientific Monthly **39**, 221–234 (1934).

[40] A. H. Compton, "Cosmic rays," Nature **135**, 695–698 (1935).

[41] P. Carlson and A. A. Watson, "Erich Regener and the ionisation maximum of the atmosphere," History of Geo- and Space Sciences **5**, 175–182 (2014).

[42] E. Regener, "Intensity of cosmic radiation in the high atmosphere," Nature **130**, 364–364 (1932).

[43] E. Regener and G. Pfotzer, "Messungen der Ultrastrahlung in der oberen Atmosphäre mit dem Zählrohr," Physikalische Zeitschrift **35**, 779–784 (1934).

[44] M. Pagitz, "The future of scientific ballooning," Philosophical Transactions of the Royal Society A: Mathematical, Physical and Engineering Sciences **365**, 3003–3017 (2007).

[45] N. Yajima, N. Izutsu, T. Imamura, and T. Abe, *Scientific Ballooning: Technology and applications of exploration balloons floating in the stratosphere and the atmospheres of other planets*, Vol. 112 (Springer Science & Business Media, New York, 2009).

[46] A. Piccard and M. Cosyns, "Étude du rayonnement cosmique en grande altitude," Comptes rendus de l'Académie des sciences **195**, 604–606 (1932).

[47] A. Piccard, E. Stahel, and P. Kipfer, "Messung der Ultrastrahlung in 16000 m Höhe," Naturwissenschaften **20**, 592–593 (1932).

[48] G. Pfotzer, "History of the use of balloons in scientific experiments," Space Science Reviews **13**, 199–242 (1972).

[49] P. Auger, P. Ehrenfest, R. Maze, J. Daudin, and R. A. Fréon, "Extensive cosmic-ray showers," Reviews of Modern Physics **11**, 288–291 (1939).

[50] C. D. Anderson, "The positive electron," Physical Review **43**, 491–494 (1933).

[51] S. H. Neddermeyer and C. D. Anderson, "Note on the nature of cosmic-ray particles," Physical Review **51**, 884–886 (1937).

[52] C. M. G. Lattes, H. Muirhead, G. P. S. Occhialini, and C. F. Powell, "Processes involving charged mesons," Nature **159**, 694–697 (1947).

[53] C. M. G. Lattes, G. P. S. Occhialini, and C. F. Powell, "A determination of the ratio of the masses of π- and μ-mesons by the method of grain-counting," Proceedings of the Physical Society **61**, 173–183 (1948).

[54] G. D. Rochester and C. C. Butler, "Evidence for the existence of new unstable elementary particles," Nature **160**, 855–857 (1947).

[55] O. Chamberlain, W. W. Chupp, G. Goldhaber, E. Segre, C. Wiegand, *et al.*, "On the observation of an antiproton star in emulsion exposed at the Bevatron," Il Nuovo Cimento **3**, 447–467 (1956).

[56] H. A. Grunder, W. D. Hartsough, and E. J. Lofgren, "Acceleration of heavy ions at the Bevatron," Science **174**, 1128–1129 (1971).

[57] J. Linsley, "Evidence for a primary cosmic-ray particle with energy 10^{20} eV," Physical Review Letters **10**, 146–148 (1963).

[58] R. P. Hudson and J. R. Pierce, "The 1978 Nobel prize in physics," Science **202**, 960–963 (1978).

[59] A. A. Penzias, "A runaway success," Nature **467**, S4–S4 (2010).

[60] A. A. Penzias and R. W. Wilson, "A measurement of excess antenna temperature at 4080 Mc/s." Astrophysical Journal **142**, 419–421 (1965).

[61] R. Burmester, *Wissenschaft aus erster Hand / Science at First Hand: 65 Jahre Lindauer Nobelpreisträgertagungen / 65 years of Lindau Nobel Laureate Meetings*, 2nd ed. (Deutsches Museum Bonn, Bonn, 2015) pp. 1–223.

[62] A. C. Beck and H. T. Friis, "Horn antenna system," U. S. patent no. 2416675, filed November 26, 1941, granted March 4, 1947 (1947).

[63] A. B. Crawford, D. C. Hogg, and L. E. Hunt, "A horn-reflector antenna for space communication," Bell System Technical Journal **40**, 1095–1116 (1961).

[64] W. C. Jakes, "Participation of Bell Telephone Laboratories in project Echo and experimental results," Bell System Technical Journal **40**, 975–1028 (1961).

[65] W. K. Victor and R. Stevens, "The role of the Jet Propulsion Laboratory in project Echo," IRE Transactions on Space Electronics and Telemetry **SET-7**, 20–28 (1961).

[66] K. Greisen, "End to the cosmic-ray spectrum?" Physical Review Letters **16**, 748–750 (1966).

[67] G. T. Zatsepin and V. A. Kuz'min, "Upper limit of the spectrum of cosmic rays," Journal of Experimental and Theoretical Physics Letters **4**, 78–80 (1966).

[68] D. J. Bird, S. C. Corbato, H. Y. Dai, J. W. Elbert, K. D. Green, *et al.*, "Detection of a cosmic ray with measured energy well beyond the expected spectral cutoff due to cosmic microwave radiation," Astrophysical Journal **441**, 144–150 (1995).

[69] R. G. Brownlee, A. J. Fisher, L. Goorevich, P. C. Kohn, C. B. A. McCusker, *et al.*, "Design of an array to record air showers of energy up to 10^{21} eV," Canadian Journal of Physics **46**, 259–262 (1968).

[70] M. M. Winn, J. Ulrichs, L. S. Peak, C. B. A. McCusker, and L. Horton, "The cosmic-ray energy spectrum above 10^{17} eV," Journal of Physics G: Nuclear Physics **12**, 653–674 (1986).

[71] M. A. Lawrence, R. J. O. Reid, and A. A. Watson, "The cosmic ray energy spectrum above 4×10^{17} eV as measured by the Haverah Park array," Journal of Physics G: Nuclear and Particle Physics **17**, 733–757 (1991).

[72] M. Takeda, N. Sakaki, K. Honda, M. Chikawa, M. Fukushima, *et al.*, "Energy determination in the Akeno Giant Air Shower Array experiment," Astroparticle Physics **19**, 447–462 (2003).

[73] R. Aloisio, "Acceleration and propagation of ultra-high energy cosmic rays," Progress of Theoretical and Experimental Physics **2017**, 12A102 (2017).

[74] J. Abraham *et al.* (Pierre Auger Collaboration), "Upper limit on the cosmic-ray photon fraction at EeV energies from the Pierre Auger Observatory," Astroparticle Physics **31**, 399–406 (2009).

[75] T. Abu-Zayyad *et al.* (Telescope Array Collaboration), "Upper limit on the flux of photons with energies above 10^{19} eV using the Telescope Array surface detector," Physical Review D **88**, 112005 (2013).

[76] A. Aab *et al.* (Pierre Auger Collaboration), "Search for photons with energies above 10^{18} eV using the hybrid detector of the Pierre Auger

Observatory," Journal of Cosmology and Astroparticle Physics **2017, 04**, 009 (2017).

[77] A. Aab *et al.* (Pierre Auger Collaboration), "Erratum: Search for photons with energies above 10^{18} eV using the hybrid detector of the Pierre Auger Observatory," Journal of Cosmology and Astroparticle Physics **2020, 09**, E02 (2020).

[78] A. Abdul Halim *et al.* (Pierre Auger Collaboration), "Search for photons above 10^{18} eV by simultaneously measuring the atmospheric depth and the muon content of air showers at the Pierre Auger Observatory," arXiv:2406.07439 (2024).

[79] P. Abreu *et al.* (Pierre Auger Collaboration), "Ultrahigh energy neutrinos at the Pierre Auger Observatory," Advances in High Energy Physics **2013**, 708680 (2013).

[80] A. Aab *et al.* (Pierre Auger Collaboration), "Improved limit to the diffuse flux of ultrahigh energy neutrinos from the Pierre Auger Observatory," Physical Review D **91**, 092008 (2015).

[81] M. Nagano and A. A. Watson, "Observations and implications of the ultrahigh-energy cosmic rays," Reviews of Modern Physics **72**, 689–732 (2000).

[82] A. Barrau, "Primordial black holes as a source of extremely high energy cosmic rays," Astroparticle Physics **12**, 269–275 (2000).

[83] R. Hnatyk and V. Voitsekhovskyi, "Extremely high energy ($E > 10^{20}$ eV) cosmic rays: Potential sources," Kinematics and Physics of Celestial Bodies **36**, 129–139 (2020).

[84] T. Abu-Zayyad *et al.* (Telescope Array Collaboration), "The surface detector array of the Telescope Array experiment," Nuclear Instruments and Methods in Physics Research Section A **689**, 87–97 (2012).

[85] A. Aab *et al.* (Pierre Auger Collaboration), "The Pierre Auger cosmic ray Observatory," Nuclear Instruments and Methods in Physics Research Section A **798**, 172–213 (2015).

[86] E. Zas for the Pierre Auger Collaboration, "Status and first results of the largest UHECR observatory," Czechoslovak Journal of Physics **56**, A231–A240 (2006).

[87] J. Abraham *et al.* (Pierre Auger Collaboration), "The fluorescence detector of the Pierre Auger Observatory," Nuclear Instruments and Methods in Physics Research Section A **620**, 227–251 (2010).

[88] I. Allekotte, A. F. Barbosa, P. Bauleo, C. Bonifazi, B. Civit, *et al.*, "The surface detector system of the Pierre Auger Observatory," Nuclear Instruments and Methods in Physics Research Section A **586**, 409–420 (2008).

[89] A. N. Bunner, "High-energy cosmic rays," Sky and Telescope **34**, 204 (1967).

[90] A. N. Bunner, *Cosmic ray detection by atmospheric fluorescence*, Ph.D. thesis, Cornell University, Ithaca, New York (1967).

[91] G. Tanahashi, "Early air fluorescence work Cornell and Japan," AIP Conference Proceedings **433**, 54–64 (1998).

[92] T. Hara, F. Ishikawa, S. Kawaguchi, Y. Miura, M. Nagano, *et al.*, "Detection of the atmospheric scintillation light from air showers," High Energy Interactions, Extensive Air Showers. Proceedings of the 11th International Conference on Cosmic Rays, Budapest, 25 August - 4 September, 1969. Acta Physica Academiae Scientiarum Hungaricae **Supplement to Vol. 29.** Edited by A. Somogyi, 369–376 (1970).

[93] H. E. Bergeson, J. C. Boone, and G. L. Cassiday, "The Fly's Eye. A novel technique for sensing extensive air showers," in *Proceedings from the 14th international cosmic ray conference (ICRC), Munich*, Vol. 8 (1975) pp. 3059–3063.

[94] R. M. Baltrusaitis, R. Cady, G. Cassiday, R. Cooperv, J. W. Elbert, *et al.*, "The Utah Fly's eye detector," Nuclear Instruments and Methods in Physics Research Section A **240**, 410–428 (1985).

[95] J. N. Matthews, C. C. H. Jui, and High Resolution Fly's Eye Collaboration, "First results from the High Resolution Fly's Eye experiment," Nuclear Physics B - Proceedings Supplements **87**, 411–413 (2000).

[96] H. E. Bergeson, G. L. Cassiday, T.-W. Chiu, D. A. Cooper, J. W. Elbert, *et al.*, "Measurement of light emission from remote cosmic-ray air showers," Physical Review Letters **39**, 847–849 (1977).

[97] J. N. Matthews, "Observing cosmic rays with the High Resolution Fly's Eye (HiRes) detector," Acta Physica Polonica B **35**, 1863–1876 (2004).

[98] N. A. Porter, T. E. Cranshaw, J. F. De Beer, A. G. Parham, and A. C. Sherwood, "Observations on extensive air showers VII. The lateral distribution of energy in the electron-photon component," Philosophical Magazine: A Journal of Theoretical Experimental and Applied Physics **3**, 826–830 (1958).

[99] A. A. Watson, "The discovery of Cherenkov radiation and its use in the detection of extensive air showers," Nuclear Physics B - Proceedings Supplements **212**, 13–19 (2011).

[100] R. M. Tennent, "The Haverah Park extensive air shower array," Proceedings of the Physical Society **92**, 622–631 (1967).

[101] K.-H. Kampert and A. A. Watson, "Extensive air showers and ultra high-energy cosmic rays: A historical review," European Physical Journal H **37**, 359–412 (2012).

[102] G. Sigl, "Ultrahigh-energy cosmic rays: Physics and astrophysics at extreme energies," Science **291**, 73–79 (2001).

[103] J. W. Cronin, "The highest-energy cosmic rays," Nuclear Physics B - Proceedings Supplements **138**, 465–491 (2005).

[104] K. Kotera and A. V. Olinto, "The astrophysics of ultrahigh-energy cosmic rays," Annual Review of Astronomy and Astrophysics **49**, 119–153 (2011).

[105] A. Letessier-Selvon and T. Stanev, "Ultrahigh energy cosmic rays," Reviews of Modern Physics **83**, 907–942 (2011).

[106] A. A. Watson, "High-energy cosmic rays and the Greisen-Zatsepin-Kuz'min effect," Reports on Progress in Physics **77**, 036901 (2014).

[107] J. Linsley, L. Scarsi, and B. Rossi, "Extremely energetic cosmic-ray event," Physical Review Letters **6**, 485–487 (1961).

[108] J. W. Elbert and P. Sommers, "In search of a source for the 320 EeV Fly's Eye cosmic ray," Astrophysical Journal **441**, 151–161 (1995).

[109] P. Bhattacharjee and G. Sigl, "Origin and propagation of extremely high-energy cosmic rays," Physics Reports **327**, 109–247 (2000).

[110] M. Kachelriess and P. D. Serpico, "The Compton-getting effect on ultra-high energy cosmic rays of cosmological origin," Physics Letters B **640**, 225–229 (2006).

[111] R. Alves Batista, J. Biteau, M. Bustamante, K. Dolag, R. Engel, *et al.*, "Open questions in cosmic-ray research at ultrahigh energies," Frontiers in Astronomy and Space Sciences **6**, 23 (2019).

[112] K.-H. Kampert and M. Unger, "Measurements of the cosmic ray composition with air shower experiments," Astroparticle Physics **35**, 660–678 (2012).

[113] S. Das, H. Kang, D. Ryu, and J. Cho, "Propagation of ultra-high-energy protons through the magnetized cosmic web," Astrophysical Journal **682**, 29–38 (2008).

[114] A. Aab *et al.* (Pierre Auger Collaboration), "Combined fit of spectrum and composition data as measured by the Pierre Auger Observatory," Journal of Cosmology and Astroparticle Physics **2017, 04**, 038 (2017).

[115] A. Dundović and G. Sigl, "Anisotropies of ultra-high energy cosmic rays dominated by a single source in the presence of deflections," Journal of Cosmology and Astroparticle Physics **2019, 01**, 018 (2019).

[116] G. Sigl, "The enigma of the highest energy particles of nature," Annals of Physics **303**, 117–141 (2003).

[117] J. J. Beatty and S. Westerhoff, "The highest-energy cosmic rays," Annual Review of Nuclear and Particle Science **59**, 319–345 (2009).

[118] L. A. Anchordoqui, "Ultra-high-energy cosmic rays," Physics Reports **801**, 1–93 (2019).

[119] A. Aab *et al.* (Pierre Auger Collaboration), "Observation of a large-scale anisotropy in the arrival directions of cosmic rays above 8×10^{18} eV," Science **357**, 1266–1270 (2017).

[120] M. R. George, A. C. Fabian, W. H. Baumgartner, R. F. Mushotzky, and J. Tueller, "On active galactic nuclei as sources of ultra-high energy cosmic rays," Monthly Notices of the Royal Astronomical Society **388**, L59–L63 (2008).

[121] S. Chakraborti, A. Ray, A. Soderberg, A. Loeb, and P. Chandra, "Ultra-high-energy cosmic ray acceleration in engine-driven relativistic supernovae," Nature Communications **2**, 175 (2011).

[122] A. Aab *et al.* (Pierre Auger Collaboration), "An indication of anisotropy in arrival directions of ultra-high-energy cosmic rays through comparison to the flux pattern of extragalactic gamma-ray sources," Astrophysical Journal Letters **853**, L29 (2018).

[123] L. A. Anchordoqui, "Acceleration of ultrahigh-energy cosmic rays in starburst superwinds," Physical Review D **97**, 063010 (2018).

[124] R. U. Abbasi *et al.* (Telescope Array Collaboration), "Indications of intermediate-scale anisotropy of cosmic rays with energy greater than 57 EeV in the northern sky measured with the surface detector of the Telescope Array experiment," Astrophysical Journal Letters **790**, L21 (2014).

[125] I. Al Samarai for the Pierre Auger Collaboration, "Indications of anisotropy at large angular scales in the arrival directions of cosmic rays detected at the Pierre Auger Observatory," in *Proceedings of the 34th International Cosmic Ray Conference (ICRC 2015)*, Proceedings of Science (SISSA, Trieste, 2015) p. 372.

[126] A. Aab *et al.* (Pierre Auger Collaboration), "Large scale distribution of ultra high energy cosmic rays detected at the Pierre Auger Observatory with zenith angles up to 80°," Astrophysical Journal **802**, 111 (2015).

[127] A. Aab *et al.* (Pierre Auger Collaboration), "Multi-resolution anisotropy studies of ultrahigh-energy cosmic rays detected at the Pierre Auger Observatory," Journal of Cosmology and Astroparticle Physics **2017, 06**, 026 (2017).

[128] P. Sommers, "Cosmic ray anisotropy analysis with a full-sky observatory," Astroparticle Physics **14**, 271–286 (2001).

[129] A. Aab *et al.* (Pierre Auger Collaboration, Telescope Array Collaboration), "Searches for large-scale anisotropy in the arrival directions of cosmic rays detected above energy of 10^{19} eV at the Pierre Auger Observatory and the Telescope Array," Astrophysical Journal **794**, 172 (2014).

[130] O. Deligny for the Pierre Auger Collaboration and Telescope Array Collaboration, "Large-scale distribution of arrival directions of cosmic rays detected at the Pierre Auger Observatory and the Telescope Array above 10^{19} eV," in *Proceedings of the 34th International Cosmic Ray Conference (ICRC 2015)*, Proceedings of Science (SISSA, Trieste, 2015) p. 395.

[131] A. Franceschini, G. Rodighiero, and M. Vaccari, "Extragalactic optical-infrared background radiation, its time evolution and the cosmic photon-photon opacity," Astronomy & Astrophysics **487**, 837–852 (2008).

[132] T. M. Kneiske and H. Dole, "A lower-limit flux for the extragalactic background light," Astronomy & Astrophysics **515**, A19 (2010).

[133] V. S. Berezinsky and G. T. Zatsepin, "Cosmic rays at ultrahigh-energies (neutrino?)," Physics Letters **28B**, 423–424 (1969).

[134] A. Mann, "IceCube completed," Nature **469**, 13 (2011).

[135] G. W. Sullivan for the IceCube Collaboration, "Results from the IceCube experiment," Nuclear Physics B - Proceedings Supplements **235-236**, 346–351 (2013).

[136] E. Zas for the Pierre Auger Collaboration, "Recent ultra high energy neutrino bounds and multimessenger observations with the Pierre Auger Observatory," *Nuclear Physics in Astrophysics VIII (NPA8): Catania, Italia, June 18-23, 2017*, European Physical Journal Web of Conferences **165**, 01057 (2017).

[137] M. G. Aartsen *et al.* (IceCube Collaboration), "Differential limit on the extremely-high-energy cosmic neutrino flux in the presence of astrophysical background from nine years of IceCube data," Physical Review D **98**, 062003 (2018).

[138] J. Álvarez-Muñiz, R. A. Batista, J. Bolmont, M. Bustamante, W. Carvalho, *et al.*, "The giant radio array for neutrino detection (GRAND): Science and design," Science China Physics, Mechanics & Astronomy **63**, 219501 (2020).

[139] F. W. Stecker, "Diffuse fluxes of cosmic high-energy neutrinos," Astrophysical Journal **228**, 919–927 (1979).

[140] E. Roulet, G. Sigl, A. van Vliet, and S. Mollerach, "PeV neutrinos from the propagation of ultra-high energy cosmic rays," Journal of Cosmology and Astroparticle Physics **2013, 01**, 028 (2013).

[141] A. Van Vliet, J. R. Hörandel, and R. Alves Batista, "Cosmogenic gamma-rays and neutrinos constrain UHECR source models," in *Proceedings of the 35th International Cosmic Ray Conference (ICRC 2017)*, Proceedings of Science (SISSA, Trieste, 2017) p. 562.

[142] P. P. Kronberg, "Extragalactic magnetic fields," Reports on Progress in Physics **57**, 325–382 (1994).

[143] G. Sigl, F. Miniati, and T. A. Ensslin, "Ultrahigh energy cosmic rays in a structured and magnetized universe," Physical Review D **68**, 043002 (2003).

[144] K. Dolag, D. Grasso, V. Springel, and I. Tkachev, "Constrained simulations of the magnetic field in the local universe and the propagation of ultrahigh energy cosmic rays," Journal of Cosmology and Astroparticle Physics **2005, 01**, 009 (2005).

[145] D. Ryu, H. Kang, J. Cho, and S. Das, "Turbulence and magnetic fields in the large-scale structure of the universe," Science **320**, 909–912 (2008).

[146] S. Hackstein, F. Vazza, M. Brueggen, G. Sigl, and A. Dundovic, "Propagation of ultrahigh energy cosmic rays in extragalactic magnetic fields: A view from cosmological simulations," Monthly Notices of the Royal Astronomical Society **462**, 3660–3671 (2016).

[147] R. Alves Batista, M.-S. Shin, J. Devriendt, D. Semikoz, and G. Sigl, "Implications of strong intergalactic magnetic fields for ultrahigh-energy cosmic-ray astronomy," Physical Review D **96**, 023010 (2017).

[148] R. Alves Batista and G. Sigl, "Diffusion of cosmic rays at EeV energies in inhomogeneous extragalactic magnetic fields," Journal of Cosmology and Astroparticle Physics **2014, 11**, 031 (2014).

[149] S. Mollerach and E. Roulet, "Magnetic diffusion effects on the ultra-high energy cosmic ray spectrum and composition," Journal of Cosmology and Astroparticle Physics **2013, 10**, 013 (2013).

[150] K. Fang and K. Murase, "Linking high-energy cosmic particles by black hole jets embedded in large-scale structures," Nature Physics **14**, 396–398 (2018).

[151] A. M. Taylor, "UHECR composition models," Astroparticle Physics **54**, 48–53 (2014).

[152] P. G. Tinyakov and F. R. Urban, "Full sky harmonic analysis hints at large ultra-high energy cosmic ray deflections," Journal of Experimental and Theoretical Physics **120**, 533–540 (2015).

[153] B. Eichmann, J. Becker Tjus, and L. Merten, "Ultra-high-energy cosmic rays from local radio galaxies," arXiv:1701.06792 (2017).

[154] A. M. Hillas, "The origin of ultra-high-energy cosmic rays," Annual Review of Astronomy and Astrophysics **22**, 425–444 (1984).

[155] K. V. Ptitsyna and S. V. Troitsky, "Physical conditions in potential accelerators of ultra-high-energy cosmic rays: Updated Hillas plot and radiation-loss constraints," Physics-Uspekhi **53**, 691–701 (2010).

[156] M. Tavani, A. Giuliani, A. W. Chen, A. Argan, G. Barbiellini, *et al.*, "Direct evidence for hadronic cosmic-ray acceleration in the supernova remnant IC 443," Astrophysical Journal Letters **710**, L151 (2010).

[157] A. Giuliani, M. Cardillo, M. Tavani, Y. Fukui, S. Yoshiike, *et al.*, "Neutral pion emission from accelerated protons in the supernova remnant W44," Astrophysical Journal Letters **742**, L30 (2011).

[158] M. Ackermann, M. Ajello, A. Allafort, L. Baldini, J. Ballet, *et al.* (Fermi-LAT Collaboration), "Detection of the characteristic pion-decay signature in supernova remnants," Science **339**, 807–811 (2013).

[159] P. Blasi, "The origin of galactic cosmic rays," Astronomy and Astrophysics Review **21**, 70 (2013).

[160] J. Becker Tjus and L. Merten, "Closing in on the origin of galactic cosmic rays using multimessenger information," Physics Reports **872**, 1–98 (2020).

[161] L. O. Drury, "An introduction to the theory of diffusive shock acceleration of energetic particles in tenuous plasmas," Reports on Progress in Physics **46**, 973–1027 (1983).

[162] R. Blandford and D. Eichler, "Particle acceleration at astrophysical shocks: A theory of cosmic ray origin," Physics Reports **154**, 1–75 (1987).

[163] F. C. Jones and D. C. Ellison, "The plasma physics of shock acceleration," Space Science Reviews **58**, 259–346 (1991).

[164] J. G. Kirk and P. Duffy, "Particle acceleration and relativistic shocks," Journal of Physics G: Nuclear and Particle Physics **25**, R163–R194 (1999).

[165] M. A. Malkov and L. O. Drury, "Nonlinear theory of diffusive acceleration of particles by shock waves," Reports on Progress in Physics **64**, 429–481 (2001).

[166] A. R. Bell, "Cosmic ray acceleration," Astroparticle Physics **43**, 56–70 (2013).

[167] T. K. Gaisser, R. Engel, and E. Resconi, *Cosmic rays and particle physics*, 2nd ed. (Cambridge University Press, Cambridge, 2016) p. 444.

[168] T. Stanev, *High energy cosmic rays*, 2nd ed. (Springer Science & Business Media, Berlin, 2010).

[169] E. Fermi, "On the origin of the cosmic radiation," Physical Review **75**, 1169–1174 (1949).

[170] V. Petrosian, "Stochastic acceleration by turbulence," Space Science Reviews **173**, 535–556 (2012).

[171] R. J. Protheroe, "Acceleration and interaction of ultra high energy cosmic rays," in *Topics in cosmic-ray astrophysics*, edited by M. A. Duvernois (Nova Science Publishing, New York, 1999) pp. 259–297.

[172] F. M. Rieger, V. Bosch-Ramon, and P. Duffy, "Fermi acceleration in astrophysical jets," Astrophysics and Space Science **309**, 119–125 (2007).

[173] V. A. Acciari *et al.* (VERITAS Collaboration), "A connection between star formation activity and cosmic rays in the starburst galaxy M82," Nature **462**, 770–772 (2009).

[174] A. F. Heavens and L. Drury, "Relativistic shocks and particle acceleration," Monthly Notices of the Royal Astronomical Society **235**, 997–1009 (1988).

[175] P. Schneider and J. G. Kirk, "Particle acceleration at modified shock fronts. I. The power-law spectrum for relativistic flows," Astron. & Astrophys. **217**, 344–350 (1989).

[176] A. Achterberg, Y. A. Gallant, J. G. Kirk, and A. W. Guthmann, "Particle acceleration by ultrarelativistic shocks: Theory and simulations," Monthly Notices of the Royal Astronomical Society **328**, 393–408 (2001).

[177] P. Blasi, R. I. Epstein, and A. V. Olinto, "Ultra-high-energy cosmic rays from young neutron star winds," Astrophysical Journal Letters **533**, L123 (2000).

[178] J. Arons, "Magnetars in the metagalaxy: An origin for ultra-high-energy cosmic rays in the nearby universe," Astrophysical Journal **589**, 871–892 (2003).

[179] R. Fender, K. Wu, H. Johnston, T. Tzioumis, P. Jonker, *et al.*, "An ultra-relativistic outflow from a neutron star accreting gas from a companion," Nature **427**, 222–224 (2004).

[180] N. Bucciantini, T. A. Thompson, J. Arons, E. Quataert, and L. Del Zanna, "Relativistic magnetohydrodynamics winds from rotating neutron stars," Monthly Notices of the Royal Astronomical Society **368**, 1717–1734 (2006).

[181] B. D. Metzger, T. A. Thompson, and E. Quataert, "Proto-neutron star winds with magnetic fields and rotation," Astrophysical Journal **659**, 561 (2007).

[182] J. M. Lattimer and M. Prakash, "The physics of neutron stars," Science **304**, 536–542 (2004).

[183] B. P. Abbott *et al.* (LIGO scientific Collaboration and Virgo Collaboration), "GW170817: Measurements of neutron star radii and equation of state," Physical Review Letters **121**, 161101 (2018).

[184] P. A. Young and D. Arnett, "Massive star evolution," in *Stellar Collapse*, edited by C. L. Fryer (Springer Netherlands, Dordrecht, 2004) pp. 5–38.

[185] S. Chandrasekhar, "The maximum mass of ideal white dwarfs," Astrophysical Journal **74**, 81–82 (1931).

[186] K. Nomoto, S. Miyaji, D. Sugimoto, and K. Yokoi, "Collapse of accreting white dwarf to form a neutron star," in *International Astronomical Union Colloquium*, Vol. 53 (Cambridge University Press, Cambridge, 1979) pp. 56–60.

[187] B. Wang and D. Liu, "The formation of neutron star systems through accretion-induced collapse in white-dwarf binaries," Research in Astronomy and Astrophysics **20**, 135–159 (2020).

[188] J. W. T. Hessels, S. M. Ransom, I. H. Stairs, P. C. C. Freire, V. M. Kaspi, *et al.*, "A radio pulsar spinning at 716 Hz," Science **311**, 1901–1904 (2006).

[189] R. C. Tolman, "Static solutions of Einstein's field equations for spheres of fluid," Physical Review **55**, 364–373 (1939).

[190] J. R. Oppenheimer and G. M. Volkoff, "On massive neutron cores," Physical Review **55**, 374–381 (1939).

[191] C. E. Rhoades Jr and R. Ruffini, "Maximum mass of a neutron star," Physical Review Letters **32**, 324–327 (1974).

[192] I. Bombaci, "The maximum mass of a neutron star." Astronomy & Astrophysics **305**, 871–877 (1996).

[193] R. C. Duncan and C. Thompson, "Formation of very strongly magnetized neutron stars: Implications for gamma-ray bursts," Astrophysical Journal **392**, L9–L13 (1992).

[194] R. Turolla, S. Zane, and A. L. Watts, "Magnetars: The physics behind observations. A review," Reports on Progress in Physics **78**, 116901 (2015).

[195] V. M. Kaspi and A. M. Beloborodov, "Magnetars," Annual Review of Astronomy and Astrophysics **55**, 261–301 (2017).

[196] S. Mereghetti, J. A. Pons, and A. Melatos, "Magnetars: Properties, origin and evolution," Space Science Reviews **191**, 315–338 (2015).

[197] N. Hurley-Walker, X. Zhang, A. Bahramian, S. McSweeney, T. O'Doherty, *et al.*, "A radio transient with unusually slow periodic emission," Nature **601**, 526–530 (2022).

[198] P. Chen, T. Tajima, and Y. Takahashi, "Plasma wakefield acceleration for ultrahigh-energy cosmic rays," Physical Review Letters **89**, 161101 (2002).

[199] M. Hoshino, "Wakefield acceleration by radiation pressure in relativistic shock waves," Astrophysical Journal **672**, 940–956 (2008).

[200] F.-Y. Chang, P. Chen, G.-L. Lin, R. Noble, and R. Sydora, "Magnetowave induced plasma wakefield acceleration for ultrahigh energy cosmic rays," Physical Review Letters **102**, 111101 (2009).

[201] M. M. Romanova and R. V. E. Lovelace, "Magnetic field, reconnection, and particle acceleration in extragalactic jets," Astronomy & Astrophysics **262**, 26–36 (1992).

[202] E. Dal Pino and A. Lazarian, "Ultra-high-energy cosmic-ray acceleration by magnetic reconnection in newborn accretion-induced collapse pulsars," Astrophysical Journal Letters **536**, L31–L34 (2000).

[203] S. Zenitani and M. Hoshino, "The generation of nonthermal particles in the relativistic magnetic reconnection of pair plasmas," Astrophysical Journal Letters **562**, L63–L66 (2001).

[204] M. Ostrowski, "On possible 'cosmic ray cocoons' of relativistic jets," Monthly Notices of the Royal Astronomical Society **312**, 579–584 (2000).

[205] F. M. Rieger and P. Duffy, "Shear acceleration in relativistic astrophysical jets," Astrophysical Journal **617**, 155–161 (2004).

[206] S. S. Kimura, K. Murase, and B. T. Zhang, "Ultrahigh-energy cosmic-ray nuclei from black hole jets: Recycling galactic cosmic rays through shear acceleration," Physical Review D **97**, 023026 (2018).

[207] R. Liu, *Constraining sources of ultrahigh energy cosmic rays and shear acceleration mechanism of particles in relativistic jets*, Ph.D. thesis, Ruprecht Karl University of Heidelberg, Heidelberg (2015).

[208] A. Aab *et al.*, "A targeted search for point sources of EeV neutrons," Astrophysical Journal Letters **789**, L34 (2014).

[209] V. A. Kostelecký and M. Mewes, "Lorentz-violating electrodynamics and the cosmic microwave background," Physical Review Letters **99**, 011601 (2007).

[210] J. Caldeira, W. L. K. Wu, B. Nord, C. Avestruz, S. Trivedi, *et al.*, "DeepCMB: Lensing reconstruction of the cosmic microwave background with deep neural networks," Astronomy and Computing **28**, 100307 (2019).

[211] H. Tashiro, "CMB spectral distortions and energy release in the early universe," Progress of Theoretical and Experimental Physics **2014**, 06B107 (2014).

[212] M. Ackermann, M. Ajello, A. Allafort, P. Schady, L. Baldini, *et al.*, "The imprint of the extragalactic background light in the gamma-ray spectra of blazars," Science **338**, 1190–1192 (2012).

[213] K. Mattila, "The 1-μm discontinuity in the extragalactic background light spectrum: An artefact of foreground subtraction," Monthly Notices of the Royal Astronomical Society **372**, 1253–1258 (2006).

[214] F. Krennrich, E. Dwek, and A. Imran, "Constraints on energy spectra of blazars based on recent EBL limits from galaxy counts," Astrophysical Journal **689**, L93 (2008).

[215] K. Mattila and P. Väisänen, "Extragalactic background light: Inventory of light throughout the cosmic history," Contemporary Physics (2019).

[216] A. Domínguez *et al.*, "Extragalactic background light inferred from AEGIS galaxy-SED-type fractions," Monthly Notices of the Royal Astronomical Society **410**, 2556–2578 (2011).

[217] R. C. Gilmore, R. S. Somerville, J. R. Primack, and A. Domínguez, "Semi-analytic modelling of the extragalactic background light and consequences for extragalactic gamma-ray spectra," Monthly Notices of the Royal Astronomical Society **422**, 3189–3207 (2012).

[218] R. Alves Batista, D. Boncioli, A. di Matteo, A. van Vliet, and D. Walz, "Effects of uncertainties in simulations of extragalactic UHECR propagation, using CRPropa and SimProp," Journal of Cosmology and Astroparticle Physics **2015, 10**, 063 (2015).

[219] M. J. Rees, "The origin and cosmogonic implications of seed magnetic fields," Royal Astronomical Society Quarterly Journal **28**, 197–206 (1987).

[220] L. M. Widrow, "Origin of galactic and extragalactic magnetic fields," Reviews of Modern Physics **74**, 775 (2002).

[221] G. E. Hale, "On the probable existence of a magnetic field in sunspots," Astrophysical Journal **28**, 315–343 (1908).

[222] P. Zeeman, "On the influence of magnetism on the nature of the light emitted by a substance," Astrophysical Journal **5**, 332 (1897).

[223] J. Harvey, "Hale's discovery of sunspot magnetic fields," Astrophysical Journal **525**, 60 (1999).

[224] J. S. Hey, S. J. Parsons, and J. W. Phillips, "Fluctuations in cosmic radiation at radio-frequencies," Nature **158**, 234–234 (1946).

[225] J. G. Bolton and G. J. Stanley, "Variable source of radio frequency radiation in the constellation of Cygnus," Nature **161**, 312–313 (1948).

[226] D. Morris and G. L. Berge, "Direction of the galactic magnetic field in the vicinity of the sun," Astrophysical Journal **139**, 1388–1392 (1964).

[227] G. L. Berge and G. A. Seielstad, "New determinations of the Faraday rotation for extragalactic radio sources," Astrophysical Journal **148**, 367–375 (1967).

[228] R. N. Manchester, "Pulsar rotation and dispersion measures and the galactic magnetic field," Astrophysical Journal **172**, 43–52 (1972).

[229] B. Gold, N. Odegard, J. L. Weiland, R. S. Hill, A. Kogut, *et al.*, "Seven-year Wilkinson Microwave Anisotropy Probe (WMAP*) observations: Galactic foreground emission," Astrophysical Journal Supplement Series **192**, 15 (2011).

[230] R. Jansson and G. R. Farrar, "A new model of the galactic magnetic field," Astrophysical Journal **757**, 14 (2012).

[231] L. Burlaga, N. Ness, and E. Stone, "Magnetic field observations as Voyager 1 entered the heliosheath depletion region," Science **341**, 147–150 (2013).

[232] L. F. Burlaga and N. F. Ness, "Observations of the interstellar magnetic field in the outer heliosheath: Voyager 1," Astrophysical Journal **829**, 134 (2016).

[233] L. F. Burlaga, N. Pogorelov, L. K. Jian, J. Park, A. Szabo, and N. F. Ness, "A large magnetic hump in the VLISM observed by Voyager 1 in 2020–2022," Astrophysical Journal **953**, 135 (2023).

[234] L. F. Burlaga, N. F. Ness, D. B. Berdichevsky, J. Park, L. K. Jian, *et al.*, "Magnetic field and particle measurements made by Voyager 2 at and near the heliopause," Nature Astronomy **3**, 1007–1012 (2019).

[235] J. S. Rankin, D. J. McComas, E. J. Zirnstein, L. F. Burlaga, and J. Heerikhuisen, "Unified picture of the local interstellar magnetic field from Voyager and IBEX," Astrophysical Journal Letters **945**, L31 (2023).

[236] R. Jansson, G. R. Farrar, A. H. Waelkens, and T. A. Enßlin, "Constraining models of the large scale galactic magnetic field with WMAP5 polarization data and extragalactic rotation measure sources," Journal of Cosmology and Astroparticle Physics **2009, 07**, 021 (2009).

[237] R. Beck, "Galactic and extragalactic magnetic fields," Space Science Reviews **99**, 243–260 (2001).

[238] R. Beck, "Measurements of cosmic magnetism with LOFAR and SKA," Advances in Radio Science **5**, 399–405 (2007).

[239] R. Stepanov, T. G. Arshakian, R. Beck, P. Frick, and M. Krause, "Magnetic field structures of galaxies derived from analysis of Faraday rotation measures, and perspectives for the SKA," Astronomy & Astrophysics **480**, 45–59 (2008).

[240] S. A. Mao, "Magnetism in the Square Kilometre Array era," Proceedings of the International Astronomical Union **14**, 307–310 (2018).

[241] J. Farnes, B. Mort, F. Dulwich, S. Salvini, and W. Armour, "Science pipelines for the Square Kilometre Array," Galaxies **6**, 120 (2018).

[242] R. Jansson and G. R. Farrar, "The galactic magnetic field," Astrophysical Journal Letters **761**, L11 (2012).

[243] M. Erdmann, G. Müller, M. Urban, and M. Wirtz, "The nuclear window to the extragalactic universe," Astroparticle Physics **85**, 54–64 (2016).

[244] G. R. Farrar and M. S. Sutherland, "Deflections of UHECRs in the galactic magnetic field," Journal of Cosmology and Astroparticle Physics **2019, 05**, 004 (2019).

[245] J. L. Han, R. N. Manchester, and G. J. Qiao, "Pulsar rotation measures and the magnetic structure of our galaxy," Monthly Notices of the Royal Astronomical Society **306**, 371–380 (1999).

[246] J. L. Han, "New knowledge of the galactic magnetic fields," Nuclear Physics B - Proceedings Supplements **175**, 62–69 (2008).

[247] H. C. Van de Hulst, "Observing the galactic magnetic field," Annual Review of Astronomy and Astrophysics **5**, 167–182 (1967).

[248] R. Durrer and A. Neronov, "Cosmological magnetic fields: Their generation, evolution and observation," Astronomy and Astrophysics Review **21**, 62 (2013).

[249] K. Subramanian, "The origin, evolution and signatures of primordial magnetic fields," Reports on Progress in Physics **79**, 076901 (2016).

[250] T. E. Clarke, P. P. Kronberg, and H. Böhringer, "A new radio-X-ray probe of galaxy cluster magnetic fields," Astrophysical Journal Letters **547**, L111–L114 (2001).

[251] F. Govoni and L. Feretti, "Magnetic fields in clusters of galaxies," International Journal of Modern Physics D **13**, 1549–1594 (2004).

[252] A. Bonafede, L. Feretti, M. Murgia, F. Govoni, G. Giovannini, *et al.*, "The Coma cluster magnetic field from Faraday rotation measures," Astronomy & Astrophysics **513**, A30 (2010).

[253] L. Feretti, G. Giovannini, F. Govoni, and M. Murgia, "Clusters of galaxies: Observational properties of the diffuse radio emission," Astronomy and Astrophysics Review **20**, 54 (2012).

[254] E. Ricciardelli, V. Quilis, and S. Planelles, "The structure of cosmic voids in a ΛCDM universe," Monthly Notices of the Royal Astronomical Society **434**, 1192–1204 (2013).

[255] A. Neronov and I. Vovk, "Evidence for strong extragalactic magnetic fields from Fermi observations of TeV blazars," Science **328**, 73–75 (2010).

[256] A. M. Beck, M. Hanasz, H. Lesch, R.-S. Remus, and F. A. Stasyszyn, "On the magnetic fields in voids," Monthly Notices of the Royal Astronomical Society Letters **429**, L60–L64 (2013).

[257] P. A. R. Ade *et al.* (Planck Collaboration), "Planck 2015 results-XIX. Constraints on primordial magnetic fields," Astronomy & Astrophysics **594**, A19 (2016).

[258] K. Jedamzik and A. Saveliev, "Stringent limit on primordial magnetic fields from the cosmic microwave background radiation," Physical Review Letters **123**, 021301 (2019).

[259] F. Vazza, M. Brueggen, C. Gheller, S. Hackstein, D. Wittor, *et al.*, "Simulations of extragalactic magnetic fields and of their observables," Classical and Quantum Gravity **34**, 234001 (2017).

[260] S. Hackstein, F. Vazza, M. Brüggen, J. G. Sorce, and S. Gottlöber, "Simulations of ultra-high energy cosmic rays in the local Universe and the origin of cosmic magnetic fields," Monthly Notices of the Royal Astronomical Society **475**, 2519–2529 (2018).

[261] R. Alves Batista, A. Dundovic, M. Erdmann, K.-H. Kampert, D. Kuempel, G. Müller, G. Sigl, *et al.*, "CRPropa 3–a public astrophysical simulation framework for propagating extraterrestrial

ultra-high energy particles," Journal of Cosmology and Astroparticle Physics **2016, 05**, 038 (2016).

[262] G. Sigl, F. Miniati, and T. A. Enßlin, "Ultrahigh energy cosmic ray probes of large scale structure and magnetic fields," Physical Review D **70**, 043007 (2004).

[263] D. Ryu, S. Das, and H. Kang, "Intergalactic magnetic field and arrival direction of ultra-high-energy protons," Astrophysical Journal **710**, 1422–1431 (2010).

[264] R. Engel, D. Heck, and T. Pierog, "Extensive air showers and hadronic interactions at high energy," Annual Review of Nuclear and Particle Science **61**, 467–489 (2011).

[265] K.-H. Kampert, M. A. Mostafa, E. Zas, and Pierre Auger Collaboration, "Multi-messenger physics with the Pierre Auger Observatory," Frontiers in Astronomy and Space Sciences **6**, 24 (2019).

[266] D. Ciampa and R. W. Clay, "The zenith angle distribution of extensive air showers at sea level: A measure of shower development," Journal of Physics G: Nuclear Physics **14**, 787–792 (1988).

[267] I. V. Rielo, *Detection of horizontal air showers and neutrino induced showers with the Pierre Auger Observatory*, Ph.D. thesis, University of Santiago de Compostela, Santiago de Compostela (2007).

[268] L. Anchordoqui, M. T. Dova, A. Mariazzi, T. McCauley, T. Paul, *et al.*, "High energy physics in the atmosphere: Phenomenology of cosmic ray air showers," Annals of Physics **314**, 145–207 (2004).

[269] S. Chapman, "The absorption and dissociative or ionizing effect of monochromatic radiation in an atmosphere on a rotating earth part II. Grazing incidence," Proceedings of the Physical Society **43**, 483–501 (1931).

[270] A. Haungs, H. Rebel, and M. Roth, "Energy spectrum and mass composition of high-energy cosmic rays," Reports on Progress in Physics **66**, 1145–1206 (2003).

[271] T. K. Gaisser and A. M. Hillas, "Reliability of the method of constant intensity cuts for reconstructing the average development of vertical showers," in *Proceedings of the 15th International Cosmic Ray Conference (ICRC 1977)*, Vol. 8 (1977) pp. 353–357.

[272] D. Veberič, "Lambert W function for applications in physics," Computer Physics Communications **183**, 2622–2628 (2012).

[273] A. Aab *et al.* (Pierre Auger Collaboration), "Data-driven estimation of the invisible energy of cosmic ray showers with the Pierre Auger Observatory," Physical Review D **100**, 082003 (2019).

[274] A. Aab *et al.* (Pierre Auger Collaboration), "Depth of maximum of air-shower profiles at the Pierre Auger Observatory. I. Measurements at energies above $10^{17.8}$ eV," Physical Review D **90**, 122005 (2014).

[275] R. G. Glasser, N. Seeman, and B. Stiller, "Mean lifetime of the neutral pion," Physical Review **123**, 1014–1020 (1961).

[276] R. Miskimen, "Neutral pion decay," Annual Review of Nuclear and Particle Science **61**, 1–21 (2011).

[277] O. Scholten and K. Werner, "Macroscopic model of geomagnetic-radiation from air showers," Nuclear Instruments and Methods in Physics Research Section A **604**, S24–S26 (2009).

[278] N. N. Kalmykov and A. A. Konstantinov, "Macroscopic model of radio emission from extensive air showers," Physics of Atomic Nuclei **74**, 1019–1031 (2011).

[279] D. Ardouin, A. Belletoile, C. Berat, *et al.*, "Geomagnetic origin of the radio emission from cosmic ray induced air showers observed by CODALEMA," Astroparticle Physics **31**, 192–200 (2009).

[280] J. Alvarez-Muñiz, W. R. Carvalho Jr, H. Schoorlemmer, and E. Zas, "Radio pulses from ultra-high energy atmospheric showers as the superposition of Askaryan and geomagnetic mechanisms," Astroparticle Physics **59**, 29–38 (2014).

[281] G. A. Askar'yan, "Excess negative charge of an electron-photon shower and its coherent radio emission," Zh. Eksperim. Teor. Fiz. **41**, 616–618 (1961).

[282] G. A. Askar'yan, "Coherent radioemission from cosmic showers in the air and dense media," Zh. Eksperim. Teor. Fiz. **48**, 988–990 (1965).

[283] T. Huege, "Radio detection of cosmic ray air showers in the digital era," Physics Reports **620**, 1–52 (2016).

[284] C. Glaser, S. de Jong, M. Erdmann, and J. R. Hörandel, "An analytic description of the radio emission of air showers based on its emission mechanisms," Astroparticle Physics **104**, 64–77 (2019).

[285] F. Schlüter, M. Gottowik, T. Huege, and J. Rautenberg, "Refractive displacement of the radio-emission footprint of inclined air showers simulated with CoREAS," The European Physical Journal C **80**, 643 (2020).

[286] T. Bergmann, R. Engel, D. Heck, N. N. Kalmykov, S. Ostapchenko, *et al.*, "One-dimensional hybrid approach to extensive air shower simulation," Astroparticle Physics **26**, 420–432 (2007).

[287] D. Heck, J. Knapp, J. N. Capdevielle, G. Schatz, and T. Thouw, "CORSIKA: A Monte Carlo code to simulate extensive air showers," Forschungszentrum Karlsruhe, report **FZKA 6019** (1998).

[288] D. Heck and J. Knapp, "Upgrade of the Monte Carlo code CORSIKA to simulate extensive air showers with energies $> 10^{20}$ eV," Forschungszentrum Karlsruhe, report **FZKA 6097B** (1998).

[289] A. M. Hillas, "Angular and energy distributions of charged particles in electron-photon cascades in air," Journal of Physics G: Nuclear Physics **8**, 1461–1473 (1982).

[290] A. Śmiałkowski and M. Giller, "Universality of electron distributions in extensive air showers," Astrophysical Journal **854**, 48 (2018).

[291] K. Kamata and J. Nishimura, "The lateral and the angular structure functions of electron showers," Progress of Theoretical Physics Supplement **6**, 93–155 (1958).

[292] K. Greisen, "Cosmic ray showers," Annual Review of Nuclear Science **10**, 63–108 (1960).

[293] Pierre Auger Collaboration, "The rapid atmospheric monitoring system of the Pierre Auger Observatory," Journal of Instrumentation **7**, P09001 (2012).

[294] B. Keilhauer and M. Will for the Pierre Auger Collaboration, "Description of atmospheric conditions at the Pierre Auger Observatory using meteorological measurements and models," The European Physical Journal Plus **127**, 1–10 (2012).

[295] A. Aab *et al.* (Pierre Auger Collaboration), "The FRAM robotic telescope for atmospheric monitoring at the Pierre Auger Observatory," Journal of Instrumentation **16**, P06027 (2021).

[296] J. Abraham *et al.* (Pierre Auger Collaboration), "Atmospheric effects on extensive air showers observed with the surface detector of the Pierre Auger Observatory," Astroparticle Physics **32**, 89–99 (2009).

[297] L. Evans, "The Large Hadron Collider," New Journal of Physics **9**, 335 (2007).

[298] L. Evans, "The Large Hadron Collider," Annual Review of Nuclear and Particle Science **61**, 435–466 (2011).

[299] D. O'Hanlon, "The Large Hadron Collider," in *Studies of CP-violation in charmless three-body b-hadron decays* (Springer Theses, Springer Nature Switzerland AG, Switzerland, 2018) pp. 25–35.

[300] M. Aaboud *et al.* (ATLAS Collaboration), "Measurement of the inelastic proton-proton cross section at $\sqrt{s} = 13$ TeV with the ATLAS detector at the LHC," Physical Review Letters **117**, 182002 (2016).

[301] Antoine Letessier-Selvon for the Pierre Auger Collaboration, "Highlights from the Pierre Auger Observatory," Brazilian Journal of Physics **44**, 560–570 (2014).

[302] J. Vícha and Pierre Auger Collaboration, "Probing the universe at the highest energies with the Pierre Auger Observatory," Astronomische Nachrichten **340**, 57–61 (2019).

[303] J. Abraham *et al.* (Pierre Auger Collaboration), "Properties and performance of the prototype instrument for the Pierre Auger Observatory," Nuclear Instruments and Methods in Physics Research Section A **523**, 50–95 (2004).

[304] Miguel Mostafá for the Pierre Auger Collaboration, "Hybrid activities of the Pierre Auger Observatory," Nuclear Physics B - Proceedings Supplements **165**, 50–58 (2007).

[305] C. Berat and Pierre Auger Collaboration, "Radio detection of extensive air showers at the Pierre Auger Observatory," Nuclear Instruments and Methods in Physics Research Section A **718**, 471–474 (2013).

[306] R. Gaïor, *EASIER: Extensive air shower identification using electron radiometer*, Ph.D. thesis, Pierre and Marie Curie University, Paris (2013).

[307] R. Gaïor, I. Al Samarai, C. Berat, M. B. Otano, J. David, *et al.*, "GIGAS: A set of microwave sensor arrays to detect molecular bremsstrahlung radiation from extensive air shower," Nuclear Instruments and Methods in Physics Research Section A **888**, 153–162 (2018).

[308] M. Ambrosio, C. Aramo, F. Bracci, P. Facal, R. Fonte, *et al.*, "The camera of the Pierre Auger Observatory fluorescence detector," Nuclear Instruments and Methods in Physics Research Section A **478**, 125–129 (2002).

[309] Frank G. Schröder for the Pierre Auger Collaboration, "Radio detection of high-energy cosmic rays with the Auger Engineering Radio Array," Nuclear Instruments and Methods in Physics Research Section A **824**, 648–651 (2016).

[310] B. Zimmermann for the Pierre Auger Collaboration, "Cosmic ray physics with the Auger Engineering Radio Array (AERA)," Nuclear and Particle Physics Proceedings **291-293**, 90–95 (2017).

[311] A. Aab *et al.* (Pierre Auger Collaboration), "Design, upgrade and characterization of the silicon photomultiplier front-end for the AMIGA detector at the Pierre Auger Observatory," Journal of Instrumentation **16**, P01026 (2021).

[312] A. Aab *et al.* (Pierre Auger Collaboration), "The Pierre Auger Observatory upgrade "AugerPrime" preliminary design report," arXiv:1604.03637 (2016).

[313] G. Cataldi and Pierre Auger Collaboration, "Towards AugerPrime: The upgrade of the Pierre Auger Observatory," Nuclear and Particle Physics Proceedings **291**, 96–101 (2017).

[314] A. Castellina and Pierre Auger Collaboration, "AugerPrime: The Pierre Auger Observatory upgrade," European Physical Journal Web of Conferences **210**, 06002 (2019).

[315] Ralph Engel for the Pierre Auger Collaboration, "Upgrade of the Pierre Auger Observatory (AugerPrime)," in *Proceedings of the 34th International Cosmic Ray Conference (ICRC 2015)*, Proceedings of Science, Vol. 236 (SISSA, Trieste, 2016) p. 686.

[316] J. R. Hörandel, "Precision measurements of cosmic rays up to the highest energies with a large radio array at the Pierre Auger Observatory," European Physical Journal Web of Conferences **210**, 06005 (2019).

[317] P. Abreu *et al.* (Pierre Auger Collaboration), "Antennas for the detection of radio emission pulses from cosmic-ray induced air showers at the Pierre Auger Observatory," Journal of Instrumentation **7**, P10011 (2012).

[318] H. Kawai *et al.* (Telescope Array Collaboration), "Measurement of ultra-high energy cosmic rays by Telescope Array (TA)," Journal of the Physical Society of Japan Supplement A **78**, 108–113 (2009).

[319] John N. Matthews for the Telescope Array Collaboration, "First results from the Telescope Array," Nuclear Physics B - Proceedings Supplements **212-213**, 79–86 (2011).

[320] R. U. Abbasi *et al.* (Telescope Array Collaboration), "Surface detectors of the TAx4 experiment," Nuclear Instruments and Methods in Physics Research Section A **1019**, 165726 (2021).

[321] H. Tokuno, Y. Tameda, M. Takeda, K. Kadota, D. Ikeda, *et al.*, "New air fluorescence detectors employed in the Telescope Array experiment," Nuclear Instruments and Methods in Physics Research Section A **676**, 54–65 (2012).

[322] K. Martens for the Telescope Array Collaboration, "The telescope array and its low energy extension," Nuclear Physics B (Proceedings Supplements) **165**, 33–36 (2007).

[323] Hiroyuki Sagawa for the Telescope Array Collaboration, "Telescope Array extension," Nuclear and Particle Physics Proceedings **279-281**, 145–152 (2016).

[324] O. Shoichi for the Telescope Array Collaboration, "Telescope Array Low energy Extension: TALE," in *Proceedings of 2016 International Conference on Ultra-High Energy Cosmic Rays (UHECR2016)*, JPS Conference Proceedings, Vol. 19 (Physical Society of Japan, Tokyo, 2018) p. 011026.

[325] D. Bergman for the Telescope Array Collaboration, "Telescope Array: Latest results and expansion plans," Journal of Physics: Conference Series **1468**, 012078 (2020).

[326] Y. Omura, D. R. Bergman, J. F. Krizmanic, K. Nakai, and Y. Tsunesada, "NICHE detector and operations," Journal of Physics: Conference Series **1468**, 012097 (2020).

[327] E. Kido on behalf of the Telescope Array Collaboration, "Status and prospects of the TA×4 experiment," European Physical Journal Web of Conferences **210**, 06001 (2019).

[328] E. Kido for the Telescope Array Collaboration, "The TA×4 experiment," Proceedings of 2016 International Conference on Ultra-High Energy Cosmic Rays (UHECR2016), JPS Conference Proceedings **19**, 011025 (2018).

[329] P. Abreu *et al.* (Pierre Auger Collaboration), "Ultrahigh energy neutrinos at the Pierre Auger Observatory," Advances in High Energy Physics **2013**, 708680 (2013).

[330] V. S. Berezinsky and A. Y. Smirnov, "Cosmic neutrinos of ultra-high energies and detection possibility," Astrophysics and Space Science **32**, 461–482 (1975).

[331] D. Williams and IceCube Collaboration, "Status and prospects for the IceCube neutrino observatory," Nuclear Instruments and Methods in Physics Research Section A **952**, 161650 (2020).

[332] M. G. Aartsen *et al.* (IceCube Collaboration), "The IceCube neutrino observatory: Instrumentation and online systems," Journal of Instrumentation **12**, P03012 (2017).

[333] R. Abbasi *et al.* (IceCube Collaboration), "IceTop: The surface component of IceCube," Nuclear Instruments and Methods in Physics Research Section A **700**, 188–220 (2013).

[334] M. G. Aartsen *et al.* (IceCube Collaboration), "Evidence for high-energy extraterrestrial neutrinos at the IceCube detector," Science **342**, 1242856 (2013).

[335] P. K. F. Grieder, *Cosmic rays at Earth*, 1st ed. (Elsevier Science B.V., Amsterdam, 2001).

[336] K.-H. Kampert, "Methods of determination of the energy and mass of primary cosmic ray particles at extensive air shower energies," Journal of Physics G: Nuclear and Particle Physics **27**, 1663–1673 (2001).

[337] L. J. Gleeson and W. I. Axford, "Solar modulation of galactic cosmic rays," Astrophysical Journal **154**, 1011–1026 (1968).

[338] M. S. Potgieter, "Solar modulation of cosmic rays," Living Reviews in Solar Physics **10**, 1–66 (2013).

[339] A. Aab *et al.* (Pierre Auger Collaboration), "Measurement of the cosmic-ray energy spectrum above 2.5×10^{18}eV using the Pierre Auger Observatory," Physical Review D **102**, 062005 (2020).

[340] A. Castellina for the Pierre Auger Collaboration, "Astroparticle and particle physics at ultra-high energy: Results from the Pierre Auger Observatory," SciPost Physics Proceedings **13**, 034 (2023).

[341] G. Sigl, D. N. Schramm, and P. Bhattacharjee, "On the origin of highest energy cosmic rays," Astroparticle Physics **2**, 401–414 (1994).

[342] D. J. Bird, S. C. Corbató, H. Y. Dai, B. R. Dawson, J. W. Elbert, *et al.*, "Evidence for correlated changes in the spectrum and composition of cosmic rays at extremely high energies," Physical Review Letters **71**, 3401–3404 (1993).

[343] A. D'Amone et al. for the ARGO-YBJ Collaboration, "Observation of a knee in the p+He energy spectrum below 1 PeV by measuring particle densities very close to the EAS core with the ARGO-YBJ experiment," in *Proceedings of the 34th International Cosmic Ray Conference (ICRC 2015)*, Proceedings of Science (SISSA, Trieste, 2015) p. 366.

[344] A. D. Panov, J. H. Adams Jr., H. S. Ahn, G. L. Bashinzhagyan, J. W. Watts, *et al.*, "Energy spectra of abundant nuclei of primary cosmic rays from the data of ATIC-2 experiment: Final results," Bulletin of the Russian Academy of Sciences: Physics **73**, 564–567 (2009).

[345] R. U. Abbasi *et al.* (High Resolution Fly's Eye Collaboration), "First observation of the Greisen-Zatsepin-Kuzmin suppression," Physical Review Letters **100**, 101101 (2008).

[346] I. Valiño for the Pierre Auger Collaboration, "The flux of ultra-high energy cosmic rays after ten years of operation of the Pierre Auger Observatory," in *Proceedings of the 34th International Cosmic Ray Conference (ICRC 2015)*, Proceedings of Science (SISSA, Trieste, 2015) p. 271.

[347] I. P. Ivanenko, V. Y. Shestoperov, L. O. Chikova, I. M. Fateeva, L. A. Khein, *et al.*, "Energy spectra of cosmic rays above 2 TeV as measured by the "SOKOL" apparatus," in *Proceedings of the 23rd International Cosmic Ray Conference (ICRC 1993)*, Vol. 2 (1993) p. 17.

[348] C. C. H. Jui for the Telescope Array Collaboration, "Summary of results from the Telescope Array experiment," in *Proceedings of the 34th International Cosmic Ray Conference (ICRC 2015)*, Proceedings of Science (SISSA, Trieste, 2015) p. 035.

[349] M. Amenomori *et al.* (Tibet ASγ Collaboration), "The all-particle spectrum of primary cosmic rays in the wide energy range from 10^{14} to 10^{17} eV observed with the Tibet-III air-shower array," Astrophysical Journal **678**, 1165–1179 (2008).

[350] G. Adams, G. Lee, V. I. Zatsepin, M. I. Panasyuk, and N. V. Sokolskaya, "Spectra of all primary cosmic ray particles: TIC experiment data," Bulletin of the Russian Academy of Sciences: Physics **61**, 922–925 (1997).

[351] S. F. Berezhnev, N. M. Budnev, A. Chiavassa, O. A. Chvalaev, O. A. Gress, *et al.*, "The primary CR spectrum by the data of the Tunka-133 array," JPS conference proceedings, Proceedings of international symposium for ultra-high energy cosmic rays (UHECR2014) **9**, 010009 (2016).

[352] N. Budnev, D. Chernov, O. Gress, E. Korosteleva, L. Kuzmichev, *et al.*, "Tunka-25 air shower Cherenkov array: The main results," Astroparticle Physics **50**, 18–25 (2013).

[353] A. Coleman, J. Eser, E. Mayotte, F. Sarazin, F. G. Schröder, *et al.*, "Ultra high energy cosmic rays The intersection of the Cosmic and Energy Frontiers," Astroparticle physics **149**, 102819 (2023).

[354] J. Abraham *et al.* (Pierre Auger Collaboration), "Measurement of the depth of maximum of extensive air showers above 10^{18} eV," Physical Review Letters **104**, 091101 (2010).

[355] A. Abdul Halim *et al.* (Pierre Auger Collaboration), "Radio measurements of the depth of air-shower maximum at the Pierre Auger Observatory," Physical Review D **109**, 022002 (2024).

[356] J. P. Huchra, L. M. Macri, K. L. Masters, T. H. Jarrett, P. Berlind, *et al.*, "The 2MASS Redshift Survey-description and data release," Astrophysical Journal Supplement Series **199**, 26 (2012).

[357] A. Aab *et al.* (Pierre Auger Collaboration), "Searches for anisotropies in the arrival directions of the highest energy cosmic rays detected by the Pierre Auger Observatory," Astrophysical Journal **804**, 15 (2015).

[358] M.-P. Véron-Cetty and P. Véron, "A catalogue of quasars and active nuclei: 12th edition," Astronomy & Astrophysics **455**, 773–777 (2006).

[359] R. U. Abbasi *et al.* (Telescope Array Collaboration), "An extremely energetic cosmic ray observed by a surface detector array," Science **382**, 903–907 (2023).

[360] T. Abu-Zayyad *et al.* (Telescope Array Collaboration), "The cosmic-ray energy spectrum observed with the surface detector of the telescope array experiment," Astrophysical Journal Letters **768**, L1 (2013).

[361] R. B. Tully, E. J. Shaya, I. D. Karachentsev, H. M. Courtois, D. D. Kocevski, *et al.*, "Our peculiar motion away from the Local Void," Astrophysical Journal **676**, 184 (2008).

[362] I. D. Karachentsev and M. E. Sharina, "Distance to the spiral galaxy NGC 6503 situated in the Local Void," Astronomy & Astrophysics **324**, 457–460 (1997).

[363] A. Addazi, J. Alvarez-Muniz, R. Alves Batista, G. Amelino-Camelia, V. Antonelli, *et al.*, "Quantum gravity phenomenology at the dawn of the multi-messenger era – A review," Progress in Particle and Nuclear Physics **125**, 103948 (2022).

[364] A. Aab *et al.* (Pierre Auger Collaboration), "Large-scale cosmic-ray anisotropies above 4 EeV measured by the Pierre Auger Observatory," Astrophysical Journal **868**, 4 (2018).

[365] A. Aab *et al.* (Pierre Auger Collaboration), "Cosmic-ray anisotropies in right ascension measured by the Pierre Auger Observatory," Astrophysical Journal **891**, 142 (2020).

[366] O. M. Miller, "Notes on cylindrical world map projections," Geographical Review **32**, 424–430 (1942).

[367] J. Keuning, "The history of geographical map projections until 1600," Imago Mundi **12**, 1–24 (1955).

[368] J. P. Snyder, *Flattening the Earth: Two thousand years of map projections* (University of Chicago Press, Chicago, 1997) p. 384.

[369] J. R. Gott, D. M. Goldberg, and R. J. Vanderbei, "Flat maps that improve on the Winkel Tripel," arXiv:2102.08176 (2021).

[370] A. Tissot, *Mémoire sur la représentation des surfaces et les projections des cartes géographiques* (Gauthier-Villars, Paris, 1881).

[371] P. H. Laskowski, "The traditional and modern look at Tissot's indicatrix," The American Cartographer **16**, 123–133 (1989).

[372] R. U. Abbasi *et al.* (Telescope Array Collaboration), "Evidence for a supergalactic structure of magnetic deflection multiplets of ultra-high-energy cosmic rays," Astrophysical Journal **899**, 86 (2020).

[373] R. C. Dos Anjos, J. F. Soriano, L. A. Anchordoqui, T. C. Paul, D. F. Torres, *et al.*, "Ultrahigh-energy cosmic ray composition from the distribution of arrival directions," Physical Review D **98**, 123018 (2018).

[374] T. Stanev, P. L. Biermann, J. Lloyd-Evans, J. P. Rachen, and A. A. Watson, "Arrival directions of the most energetic cosmic rays," Physical Review Letters **75**, 3056–3059 (1995).

[375] C. F. Gauss, *Disquisitiones generales circa superficies curvas*, Vol. 1 (Typis Dieterichianis, Gottingae, 1828).

[376] C. G. Gray and K. E. Gubbins, *Theory of Molecular Fluids: Fundamentals*, 1st ed., International Series of Monographs on Chemistry 9, Vol. 1 (Oxford University Press, Oxford, 1984) p. 626.

[377] L. Merten, J. B. Tjus, H. Fichtner, B. Eichmann, and G. Sigl, "CR-Propa 3.1 – a low energy extension based on stochastic differential equations," Journal of Cosmology and Astroparticle Physics **2017, 06**, 046 (2017).

[378] P. Abreu *et al.* (Pierre Auger Collaboration), "Bounds on the density of sources of ultra-high energy cosmic rays from the Pierre Auger Observatory," Journal of Cosmology and Astroparticle Physics **2013, 05**, 009 (2013).

[379] A. J. Koning, S. Hilaire, and M. C. Duijvestijn, "TALYS: Comprehensive nuclear reaction modeling," AIP Conference Proceedings **769**, 1154–1159 (2005).

[380] A. J. Koning and D. Rochman, "Modern nuclear data evaluation with the TALYS code system," Nuclear Data Sheets **113**, 2841–2934 (2012).

[381] A. Haghighat, *Monte Carlo methods for particle transport*, 1st ed., Vol. 1 (CRC Press, Boca Raton, 2016).

[382] G. Müller, *A search for sources of extragalactic cosmic rays using structured magnetic fields and advanced propagation software with the Pierre Auger Observatory*, Ph.D. thesis, RWTH Aachen University, Aachen (2016).

[383] E. Armengaud, G. Sigl, T. Beau, and F. Miniati, "CRPropa: A numerical tool for the propagation of UHE cosmic rays, γ-rays and neutrinos," Astroparticle Physics **28**, 463–471 (2007).

[384] M. Plum for the Pierre Auger Collaboration, "Measurement of the chemical composition of the ultra-high-energy cosmic rays with the Pierre Auger Observatory," arXiv:1501.06325 (2015).

[385] M. De Domenico, M. Settimo, S. Riggi, and E. Bertin, "Reinterpreting the development of extensive air showers initiated by nuclei and photons," Journal of Cosmology and Astroparticle Physics **2013, 07**, 050 (2013).

[386] T. Pierog, M. K. Alekseeva, T. Bergmann, V. Chernatkin, R. Engel, *et al.*, "First results of fast one-dimensional hybrid simulation of EAS using CONEX," Nuclear Physics B - Proceedings Supplements **151**, 159–162 (2006).

[387] T. Pierog, I. Karpenko, J. M. Katzy, E. Yatsenko, and K. Werner, "EPOS LHC: Test of collective hadronization with data measured at the CERN Large Hadron Collider," Physical Review C **92**, 034906 (2015).

[388] M. Erdmann and D. Walz, "Constraining UHECR source scenarios with spectrum and $X_{\max}$ distributions," Internal Note of the Pierre Auger Collaboration **GAP Note 2014-034** (2014).

[389] D. Walz, *Constraining models of the extragalactic cosmic ray origin with the Pierre Auger Observatory*, Ph.D. thesis, RWTH Aachen University, Aachen (2016).

[390] A. Patil, D. Huard, and C. Fonnesbeck, "PyMC: Bayesian stochastic modelling in Python," Journal of Statistical Software **35**, 1–81 (2010).

[391] T. Wibig and A. W. Wolfendale, "Cosmic rays of the highest energies," Romanian Reports in Physics **59**, 707 (2007).

[392] K. M. Gorski, E. Hivon, A. J. Banday, B. D. Wandelt, F. K. Hansen, *et al.*, "HEALPix: A framework for high-resolution discretization and fast analysis of data distributed on the sphere," Astrophysical Journal **622**, 759 (2005).

[393] C. Bonifazi *et al.* (Pierre Auger Collaboration), "The angular resolution of the Pierre Auger Observatory," Nuclear Physics B - Proceedings Supplements **190**, 20–25 (2009).

[394] A. M. Taylor, M. Ahlers, and D. Hooper, "Indications of negative evolution for the sources of the highest energy cosmic rays," Physical Review D **92**, 063011 (2015).

[395] H. Takami, S. Inoue, and T. Yamamoto, "Propagation of ultra-high-energy cosmic ray nuclei in cosmic magnetic fields and implications for anisotropy measurements," Astroparticle Physics **35**, 767–780 (2012).

[396] P. Allison *et al.* (The ARA Collaboration), "Performance of two Askaryan Radio Array stations and first results in the search for ultrahigh energy neutrinos," Physical Review D **93**, 082003 (2016).

[397] C. R. Persichilli, *Performance and simulation of the ARIANNA pilot array, with implications for future ultra-high energy neutrino astronomy*, Ph.D. thesis, University of California, Irvine, California (2018).

[398] A. N. Otte, "Studies of an air-shower imaging system for the detection of ultrahigh-energy neutrinos," Physical Review D **99**, 083012 (2019).

[399] R. Aloisio and V. Berezinsky, "Diffusive propagation of ultra-high-energy cosmic rays and the propagation theorem," Astrophysical Journal **612**, 900–913 (2004).

[400] A. Aab *et al.* (Pierre Auger Collaboration), "Search for photons with energies above 10^{18} eV using the hybrid detector of the Pierre Auger Observatory," Journal of Cosmology and Astroparticle Physics **2017, 04**, 009 (2017).

[401] J. Knödlseder, "The future of gamma-ray astronomy," Comptes Rendus Physique **17**, 663–678 (2016).

[402] D. Cyranoski, "China seeks cosmic-ray win," Nature **543**, 300–301 (2017).

[403] P. Allison *et al.* (ARA Collaboration), "Design and initial performance of the Askaryan Radio Array prototype EeV neutrino detector at the South Pole," Astroparticle Physics **35**, 457–477 (2012).

[404] S. W. Barwick *et al.* (ARIANNA Collaboration), "A first search for cosmogenic neutrinos with the ARIANNA hexagonal radio array," Astroparticle Physics **70**, 12–26 (2015).

[405] O. Martineau-Huynh, M. Bustamante, W. Carvalho, *et al.*, "The Giant Radio Array for Neutrino Detection," European Physical Journal Web of Conferences **135**, 02001 (2017).

[406] J. van Santen for the IceCube-Gen2 Collaboration (IceCube Gen2 Collaboration), "Icecube-Gen2: The next-generation neutrino observatory for the South Pole," in *Proceedings of the 35th International Cosmic Ray Conference (ICRC 2017)*, Proceedings of Science (SISSA, Trieste, 2017) p. 991.

[407] A. V. Olinto, J. H. Adams, R. Aloisio, L. A. Anchordoqui, D. R. Bergman, *et al.*, "POEMMA: Probe of extreme multi-messenger astrophysics," in *Proceedings of the 35th International Cosmic Ray Conference (ICRC 2017)*, Proceedings of Science (SISSA, Trieste, 2017) p. 542.

[408] G. Sigl, "Interpretation of ultra-high energy multi-messenger data," European Physical Journal Web of Conferences **53**, 01013 (2013).

[409] M. G. Aartsen *et al.* (IceCube Collaboration and Fermi-LAT, MAGIC, AGILE, ASAS-SN, HAWC, H.E.S.S., INTEGRAL, Kanata, Kiso, Kapteyn, Liverpool Telescope, Subaru, Swift/NuSTAR, VERITAS, and VLA/17B-403 teams), "Multimessenger observations of a flaring blazar coincident with high-energy neutrino IceCube-170922A," Science **361**, eaat1378 (2018).

List of abbreviations

AERA	Auger Engineering Radio Array
AGN	active galactic nuclei
AMIGA	Auger Muon and Infill for the Ground Array
ARIANNA	Antarctic Ross Ice-Shelf Antenna Neutrino Array
a.s.l.	above sea level
ATIC	Advanced Thin Ionization Calorimeter
BR	Black Rock Mesa
CMB	cosmic microwave background
CMF	center-of-mass frame
CORSIKA	Cosmic Ray Simulations for KASCADE
CRPropa	Cosmic Ray Propagation framework
DOM	digital optical module
DSA	diffusive shock acceleration
EAS	extensive air shower
EASIER	Extensive Air Shower Identification with Electron Radiometer
EBL	extragalactic background light
EGMF	extragalactic magnetic field
EHECR	extremely high energy cosmic ray
FD	fluorescence detector
GMF	galactic magnetic field

GPS	Global Positioning System
GRAND	Giant Radio Array for Neutrino Detection
GRB	gamma-ray burst
HEAT	High Elevation Auger Telescopes
HiRes	High-Resolution Fly's Eye
ICRC	International Cosmic Ray Conference
IGM	intergalactic medium
KASCADE	Karlsruhe Shower Core and Array Detector
LF	laboratory frame
LHC	Large Hadron Collider
LOS	line-of-sight
LR	Long Ridge
MD	Middle Drum
NICHE	Non-Imaging Cherenkov array
NKG	Nishimura-Kamata-Greisen
PMT	photomultiplier tube
POEMMA	Probe of MultiMessenger Astrophysics
SD	surface detector
SKA	Square Kilometer Array
SNR	supernova remnant
SUGAR	Sydney University Giant Airshower Recorder
TA	Telescope Array
TALE	Telescope Array Low-Energy Extension
UHECR	ultra-high-energy cosmic ray
UHEν	ultra-high energy neutrino
UK	United Kingdom

UMD	underground muon detector
USA	United States of America
VCV	Véron-Cetty and Véron

List of symbols

Particles:

e^-	electron
e^+	positron
γ_{bp}	cosmic background photon
γ_{p}	photon
K^-, K^+	kaons
μ^-, μ^+	muons
n	neutron
ν_e	electron neutrino
$\bar{\nu}_e$	electron antineutrino
ν_μ	muon neutrino
$\bar{\nu}_\mu$	muon antineutrino
ν_τ	tau neutrino
$\bar{\nu}_\tau$	tau antineutrino
p	proton
π^0	neutral pion
π^-, π^+	charged pions

Constants:

au	astronomical unit

c	speed of light in vacuum
e	elementary charge
ϵ_0	electric constant
m_e	electron rest mass
m_p	proton rest mass
$M_\odot$	solar mass

Other symbols:

$B_\parallel(s)$	component of the magnetic field parallel to the line-of-sight at point s
$B_\perp(s)$	component of the magnetic field perpendicular to the line-of-sight at point s
DM	dispersion measure
γ	spectral index
λ	wavelength
$n_e(s)$	total density of ionized electrons at point s
Ψ	Faraday rotation angle
Ψ_0	intrinsic Faraday rotation in the sources
RM	rotation measure
$Y_l^m(\theta, \phi)$	spherical harmonic with indices l and m